

UNIVERSITY OF CALIFORNIA  
RIVERSIDE

Controlling Electron Flows at the Nanoscale:  
Spectroscopic and Optoelectronic Investigations of Laser Media,  
Interlayer Carrier Multiplication, and Spin Currents

A Dissertation submitted in partial satisfaction  
of the requirements for the degree of

Doctor of Philosophy

in

Physics

by

Maxwell Jacob Grossnickle

June 2019

Dissertation Committee:

Dr. Nathaniel Gabor, Chairperson  
Dr. Jing Shi  
Dr. Vivek Aji

Copyright by  
Maxwell Jacob Grossnickle  
2019

The Dissertation of Maxwell Jacob Grossnickle is approved:

---

---

---

Committee Chairperson

University of California, Riverside

## ACKNOWLEDGMENTS

The path to becoming a scientist is a difficult one, requiring constant attention and reevaluation of one's innermost thought-processes. Every success, great or small, needs to be followed immediately by the eternal question: "*But could I be wrong?*" Internalizing this feeling takes enormous discipline but is, I think, integral to truly becoming a scientist. I have been fortunate enough to be helped in this endeavor by a number of incredible people.

I would first like to thank my advisor, Nathan Gabor. Working to build the Quantum Materials Optoelectronics Lab with him has been a truly incredible experience. Throughout my time in graduate school, Nathan has been an outstanding mentor and an incredibly clever scientist. Time and again we would work on a difficult problem, get stumped, and then overcome it after he suggested some minor tweak in our approach. Nathan was also very supportive of my explorations into the world of science outreach, a hobby that is showing more and more promise as time goes on. His inventive and flexible approach to problem-solving has been tremendously inspiring and helped me to develop into the versatile experimentalist I am today.

Throughout my graduate career, my family has awed me with their constant support and interest in my work, even as it became ever more intricate and arcane. Thank you, Mom and Dad, for believing in me even as I pursued a field you knew nothing about, I could not have done it without you. Thank you, Zach, for your support and for helping to start me down the path to exploring the wider world with our whirlwind London trip so long ago. Thank you, Aunt Carol, for the lovely care packages that always

arrived right when my austere grad student lifestyle was beginning to grate. A great thanks to you, Grandma Liz, for being my biggest cheerleader, whether or not I had accomplished anything worth cheering for. Lastly, thank you, Juliet, for your constant love and energy. The world with you in it is one where the hues are just a bit deeper, the music more enchanting, and the meals that much richer.

I would also like to thank my friends Kyle, Stephen, Alaina, and Devin. It is not easy to maintain a friendship across a thousand miles for the better part of a decade, and it means the world to me that you all have continued to smash, blast, and slash through dotes, horde, and those blasted boofs with me all this time.

My undergraduate research advisor Minhyea Lee deserves thanks for providing me with a truly rare undergraduate research experience. Most undergrads are given simple projects that don't truly represent what is actually done in a lab, but Minhyea from almost day one entrusted me with all the responsibilities of a full graduate student. This was a trial by fire experience, but her close attention and mentorship equipped me with the tools necessary to hit the ground running when I started research in graduate school.

Thank you to my QMO lab mates Fatemeh Barati, Trevor Arp, Dennis Pleskot, Jacky Wan, and Jedediah Kistner-Morris for your collaboration in the lab. Special thanks to Fatemeh for her brilliant work on our paper together and to Trevor for the jaw-dropping achievement of developing our lab's entire measurement software suite from scratch, without which most of the work in this dissertation would not have been possible (at least while also remaining sane).

Finally, I'd like to thank everyone else who made this possible. Glenda Barraza and Sonia Godinez were unsung front office heroes who helped me deftly navigate all the bureaucratic hurdles that come with building a brand-new lab. The passion and expertise of three of my high school teachers unknowingly set me down this path thirteen years ago: Mary Connelly and Greg Moldow, who inspired me to be a better writer, and Michael Colacino, who first showed me how incredible the world of physics could be.

Two chapters in this dissertation are based on previously published work. Chapter 3 is in part reproduced from A.T. Wieg, M.J. Grossnickle, Y. Kodera, N.M. Gabor, and J.E. Garay, "Nd:AlN polycrystalline ceramics: A candidate media for tunable, high energy, near IR lasers." *Appl. Phys. Lett.* **109**, 121901 (2016), with the permission of AIP publishing. Chapter 4, in part, is a reprint of the paper F. Barati, M. Grossnickle, S. Su, R. K. Lake, V. Aji, and N.M. Gabor, "Hot carrier-enhanced interlayer electron-hole pair multiplication in 2D semiconductor heterostructure photocells." *Nat. Nanotech.* **12**, 1134-1139 (2017).

To Mom, Dad, Zach, and Juliet

## ABSTRACT OF THE DISSERTATION

Controlling Electron Flows at the Nanoscale:  
Spectroscopic and Optoelectronic Investigations of Laser Media,  
Interlayer Carrier Multiplication, and Spin Currents

by

Maxwell Jacob Grossnickle

Doctor of Philosophy, Graduate Program in Physics  
University of California, Riverside, June 2019  
Dr. Nathaniel Gabor, Chairperson

Nanoscale fabrication methods are generating ever smaller and more precise devices that exhibit exciting physics but also require intense care to measure accurately. To address this need, we develop a modular optical microscope capable of rapidly measuring multiple parameters and generating datasets consisting of dozens of dimensions. We use this microscope to measure three very different physical systems. In the first, we spatially map excitation-emission characteristics of the laser medium neodymium aluminum nitride. We next measure interlayer charge transport in a van der Waals layered heterostructure consisting of monolayer MoSe<sub>2</sub> and bilayer WSe<sub>2</sub>. Our experiments show carrier multiplication as current is driven between materials and we develop a charge-transport model that explains the responsible mechanism and replicates the observed temperature dependence. Finally, in a platinum-yttrium iron garnet device, we use the interaction between the spin-Seebeck effect and the Shockley-Ramo theorem to spatially map electric field lines in arbitrary device geometries.

## TABLE OF CONTENTS

Acknowledgments	iv
Dedication	vii
Abstract	viii
Chapter 1: Introduction	
1.1 Science in the Flatlands	1
1.2 Optoelectronic properties of atomic layered materials	3
1.3 The Shockley-Ramo Theorem	5
References	9
Chapter 2: Instrumentation: Modular Multi-Dimensional Scanning Microscope	
2.1 Introduction	10
2.2 Scanning laser microscopy	10
2.3 Sample-measurement connections	18
2.4 Photoluminescence measurements	18
2.5 Ultrafast measurements	20
2.6 Strong magnetic fields	22
2.7 Conclusion	26
References	28
Chapter 3: Photoluminescence in a Neodymium-Doped Ceramic	
3.1 Developing New Laser Materials	29
3.2 Characteristics of Neodymium-doped Aluminum Nitride	33
3.3 Scanning Spectroscopic Microscope	33
3.4 Dopant-Segregation Dependence of Photoluminescence	35
3.5 Absorption and Emission Spectra	37
3.6 Conclusion	43
References	45
Chapter 4: Photocurrent and Carrier Multiplication in TMD Heterostructures	
4.1 Electronic engineering at the nanoscale	46
4.2 Basic experimental picture	48
4.3 MoSe <sub>2</sub> /2L-WSe <sub>2</sub> heterostructure synthesis	50
4.4 Spectroscopic characterization	52
4.5 Annealing process	54
4.6 Photocurrent and differential reflection	56
4.7 Gate and bias dependent interlayer current	58

4.8	Interlayer carrier multiplication	62
4.9	Confirmation of gate and temperature dependence	71
4.10	Photoresponse enhancement using carrier multiplication	73
4.11	Conclusion	76
	References	80
Chapter 5: Thermospintronic Imaging of Electrostatic Flux		
5.1	Introduction	83
5.2	Spin-Seebeck effect in a Pt-YIG device	85
5.3	Angular dependence of spin-Seebeck photovoltage	87
5.4	Mapping electrostatic flux lines	89
5.5	Removing the Seebeck effect	91
5.6	Excluding the Hall effect (and others)	93
5.7	Future directions	95
5.8	Conclusion	95
	References	100
Chapter 6: Conclusion		
6.1	Complexity begets complexity	102
Appendix A: Visualizing Nanoscience		
A.1	Introduction	103
A.2	Popularizing science	103
A.3	Translating science for the public	105
A.4	Creating high-quality visuals using free, open-source software	110
	References	

## LIST OF FIGURES

### Acknowledgments

### Dedication

### Abstract

### Chapter 1

1.1 Transition metal dichalcogenide atomic structure	2
1.2 Band gap and photoluminescence of TMDs	4
1.3 TMD heterostructure photocurrent	6
1.4 Shockley-Ramo theorem	8

### Chapter 2

2.1 Scanning mirror ray diagram	11
2.2 Raster imaging	13
2.3 Optical setup	15
2.4 Full microscope schematic	17
2.5 Wired device in cryostat	19
2.6 Spatial autocorrelation	23
2.7 Ideal Halbach cylinder	25
2.8 Experimental Halbach cylinder	27

### Chapter 3

3.1 Wurtzite crystal structure	30
3.2 Nd atomic transitions	32
3.3 Microscope setup	34
3.4 Nd:AlN spatial micrographs/PL	36
3.5 Photoluminescence plots	38
3.6 PL excitation/emission	40
3.7 PL excitation/emission normalized	42

### Chapter 4

4.1 MoSe <sub>2</sub> /2L-WSe <sub>2</sub> device schematic	47
4.2 MoSe <sub>2</sub> /2L-WSe <sub>2</sub> band alignment	49
4.3 Photoluminescence of MoSe <sub>2</sub> , WSe <sub>2</sub> , and combined MoSe <sub>2</sub> /WSe <sub>2</sub>	51
4.4 Atomic layer pick-up and transfer process	53
4.5 Comparative Raman measurements	55
4.6 Heterostructure photocurrent and deltaR/R	57
4.7 I/dlogI vs Vg/dVg (linetrace)	59
4.8 I vs Vg/Vsd 340K	61
4.9 Temperature dependence of the Interlayer <i>I-V</i> <sub>sd</sub> characteristics	63
4.10 Schematics of TMD band structure and interlayer electronic transport	65
4.11 Gate voltage, source-drain voltage, and temperature dependence of <i>dlogI/dV<sub>G</sub></i>	72
4.12 Interlayer photocurrent characteristics and multiplication enhancement	74
4.13 Wavelength dependence of interlayer photocurrent at T=300K	77

<b>Chapter 5</b>	
5.1 Thermospintronic generation mechanisms	84
5.2 Experimental spin-Seebeck setup	86
5.3 Measurements of a Pt-YIG Hall bar device	88
5.4 Spin-Seebeck measurements	90
5.5 Shockley-Ramo analysis of a Hall bar	92
5.6 Shockley-Ramo analysis of terraced Hall cross	94
5.7 Seebeck effect analysis	97
5.8 Lack of spin-Seebeck signal in Pt-GGG	98
5.9 Spin-Seebeck amplitude vs out-of-plane angle	99
<b>Appendix</b>	
A.1 Concept stills from <i>Halt and Catch Fire</i>	106
A.2 Motion and speed	108
A.3 Growth	108
A.4 Energy	109
A.5 Visualization: before and after	111
A.6 Visualization process	113
A.7 Skyrmion visual using scripting	115
A.8 Electron-hole liquid using particle simulations	116

## **Chapter 1**

### **Introduction**

#### 1.1 Science in the Flatlands

“I call our world Flatland, not because we call it so, but to make its nature clearer to you, my happy readers, who are privileged to live in Space.”

-A Square (Edwin A. Abbot, *Flatland*)

One of the most thrilling areas of physics in the early part of the 21<sup>st</sup> century has been the study of atomic layered materials – materials that, as their name describes, can be pared down to two-dimensional atomic layers and then manipulated to form a dizzying variety of novel nanoscale structures. The electronic properties of these materials are highly thickness-dependent, with some shifting from metallic to semimetal forms, others changing from indirect to direct band gap semiconductors, and a few even becoming superconductors! Paradoxically, this reduction in sample dimension from three to two also greatly increases the number of parameters needed to accurately characterize such devices. Consider this: for a sample that is one million atoms on a side (about 100  $\mu\text{m}$ , very ‘small’ by everyday standards), 99.9994% of the atoms live inside the sample, safe from direct exposure to the outside environment. If that same sample is thinned down until it is just ten atoms thick, the number of ‘unexposed’ atoms drops to 80% - now a substantial amount of the sample interacts directly with outside atmosphere, and an even greater proportion are affected by non-contact factors like the dielectric environment, temperature, magnetic fields, and many others. As our test subjects move towards the

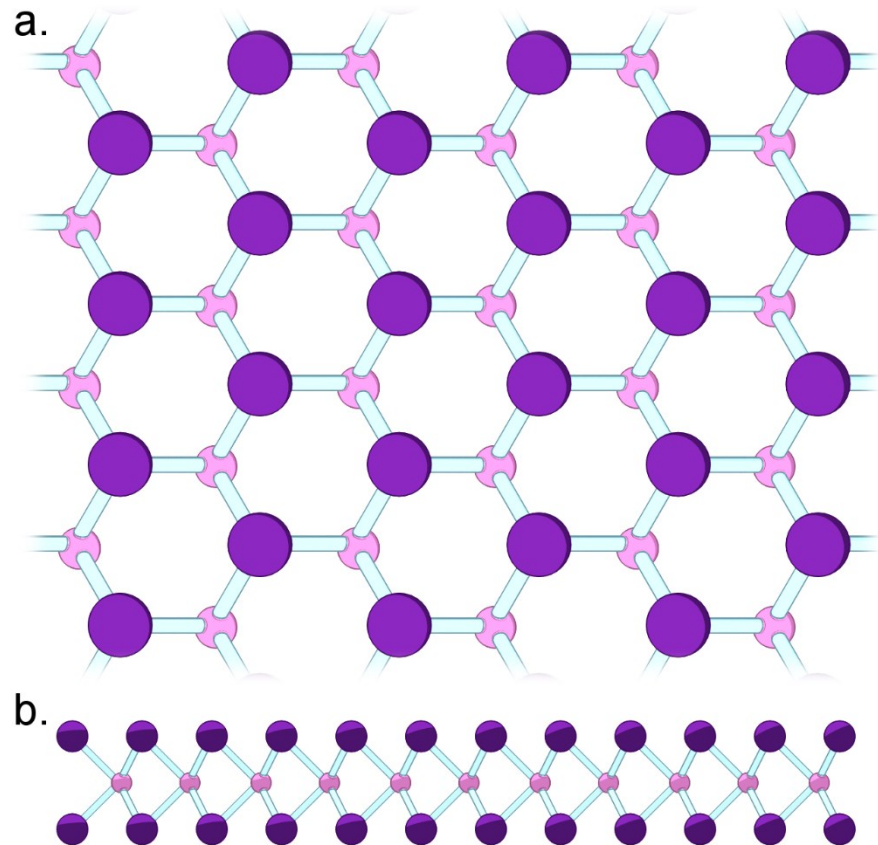


**Figure 1.1:** (a) Top-down view of a TMD in the 2H phase. Large purple atoms are chalcogens, while small pink atoms are transition metals. (b) Side view of a TMD in the 2H phase.

flatland our means for understanding them must become richer, more complex, and strive towards ever higher dimensions of study.

### 1.2 Optoelectronic properties of atomic layered materials

The first atomic layered material to be isolated was graphene<sup>1</sup>. Comprised of a single layer of graphite, it is fabricated by taking advantage of weak out-of-plane van der Waals (vdW) bonds to peel layers off a bulk sample using the now-famous Scotch tape method. This was followed a few years later by the first fabrications of monolayers of another class of vdW materials, the transition metal dichalcogenides (TMDs). The TMDs have the form  $MX_2$ , where M is a transition metal such as molybdenum, and X is a chalcogen like selenium. These atoms are strongly bonded in-plane in a hexagonal lattice (Fig 1.1a). For TMDs studied in this work, those with group VI metals, the conduction minima and valence maxima change as a function of layer thickness and the band gap becomes direct in the monolayer limit (Fig 1.2a)<sup>2</sup>, manifesting in enhanced photoluminescence as thickness decreases (Fig 1.2b)<sup>3</sup>. Monolayer TMDs also exhibit large excitonic binding energies, leading to even stronger light-matter interactions.

The spatial behavior of luminescence is an important question for TMDs; because of their high surface-to-volume ratios, they are very sensitive to environmental conditions, defects, and edge effects. Emissive properties can vary from material to material and in overlapped regions of combined heterostructures, as shown in Figure 1.3<sup>4</sup>. Indeed, this one of the most exciting aspects of TMDs, the ability to mix and match materials in devices and engage in pure band gap engineering free from doping. Chapter 4 discusses the exciting carrier multiplication physics that can arise when two TMDs,

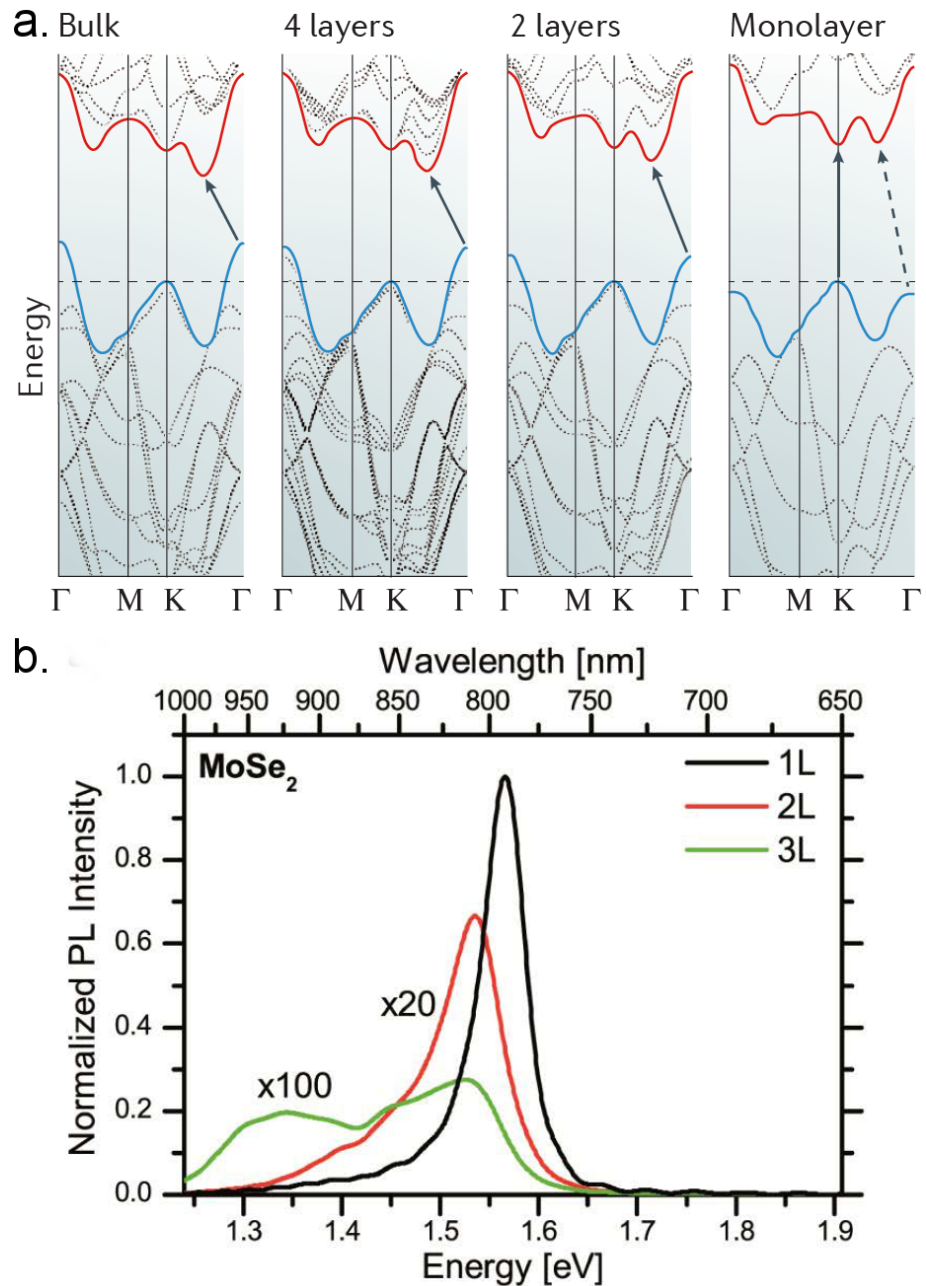


**Figure 1.2:** (a) Density field theory calculations of TMD band structure. (adapted from Ref 2) (b)  $\text{MoSe}_2$  photoluminescence as a function of layer thickness (adapted from Ref 3).

MoSe<sub>2</sub> and WSe<sub>2</sub>, are combined into a device that utilizes this band-gap engineering. The study of current flows through nanoscale landscapes necessitates developing a model that accounts for the important contributions sample geometry makes to such tiny devices, we discuss such a model in the following section.

### 1.3 The Shockley-Ramo theorem

A common tool for understanding an electronic system is to envision the motion of a single electron through the system. During the development of high-frequency vacuum tube radiation detectors in the 1930s, this method ran into a difficulty: a single electron generated in between the two electrodes of a vacuum tube will generate a current even before the electron itself reaches either electrode. This was explained separately by both William Shockley<sup>5</sup> and Simon Ramo<sup>6</sup> as arising from the propagation of the E-field from the electron as it moves near electrodes. The Shockley-Ramo theorem then states that the current measured in such a system is  $i = q\mathbf{v} \cdot \mathbf{E}(\mathbf{x})$ , where  $q$  is the amount of charge,  $\mathbf{v}$  is the instantaneous charge velocity, and  $\mathbf{E}(\mathbf{x})$  is the electric field that would exist at the particle's position if one electrode were held at unit potential and all others in the system held at ground (Fig 1.4a). The total charge on the electrode is  $Q = -q\varphi(\mathbf{x})$ , where  $\varphi(\mathbf{x})$  is the electric potential.

Eighty years later, Song et al. used the Shockley-Ramo theorem to explain long-range photoresponse seen in gapless materials. For such a system, there will be a photoexcited current  $\mathbf{j}_{ph}(\mathbf{r})$  and a diffusion current  $\mathbf{j}_d(\mathbf{r})$  which will obey the relations  $\nabla \cdot (\mathbf{j}_d + \mathbf{j}_{ph}) = 0$  and  $\mathbf{j}_d = -\sigma(\mathbf{r})\nabla\gamma$ , where  $\sigma$  is the conductivity and  $\gamma$  is the

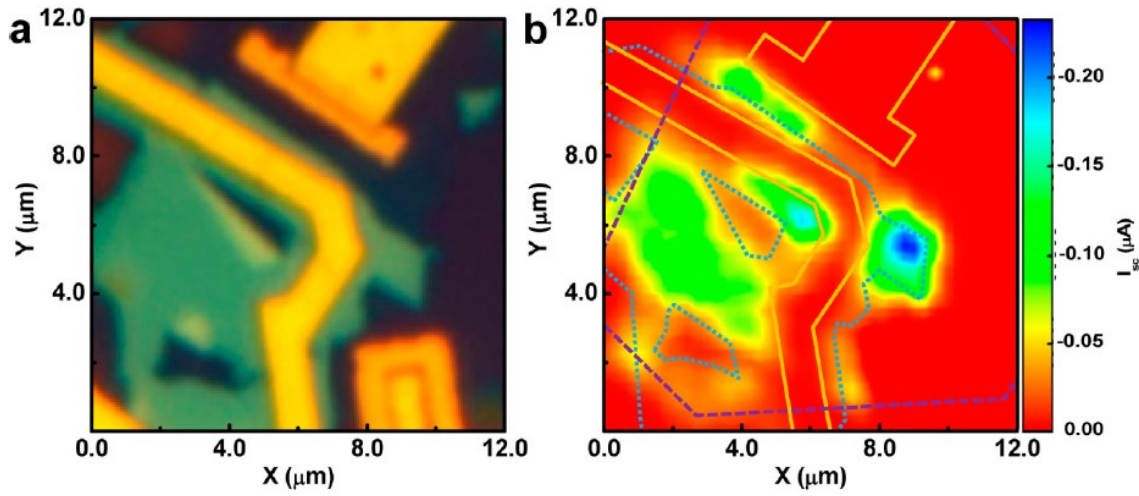


**Figure 1.3:** (a) Optical microscope image of WSe<sub>2</sub>/MoS<sub>2</sub> heterojunction. (b) Photocurrent map of the same device. The WSe<sub>2</sub> is outlined in dotted purple, the MoS<sub>2</sub> in dotted blue, and the electrodes in gold. Note the large photocurrent near the corner of the MoS<sub>2</sub> layer on the right (adapted from Ref 4).

electrochemical potential. However, for understanding the nonlocal behavior, it is more useful to introduce an auxiliary weighting field  $\psi(\mathbf{r})$  and auxiliary current  $\mathbf{j}^\psi(\mathbf{r})$  satisfying four relations:

$$\nabla \cdot \mathbf{j}^\psi(\mathbf{r}) = 0$$

$$\mathbf{j}^\psi(\mathbf{r}) = -\sigma \nabla \psi$$

$$\mathbf{n} \cdot \mathbf{j}^\psi(\mathbf{r}) = 0 \text{ at sample edges}$$

$$\mathbf{n} \times \nabla \psi = 0 \text{ at sample-contact boundaries}$$

With this information, it is possible to solve for the weighting field for arbitrary geometries, as shown in Fig. 1.4b. The direction of  $\nabla \psi$  points in the direction of  $-\mathbf{E}$ , allowing for the calculation of electric field lines at every point in space. The current measured by the contacts will then be  $I = A \int \mathbf{j}_{ph}(\mathbf{r}) \cdot \nabla \psi(\mathbf{r}) d^2 r$ , reaching a maximum when  $\mathbf{j}_{ph}$  and  $\nabla \psi$  are aligned and approaching zero as they become perpendicular.

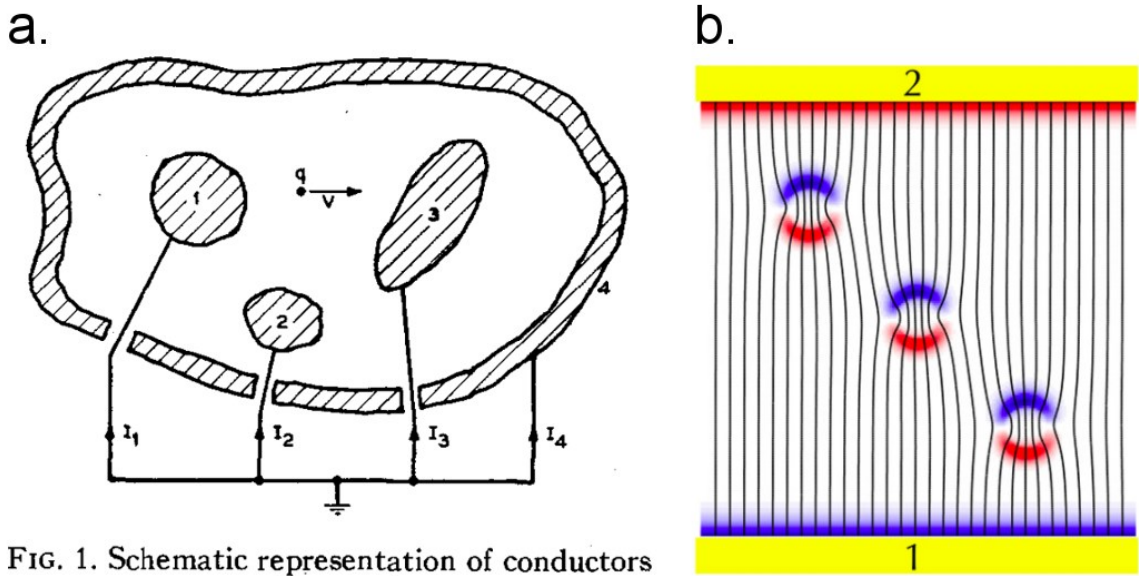


FIG. 1. Schematic representation of conductors and currents.

**Figure 1.4:** Treatments of non-local currents generated by moving charges. (a) Shockley's original description of a charge moving in a region populated by conductors. (adapted from Ref 5) (b) Shockley-Ramo field lines and resulting photocurrent (blue and red areas) for regions with increased conductivity. (adapted from Ref 7)

## REFERENCES

1. Novoselov, K.S. et al. “Electric field effect in atomically thin carbon films.” *Science* **306**, 5696 (2004) 666-669.
2. Manzeli, S. et al. “2D transition metal dichalcogenides.” *Nat. Reviews* **2**, 17033 (2017).
3. Tonndorf, P. et al. “Photoluminescence emission and Raman response of monolayer MoS<sub>2</sub>, MoSe<sub>2</sub>, and WSe<sub>2</sub>.” *Optics Express* **21**, 4 (2013).
4. Cheng, R. et al. “Electroluminescence and photocurrent generation from atomically sharp WSe<sub>2</sub>/MoS<sub>2</sub> heterojunction p-n diodes.” *Nano Lett.* **14**, (2014) 5590-5597.
5. Shockley, W. “Currents to conductors induced by a moving point charge.” *Jour. Appl. Phys.* **9**, 635 (1938).
6. Ramo, S. “Currents induced by electron motion.” *Proc. IRE* **27**, (1939) 584-585.
7. Song, J. C. W. and Levitov, L. S. “Shockley-Ramo theorem and long-range photocurrent response in gapless materials.” *Phys. Rev. B.* **90**, 075415 (2014).

## **Chapter 2**

### **Instrumentation: Modular Multi-Dimensional Scanning Microscope**

#### 2.1 Introduction

Devices with dimensions of microns or more have such a low surface/volume ratio that it is usually assumed that most observable physics is occurring in the ‘bulk’ of the device. However, as devices become tinier and tinier, this ratio shifts, and surface or interface interactions become much more important. The performance of a nanoscale device may depend sensitively on the environment, sample geometry, or even probe location of a measurement. This necessitates the development of versatile measurement tools that can rapidly probe a large parameter space in order to identify subtle effects that may previously have been unmeasurable.

In this chapter, we discuss the flexible measurement architecture we developed to carry out drastically different experiments on such devices. The next section discusses the core idea of this apparatus, the scanning laser microscope, while the rest of the chapter gives detailed descriptions of the different subsystems incorporated to enhance the functionality of the microscope.

#### 2.2 Scanning laser microscopy

The basic idea of the scanning laser used in our experiments can be understood as a modification to the most basic of optics problems: the interaction of a lens and a point source. When a point source is placed at the focal point  $f_1$  of a lens, the light that passes through the lens will be collimated (Fig 2.1). Placing a second lens after the first will result in the light being focused to a point at the focal length  $f_2$  of the second lens. An

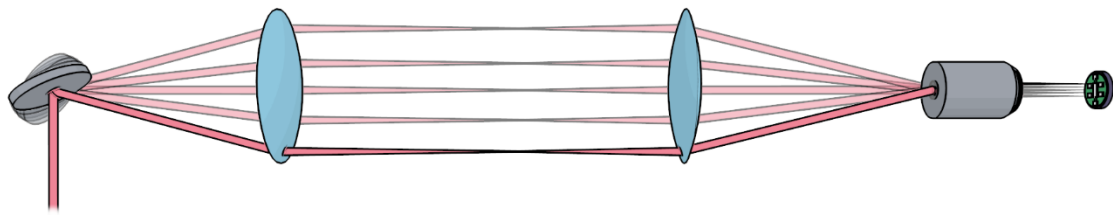


**Figure 2.1:** Ray diagram of a scanning mirror laser setup. Different beam angles result in translation of the beam on the sample.

objective lens placed at this point will then collimate the light into a very tight beam. Looking at the behavior of different rays, we can see that an increase in initial ray angle corresponds to a spatial translation of the collimated ray emerging from the objective lens. From this it follows that if we can rotate a tightly focused laser beam at the focal point of the first lens in such a system, the laser beam will translate in space after it exits the objective lens. Translating the beam in this way preserves a non-distorted Gaussian cross section, allowing us to probe different points in space with good understanding of the nature of the illumination at the sample surface.<sup>1</sup> From this, we can raster-scan the beam across the sample to build up 2D maps of properties like reflection, photoluminescence, or photovoltage (Fig 2.2.)

A real laser beam, no matter how tightly focused, will still have some diameter, so it will be magnified or de-magnified as it passes through the two lenses. The amount of this magnification is given by the relation  $M = f_2/f_1$ . By carefully selecting the focal lengths of the two lenses used, the beam size can be adjusted to completely fill back focal plane of the objective lens. This is important in high-resolution imaging because underfilling the objective reduces the effective numerical aperture (NA) of the lens(cite). The Abbe diffraction limit states that the minimum resolvable distance of focused light is given by  $d=\lambda/(2*NA)$ , where  $\lambda$  is the wavelength of light. Reducing the NA thus increases the minimum size of a focused laser spot, so it is critical to carefully control the level of back focal plane filling to maximize resolution.

In our real system, this process is implemented using paired one-dimensional galvanometric mirrors (Thorlabs GVS102) to deflect an incoming laser beam on two

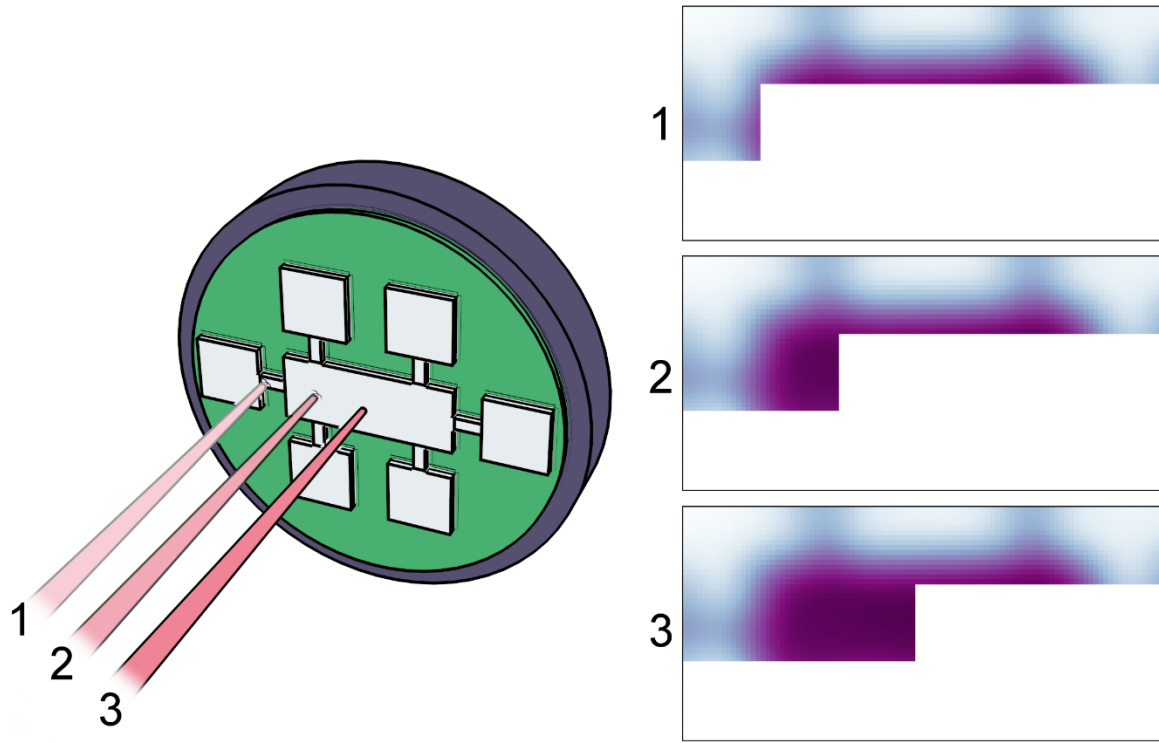


**Figure 2.2:** Measuring with a raster-scanned laser beam. As the beam moves from position 1 to 2 to 3, we record properties of the device (in this case, reflection) at each point in space.

perpendicular axes. Unfortunately, this setup has the side effect of complicating the simple ray diagram laid out in the previous paragraph – the finite distance between the two mirrors means both rotation points can't happen exactly at the focal point of the first lens in the setup. This results in a slight spatial translation of the beam at the focal point of the second lens as the beam is scanned, which requires that the objective lens be slightly underfilled so that the beam does not clip the edges as it is scanned. Sadly, at the time of this writing, single mirrors that rotate on two axes are not commercially available.

For illumination, we use a Ti:Sapph cavity (Coherent) pumped by a solid-state laser to generate an ultrafast beam that is tunable from 690-930nm. The pulse duration is 180 fs, the repetition rate is 76 MHz, and the maximum power at the start of the microscope is ~600mW. Fig. 2.3 shows a diagram of the complete microscope, while Fig 2.4 shows the microscope as it is laid out on the optical table. After leaving the cavity, the beam passes through a reducing pair of lenses to shrink the beam width down enough to fit on the galvo mirrors. After the reducing pair, the beam is split along two paths; one with a static length and one that passes into a moveable delay stage. Varying the position of this stage allows us to tune the arrival time of the pulse from that leg, enabling time-resolved pump-probe measurements. The two beams eventually pass through separate 2D galvo mirrors before being directed along the same path by a second beamsplitter. The beam(s) then passes through a magnifying pair of lenses before finally reaching the objective.

All lenses in this part of the microscope are achromatic doublets (Thorlabs AC254-B) coated with 650-1050nm antireflection coatings to reduce the effects of

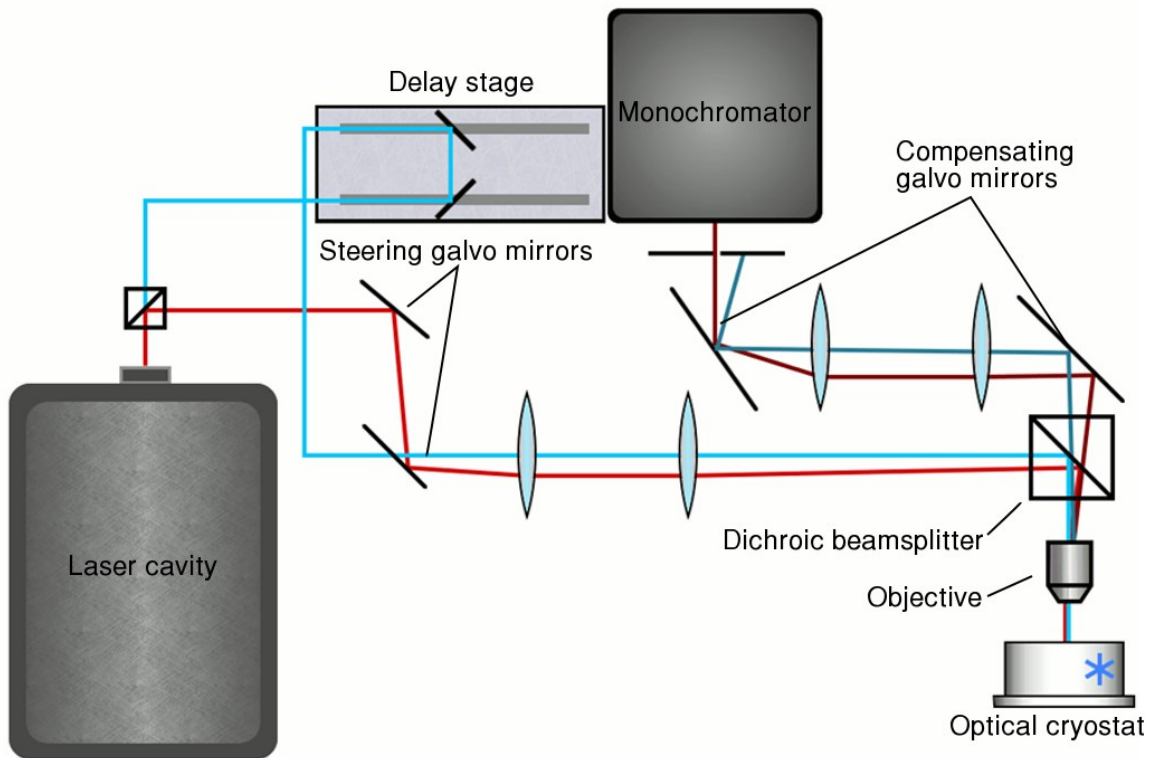


**Figure 2.3:** Scanning microscope diagram. The bright red line is the incoming ‘reference’ beam path, blue is the delay beam path, dark red is the photoluminescence path, and dark blue is reflected light from the pump beam.

spherical and chromatic aberration. The steering mirrors in use in the system are protected silver mirrors ( $R>96\%$ ) or broadband dielectric mirrors ( $R>99\%$ ) while the galvo mirrors are gold-coated ( $R>92\%$ ). The objective was selected depending on the particulars of each experiment, for the experiments in Chapters 3 and 4, we used an Olympus LCPLN-IR 5X objective. This objective provided a very tight beam spot, included a correction collar to compensate for the cryostat window (see section 2.3) and varied in transmittance by  $<15\%$  from 700-1500nm. For the measurements in Chapter 5, we used a Mitutoyo Plan Apo NIR 5X objective. This lens possessed a very large 4.8 mm field of view and exhibited transmittance variation of  $<15\%$  from 800-1500nm. In general, we measured power using a calibrated photodiode (Thorlabs S130C) placed before the galvo mirrors. The reduction in power between this point and the exit of the objective was measured to be 2/3 – that is, a measured power of 90 mW corresponded to 30 mW of power on the sample.

To measure reflectance of the device, we placed a pellicle beamsplitter in the reference beam path before the galvo mirrors. Light reflected from the sample is directed through a 4x objective onto a Si photodiode. The choice between pellicle and cube beamsplitters was a difficult one, as neither was perfect for our measurements. The cube beamsplitter introduced back reflections off its multiple faces, resulting in an artificial bright spot, while pellicles suffer from thin film effects that cause their performance to vary wildly depending on the wavelength of incident light. Ultimately, we selected the pellicle under the assumption that we would not frequently change the light wavelength in measurements.

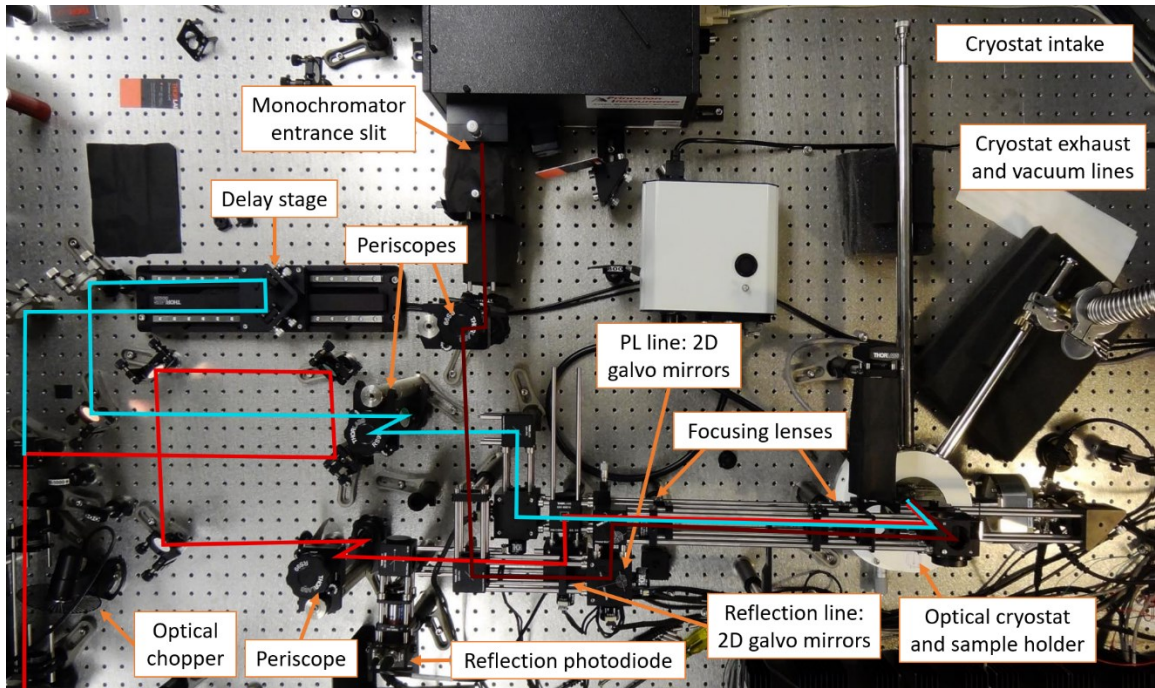


**Figure 2.4:** Photograph of optical scanning microscope setup. The bright red line is the incoming ‘reference’ beam path, dark red is the delay beam path, and blue is the photoluminescence path.

### 2.3 Sample-measurement connections

The devices in Chapters 3 and 4 were housed in an optical flow cryostat (Janis). Samples were fixed to silicon or sapphire substrates and then attached to a gold-plated coldfinger in the cryostat using carbon tape (see Fig 2.5). The substrates were patterned with gold contacts that were later connected to the sample by wire bond. These gold contacts were then soldered to electrical feedthroughs that terminated in BNC connectors outside of the cryostat, allowing us to apply and measure voltages and currents.

With a sample in place, we used a turbo pump to evacuate the cryostat down to a pressure of  $\sim 10^{-6}$  mTorr. The cryostat was capable temperature ranges of 4k – 400K, with temperature control provided by cold helium vapor flow from a dewar and a thermocouple heater attached to the coldfinger. The cryostat is accessed optically through a 1 mm-thick quartz window which is corrected for using the collar on the appropriate objective lens.

To record data, we connected the electrical feedthroughs and various photodiodes via coax to a data acquisition card (National Instruments) which was connected to a personal computer. For the measurements in chapter 3, data was taken using a LabVIEW interface. For all other measurements we used an in-house software solution developed in Python and published in *Review of Scientific Instruments*<sup>2</sup>.

### 2.4 Photoluminescence measurements

Measuring photoluminescence (PL) spectra at arbitrary points presents an interesting technical challenge in a system that scans the illumination source. To accomplish these measurements, we first replaced the silver steering mirror directly

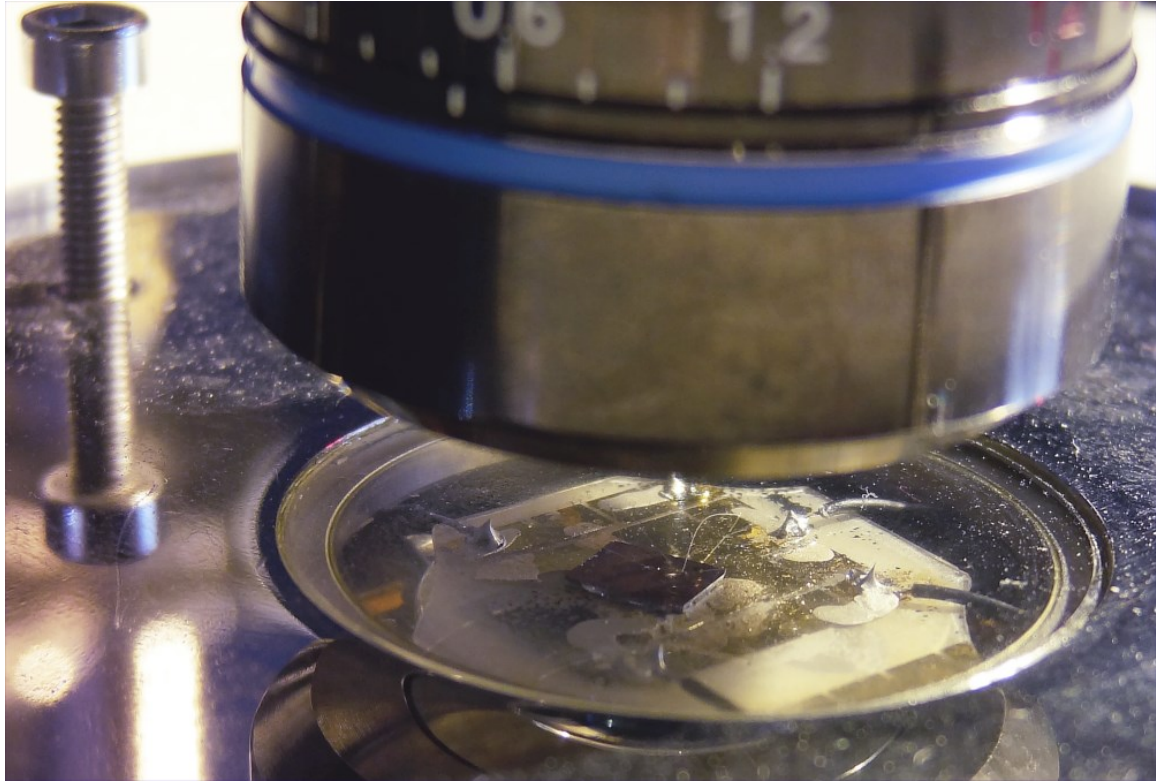


**Figure 2.5:** Photograph of a device in the optical cryostat. The sample is connected to the chip carrier by one mil gold wire bonds.

preceding the objective lens with a dichroic edgepass filter with a 1000 nm longpass wavelength. The second beam line (see Fig 2.3) introduced by this filter utilized optics with 1050-1650nm antireflection coatings. The major hurdle to overcome was accounting for the translation of the photoluminescence after it emerged from the objective lens. Though the angle of the photoluminescence was the same as that of the normal beam on its return path, the extra distance introduced by the PL path and the different wavelengths meant that the correspondence between the reflected beam and PL was not 1:1. To compensate for this, the PL line included a pair of scanning galvos mirrors, synced to those in the reference line, but with the °/V factor tuned very carefully to exactly stabilize the PL emission. The PL then passes through an achromatic doublet lens before entering a Czerny-Turner monochromator (Acton). No attempt was made to precisely match the f# of the lens to the monochromator as the spectral resolution achieved with this setup was still on the order of  $\pm 2\text{nm}$ , which was significantly sharper than needed for our measurements. Finally, the PL was measured using an amplified InGaAs photodiode that was battery powered to give the absolute lowest possible noise. An InGaAs avalanche photodiode was tested for the system but ultimately not used due to its very small sensor area and high noise.

## 2.5 Ultrafast measurements

Though we ultimately never carried out a full time-resolved measurement, this aspect of the system still merits description. The basic idea, as touched on earlier, is to split a pulsed beam along two paths, with one ‘reference’ path of fixed length and one ‘delay’ path capable of changing its length. The delay path was manipulated using a

220mm linear translation stage (Thorlabs) holding a pair of perpendicular mirrors. The stage was positioned such that the delay pulse could be varied from -400 ps to +1000 ps around the reference pulse. To characterize the pulse quality, we measured the field autocorrelation of the two pulses, which is defined by

$$A(\tau) = \int_{-\infty}^{+\infty} E(t)E^*(t - \tau)dt$$

where  $E(t)$  is a complex electric field and  $\tau$  the delay time. By measuring with a slow (compared to the pulse) detector such as a photodiode, measure a real intensity given by

$$I(\tau) = \int_{-\infty}^{+\infty} |E(t)E^*(t - \tau)|^2 dt$$

which results in data given by Fig 2.6. For  $\text{sech}^2$  pulses, the pulse duration is roughly equal to 65% of the full width at half max of the autocorrelation, so from this data we see that the pulselwidth is  $\sim 180\text{fs}$ .

Attempting to add extra dimensions in a time resolved measurement by spatially mapping data as a function of time delay requires a nuanced approach. In our setup, where each beamline had its own set of galvos, it was impossible to tune the galvos enough to scan both beams at once. Scanning one beam while holding the other fixed, however, is possible but introduces two additional autocorrelation effects. The first is that the act of scanning introduces an additional time delay – a scanning beam may be deflected enough to add an additional 1 cm of travel distance, resulting in 33 fs of additional travel time! The second is that any minor tilt in the sample will result in a path length discrepancy that depends on the spatial position of the scanning beam. For such a

scenario, with a scanned beam on a tilted sample, the intensity autocorrelation measured by a slow detector at any point in the 2D plane (Fig 2.6) will be

$$I(\tau, x_s, y_s)$$

$$= \int_{-\infty}^{+\infty} \int_{-\infty}^{+\infty} \int_{-\infty}^{+\infty} \left| e^{-\left(\frac{x_c^2}{2} + \frac{y_c^2}{2}\right)} * e^{-(t-\tau)^2} * e^{-I(t-\tau)} + e^{-\left(\frac{(x_c-x_s)^2}{2} + \frac{(y_c-y_s)^2}{2}\right)} \right.$$

$$\left. * e^{-I\left(t + \sqrt{\frac{x_s^2}{c} + \frac{y_s^2}{c}} + g * \frac{x_s}{c}\right)} * e^{-I\left(t - \sqrt{\frac{x_s^2}{c} + \frac{y_s^2}{c}} + g * \frac{x_s}{c}\right)} \right|^2 dx_c dy_c dt$$

where  $x_c$  and  $y_c$  are the coordinates of the central, non-scanning beam,  $I$  is the intensity of the beam,  $x_s$  and  $y_s$  are the coordinates of the scanning beam,  $g$  is the percentage grade of the sample, and  $c$  is the speed of light. This form assumes that the measurement coordinates are set such that the sample is only sloped along one axis.

## 2.6 Strong magnetic fields

The final experiment in this dissertation required high magnetic fields with an uncommon twist: we needed to be able to rotate the fields to arbitrary angles in the sample plane. Most optical cryostats with superconducting magnets are designed so that the field is pointing vertically, as was the case with the setup available in our lab when this project began. Commercial solutions with additional coils oriented to point in-plane, also known as vector magnets, are available, but have high cost, long construction lead times, and require expensive liquid helium to operate. To avoid these issues, we looked for inspiration to the field of high-energy physics, which also requires large magnetic fields to steer beams in particle colliders. In the 1980s, Klaus Halbach developed Halbach arrays<sup>3</sup>, linear combinations of permanent magnets oriented such that their fields are

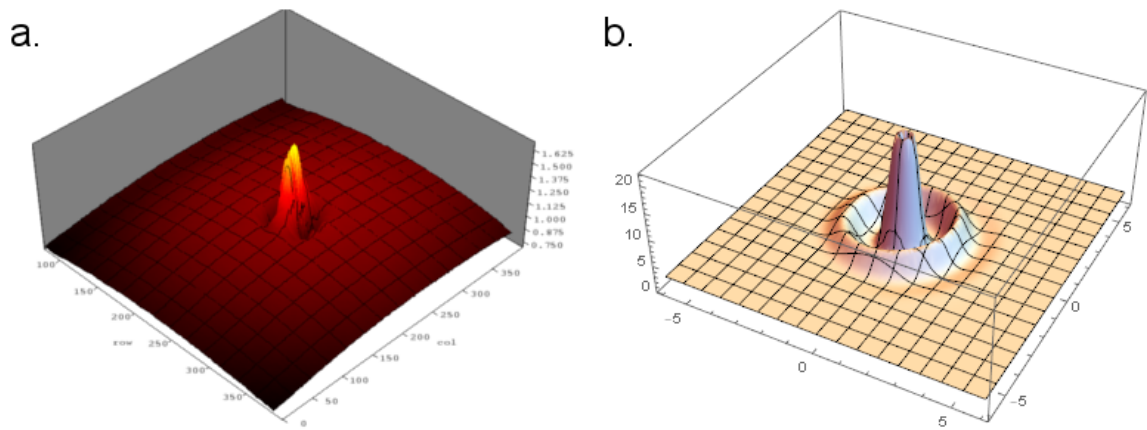


**Figure 2.6:** Spatial autocorrelation. **(a)** Autocorrelation in 1100 nm photoluminescence of a silicon wafer. **(b)** Mathematica simulation of spatial autocorrelation profile.

forced to add together on one side of the array while remaining weak on the other side. Generalizing this idea to two dimensions results in Halbach cylinders, where the magnetization in the cylinder is rotated to generate a desired field in the hollow center of the cylinder (Fig 2.8). The magnetization direction is given by

$$M = M_r \left( \cos \left( (k - 1) \left( \varphi - \frac{\pi}{2} \right) \right) \hat{r} + \sin \left( (k - 1) \left( \varphi - \frac{\pi}{2} \right) \right) \hat{\varphi} \right)$$

where  $M_r$  is the ferromagnetic remanence and  $k$  denotes the order of the field. For  $k=2$ , the field inside the cylinder will be completely uniform and equal to

$$H = M_r \ln \left( \frac{R_o}{R_i} \right) \hat{x}$$

Unfortunately, the ability to smoothly vary the magnetization of a material does not exist at the time of this writing, but it is possible to approximate a Halbach cylinder from existing magnets. To do this, we created a gapped ‘cylinder’ consisting of six 0.5”x 0.5” x 2” N52-grade neodymium permanent magnets, magnetized through the 0.5” dimension, and arranged as shown in the finite element magnetic field simulation in figure 2.xx. This simulation was carried out using FEMM. The end result was a ‘cylinder’ with a central field value of 0.52 T and a region of 1mm x 2mm where this field varied by less than 1%, as shown in Fig 2.8. We mounted the Halbach cylinder on horizontal and vertical rotation stages, which, combined with the central gap, allowed us to orient the magnetic field at any arbitrary angle, in- or out-of-plane.

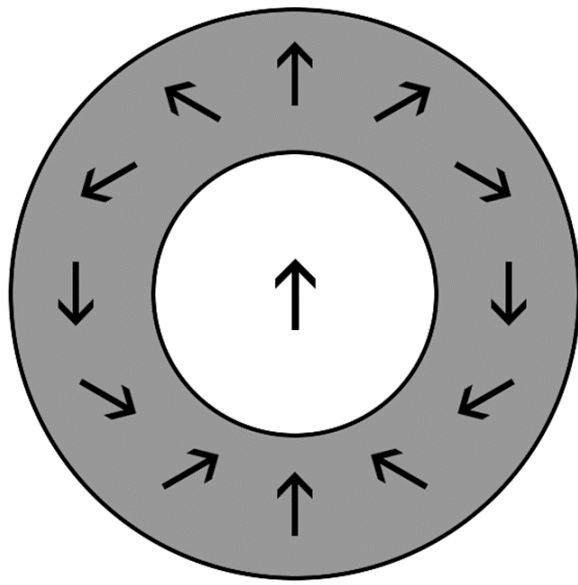


**Figure 2.7:** Ideal cylindrical Halbach array. The grey areas represent magnetic material while white represents air. Arrows indicate magnetic field direction.

## 2.7 Conclusion

The ultimate goal of this experimental setup was to design a highly customizable, modular microscope that could be rapidly updated to pursue new avenues of research, as the ensuing chapters will demonstrate. All told, measurements utilizing our microscope could vary six parameters: power, wavelength, polarization, time delay, voltage, and temperature, all at any point in the 2D plane of a sample. We could also measure four properties: reflectance, current, photocurrent and photoluminescence. A hypothetical measurement utilizing all these facets of the tool we developed would yield an incredibly dense 32-dimension dataset. Though we have never attempted such a comprehensive experiment, this number serves to illustrate the versatility of the microscope as we discuss the results achieved in the rest of the dissertation.

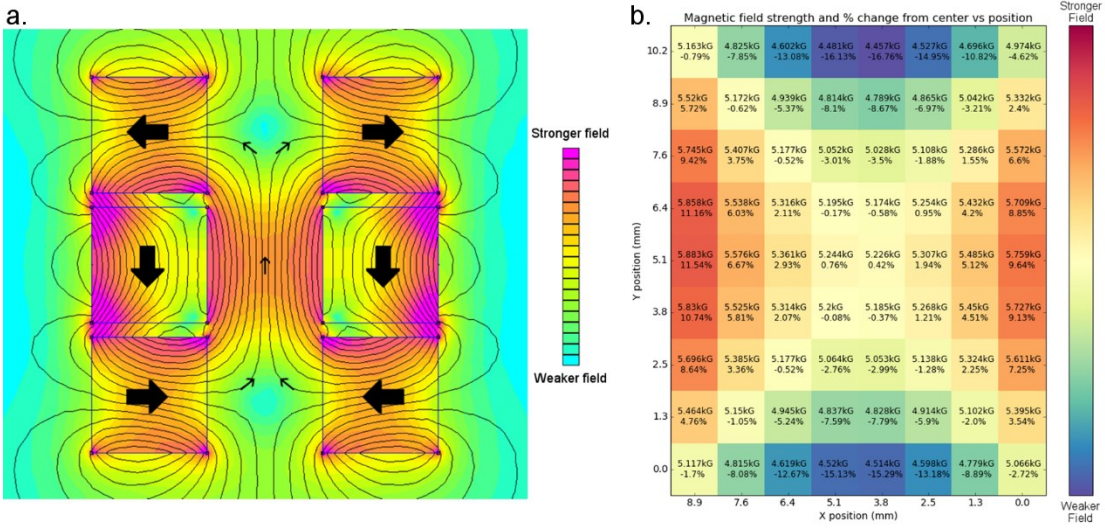


**Figure 2.8:** Simplified Halbach ‘cylinder’. (a) FEMM<sup>4</sup> (ref) simulation of magnetic field. (b) Measured magnetic field strength between central magnets of Halbach array used in this dissertation.

## REFERENCES

1. Gabor, N.M. (2012) *Extremely efficient and ultrafast: electrons, holes, and their interactions in the carbon nanotube pn junction* (Doctoral dissertation).
2. Arp, T.B. & Gabor, N.M. “Multiple parameter dynamic photoresponse microscopy for data-intensive optoelectronic measurements of van der Waals heterostructures.” *Rev. Sci. Instrum.* **90**, 023702 (2019).
3. Halbach, K. “Design of permanent multipole magnets with oriented rare earth cobalt material.” *Nucl. Instrum. Methods* **169** (1980) 1-10.
4. Meeker, D. *Finite Element Method Magnetics*. Jan 30, 2018.  
<http://www.femm.info/>

## **Chapter 3**

### **Photoluminescence in a Neodymium-Doped Ceramic**

#### 3.1 Developing New Laser Materials

One of the grails of laser materials is a lasing medium that is low-cost, durable, and most importantly, has a high thermal conductivity. Durability would allow the material to be used in a wide range of applications without worrying about damaging a fragile crystal, while a high thermal conductivity is critical for high-power applications. Neodymium-doped yttrium aluminum garnet (Nd:YAG) has been the most commonly used solid-state lasing medium since its development in 1961 as it exhibits sharp emission lines and moderately high power output<sup>1</sup>. Another widespread material, Nd-doped glass (Nd:Glass), has broader emission lines that enable amplification of shorter temporal pulses and thus increase peak energy output. A proposed successor, neodymium-doped aluminum nitride (Nd:AlN), is durable, has a high thermal conductivity, and possesses traits of both single crystal and glass lasing media, providing the opportunity to develop a laser with both higher continuous wave (CW) and pulsed outputs than existing materials. This chapter discusses a study of the spatial and spectral variations of photoluminescence emission in a ceramic Nd:AlN material.

#### 3.2 Characteristics of Neodymium-doped Aluminum Nitride

Aluminum nitride (AlN) is a ceramic (defined as a compound formed from metallic and nonmetallic elements) with a wurtzite crystal structure (pictured in Fig 3.1) and a wide band gap of 6.01 eV, far higher than the most energetic Nd absorption value of 1.65 eV. AlN also has high thermal conductivity and durability, especially when

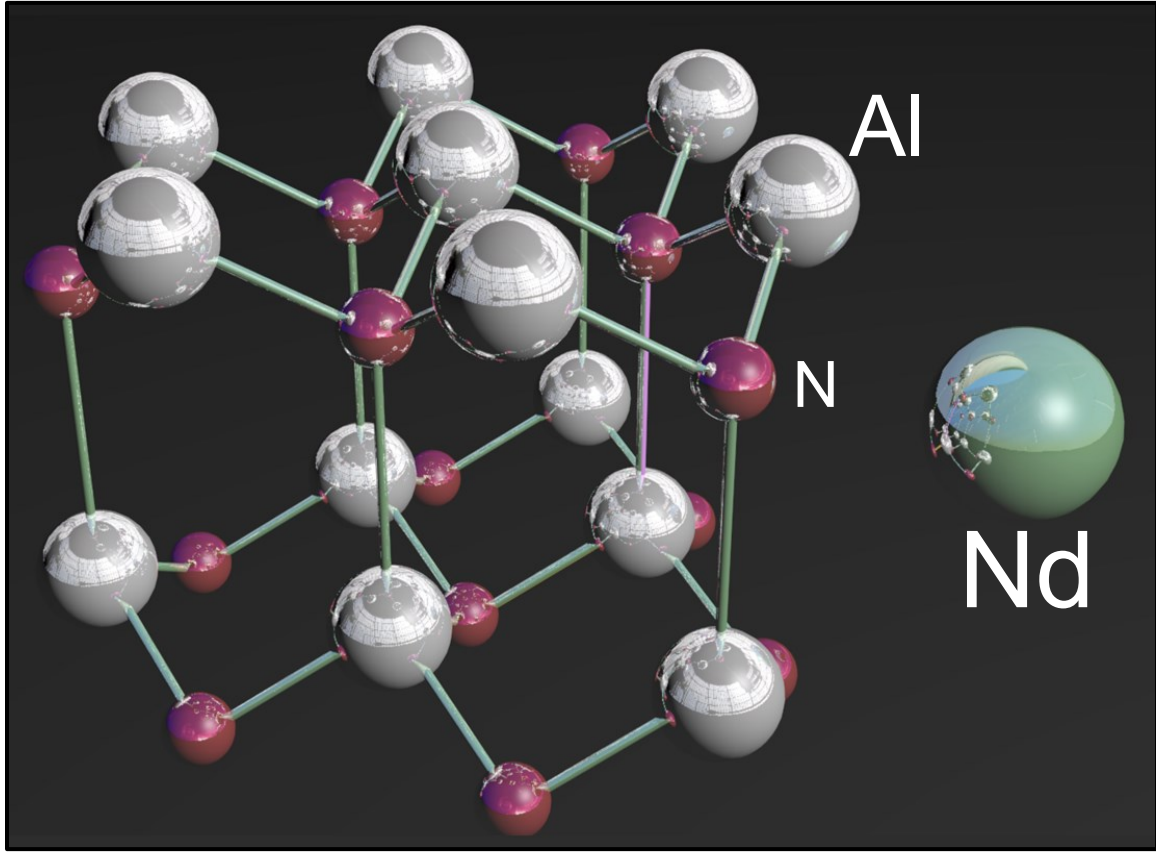


**Figure 3.1:** Wurtzite crystal structure of AlN with Nd atom for scale.

compared to YAG (see Table 3.1). These mechanical and thermal properties make it an ideal candidate to host Nd for lasing purposes.

Neodymium is a popular dopant in laser materials due in large part to its high absorption cross section. In these laser materials, a trivalent Nd<sup>3+</sup> atom can absorb at several near IR wavelengths and emit farther into the IR. The specific values vary depending on the host material, typical transitions for Nd:YAG are shown in Fig 3.2. These variations are largely due to differences in the crystal field experienced by the Nd atom in different materials or even at different lattice sites in the same material. In a single crystal material like Nd:YAG, the Nd atoms replace yttrium in identical lattice positions, giving very sharp transitions. Nd atoms in a glass see many different environments which leads to substantial inhomogeneous broadening of spectral lines. While AlN can be grown as a single crystal, the Nd:AlN in this project was fabricated using a method called current-activated pressure-assisted densification (CAPAD)<sup>3-5</sup> which yields polycrystalline samples.

The bulk polycrystalline samples presented here were processed from commercially available aluminum nitride and Nd metal powders; 97% purity as AlN, 1–2 μm particle size (Tokuyama Co., Japan) and 99.9% purity, 200 mesh Nd powder, (Alfa Aesar) respectively. Nd was added as NdN to produce AlN with 0.5 atomic % Nd. The metal Nd powder was loaded into the furnace tube in an inert atmosphere glovebox and the tube was sealed before being transferred to the furnace where nitrogen flow was initiated prior to heating. The Nd was then heated to 600 °C under flowing nitrogen for 6 h. Host and dopant powders were mixed using high energy planetary ball milling. Powders and

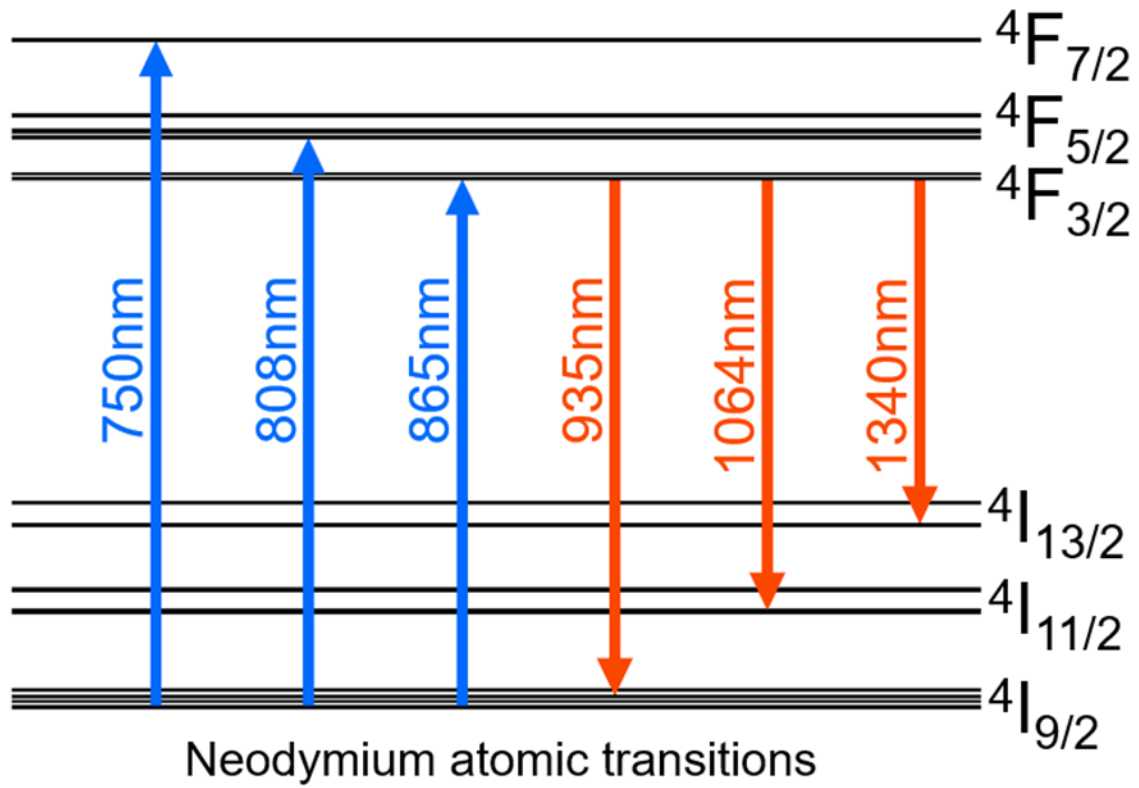


**Figure 3.2:** Neodymium atomic transitions (adapted from ref 2).

milling media were loaded into planetary mill jars and sealed under an argon atmosphere prior to milling. A 10:1 ball:powder mass ratio was used and milling was performed at either 450 rpm (Sample 1) or 600 rpm (Sample 2) for 3 h. Powders were collected and stored under argon post milling.

Powders for CAPAD (current activated pressure assisted densification) processing were loaded into a graphite die (19 mm inner diameter) and plunger assembly under an argon atmosphere before being transferred to a custom built CAPAD apparatus and processed. Samples were processed at 1700 °C (sample 1) or 1750 °C (sample 2) under 105 MPa of applied uniaxial pressure using a heating rate of approximately 500 °C min<sup>-1</sup>. Experiments were done in vacuum ( $\sim 3 \times 10^{-2}$  Torr). Temperature was measured using an optical pyrometer focused on the die wall.

### 3.3 Scanning Spectroscopic Microscope

Measuring photoluminescence with a scanning microscope required adding an entirely new beam path to the system, as shown in Figure 3.3. We replaced the mirror before the objective with a 1000nm high-pass dichroic beamsplitter, allowing photoluminescence to pass through a complimentary set of optics optimized for the 1000-1600nm wavelength range. The photoluminescence then passed through a second set of galvo mirrors that compensated for the scanning action. Once the beam was made stationary, it was passed into a Czerny-Turner monochromator to allow for spectroscopic measurements to be performed. Due to the spectral broadness of the features being measured, no attempt was made to match the f# of the incoming beam with the monochromator as the increased spectral resolution was unnecessary. A battery powered

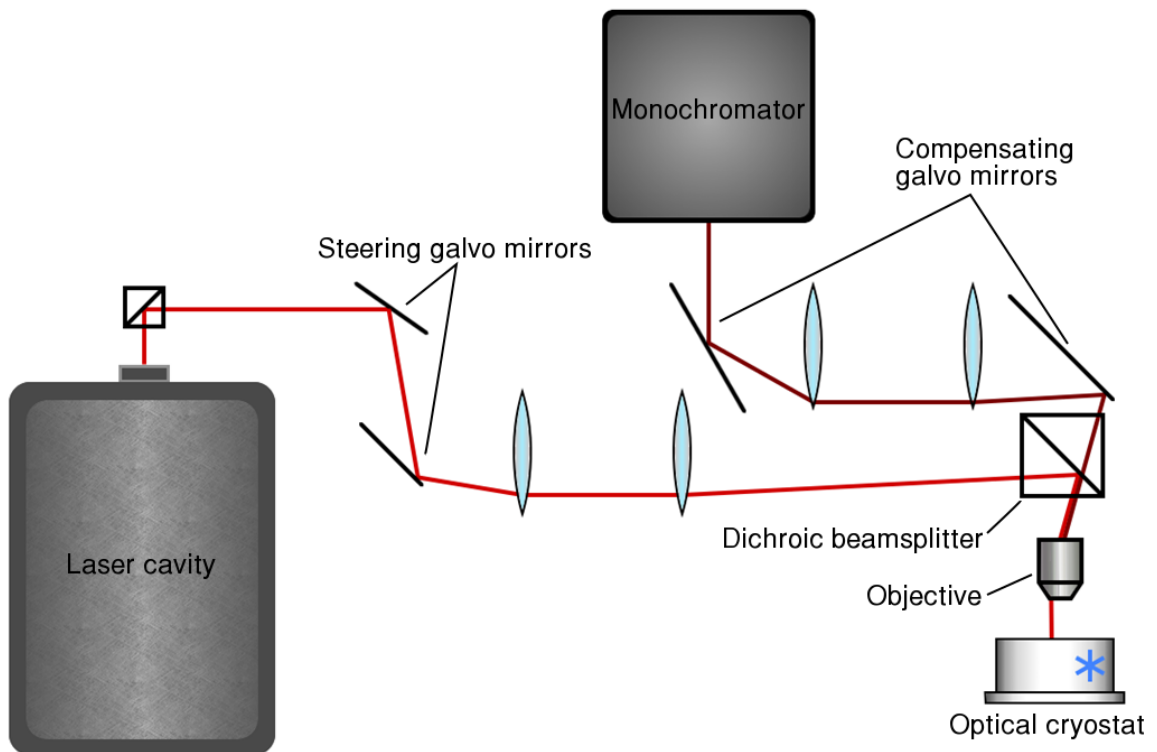


**Figure 3.3:** Scanning photoluminescence microscope setup.

InGaAs amplified photodetector was placed at the exit of the monochromator to measure the photoluminescence. The battery-powered option was selected as it offered better noise performance than the line-powered version. Another photodetector option was considered but discarded: an InGaAs avalanche photodetector, which had too small of an active sensor area ( $0.04\text{ mm}^2$ ) to be useful.

### 3.4 Dopant-Segregation Dependence of Spatial Photoluminescence

The influence of dopant segregation on the uniformity of luminescence can be determined by performing optical luminescence microscopy on the same locations as the SEM. 2D luminescence maps are shown in Figure 3.4c (Sample 1) and 3.4f (Sample 2). Comparison clearly reveals that the PL is significantly more uniform in the sample with minimal dopant segregation. Careful observation also shows that the brighter or darker regions do not correlate with the location of segregation *i.e.* the Nd-rich grain boundaries cannot be discerned in the PL maps. This can be explained by considering the significantly different wavelengths and penetration depth (activation volume) of electrons and photons. The penetration depth of the electrons is estimated to be about  $1\text{ }\mu\text{m}$  while the photons can activate the entire thickness ( $1\text{ mm}$ ) of the translucent samples. The lack of uniformity of the PL is due to differences in regional Nd concentration. It is likely that luminescence is quenched at agglomerated regions where the Nd concentration is high and energy is transferred through cross relaxation in neighboring Nd ions rather than through photon emission.

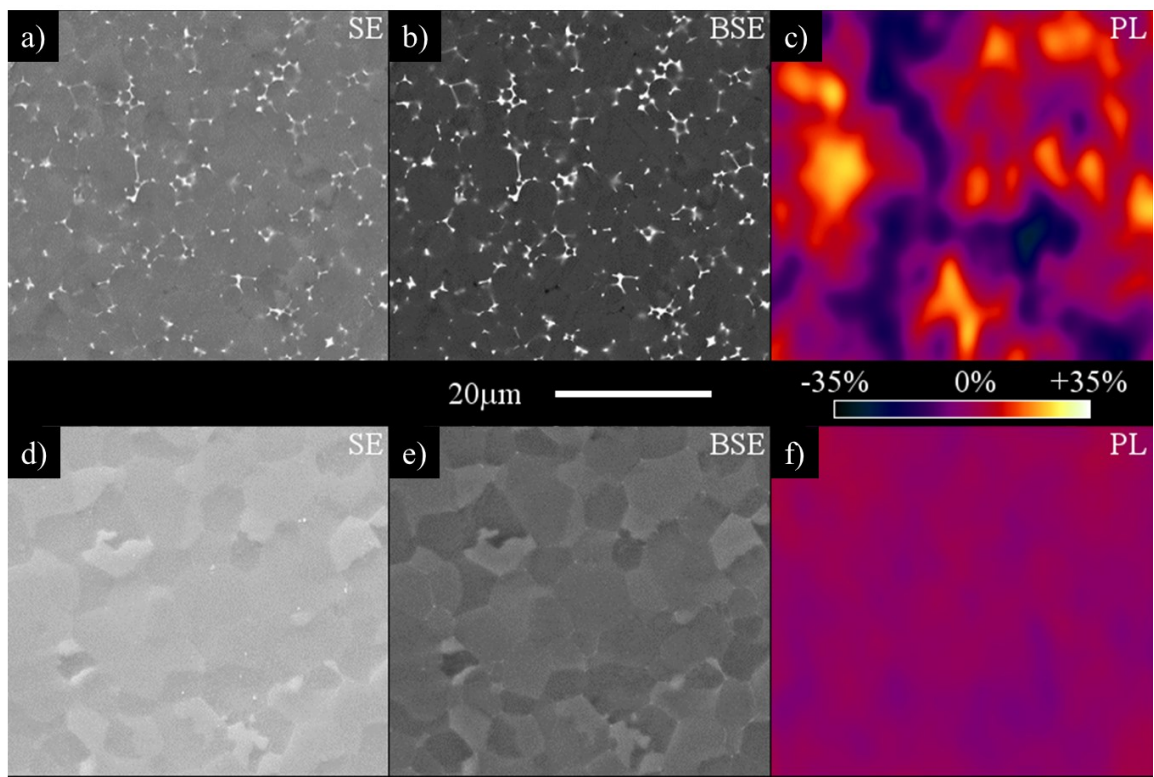


**Figure 3.4:** SEM (SE and BSE) micrographs and photoluminescence maps for Nd:AlN. **(a,b,c)** Maps taken at the same location for Sample 1. **(d, e, f)** Maps taken at the same location for Sample 2. The SEM reveals significantly less dopant segregation in Sample 2 compared to Sample 1. The luminescence maps were taken using narrow band excitation at 808 nm and monitoring at 1064 nm.

### 3.5 Absorption and Emission Spectra

Spatially homogeneous luminescence, such as that observed in our homogeneously doped Nd:AlN, is a key requisite for most photonic applications. We therefore focus on sample 2 and, in the following, present detailed emission spectroscopy resulting from continuous wave (CW at  $\lambda = 808$  nm) and pulsed excitation ( $\lambda = 700 - 1000$  nm). Figure 3.5a shows the luminescence spectrum for 0.5 Nd:AlN (sample 2) under CW 808 nm (diode laser) excitation. The inset shows a picture of the translucent ceramic (Sample 2). The spectrum shows two groups of relatively well-defined peaks in the vicinity of 1080 nm and 1350 nm. Similarly, Figure 3.5b shows luminescent spectra for Nd-doped commercial host materials; Nd:Glass and single crystal Nd:YAG both showing the 2 groups of lines near 1070 and 1350 nm that have been previously attributed to  $^4F_{3/2} \rightarrow ^4I_{11/2}$  and  $^4F_{3/2} \rightarrow ^4I_{13/2}$  electronic transitions of Nd. The Nd:YAG shows multiple sharp well-defined lines while the Nd:Glass displays only two inhomogeneously broadened lines. This is expected since the number as well as width of luminescent lines depends on the host symmetry and inhomogeneous broadening can be attributed to the amorphous structure of glass.

When compared to Nd:YAG and Nd:Glass, our homogeneously doped Nd:AlN exhibits more, better-defined lines than in Nd:Glass but fewer and broader lines compared to single crystal Nd:YAG. In addition, comparison reveals a shift in the location of the maximum intensity peak for all 3 Nd host materials; the maximum peak for Nd:AlN is red shifted by 9 nm relative to Nd:YAG.

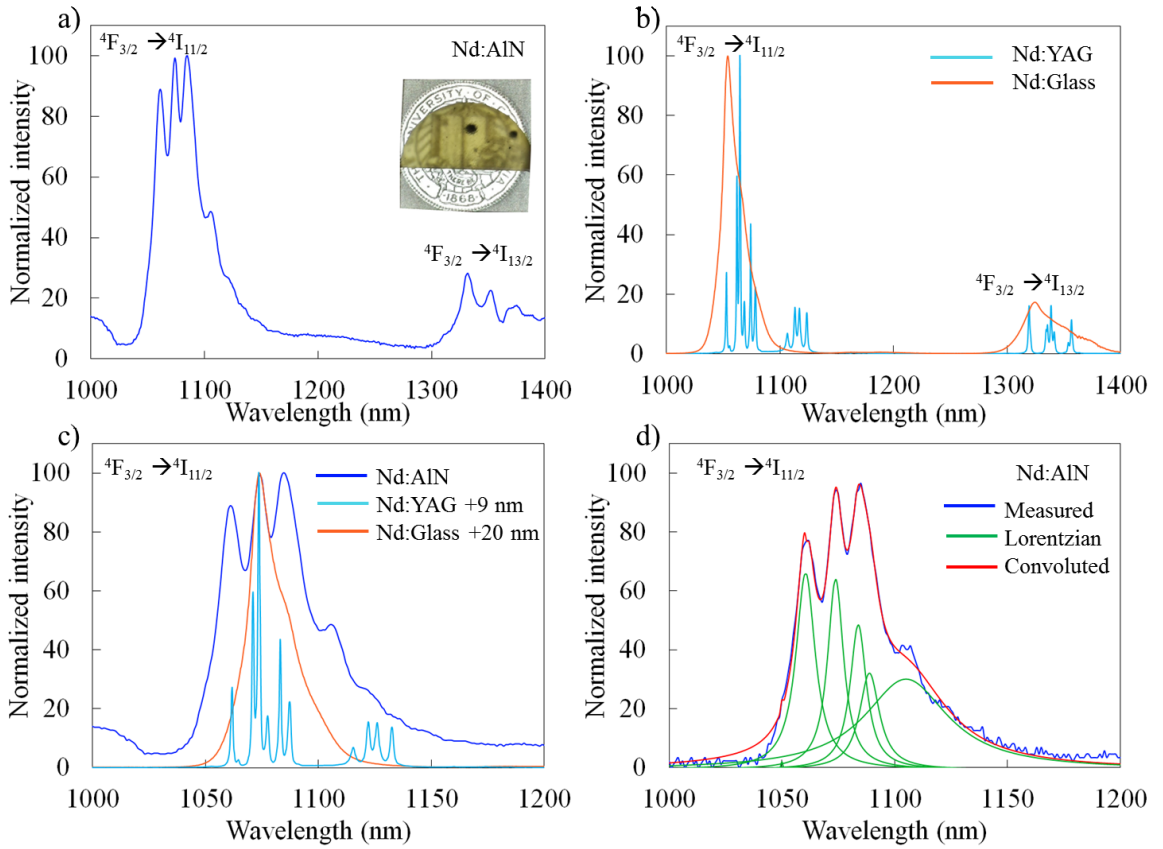


**Figure 3.5:** Luminescence spectra for various samples taken with 808 nm diode excitation **(a)** 0.5 at% Nd:AlN. Inset: Picture of Nd:AlN sample **(b)** Emission spectra for commercially available Nd:Glass and single crystal Nd:YAG **(c)** 0.5 at% Nd:AlN (Sample 2) plotted together with commercially available Nd:YAG and Nd:Glass whose spectra have been red shifted by 9 nm and 20 nm respectively. **(d)** Lorentzian deconvolution of 0.5 at% Nd:AlN spectra showing homogeneous broadening characteristic of phonon broadening.

To directly compare the peak shapes and positions, we plot the spectrum for Nd:AlN along with the Nd:YAG red shifted by 9 nm and Nd:Glass red shifted by 20 nm in Figure 3.5c. It is clear that the emission from Nd:AlN is significantly broader, forming an ‘envelope’ around both the glass and the single crystal emission lines. In order to determine if the Nd:AlN lines are homogeneously or inhomogeneously broadened we plot the deconvolution of the spectrum into Lorentzian peaks in Figure 3.5d. The excellent fit with a Lorentzian profile ( $R^2 = 0.994$ ) suggests that the emission lines are broadened through phonon effects (thermal broadening) and not caused by significant randomness in structure like in a glass host.

In our homogeneously doped sample, we also measured the photoluminescence resulting from femtosecond laser pulses. Figure 3.6 shows luminescence excitation-emission maps taken under short optical pulses at 72 K and 300 K. These are normalized by the maximum (brightest) emission peak over the entire region of interest: excitation at 725 – 900 nm (1.71 – 1.38 eV) and emission at 1000 to 1400 nm (1.24 – 0.89 eV) covering both the  ${}^4F_{3/2} \rightarrow {}^4I_{11/2}$  and  ${}^4F_{3/2} \rightarrow {}^4I_{13/2}$  transitions. At 72 K, the most intense emission is due to the  ${}^4F_{3/2} \rightarrow {}^4I_{11/2}$  transition (with a maximum at 1077 nm) while exciting between 730-750 nm. Excitation at ~800 nm causes the second brightest emission from the same transition at 72 K. Two more excitation regions (~825 and ~860 nm) cause reasonable emission in the same region as the excitation energy is further lowered. Interestingly when exciting near 825 nm, the line at 1105 nm becomes comparable to the 1077 nm peak that is dominant for all other regions.

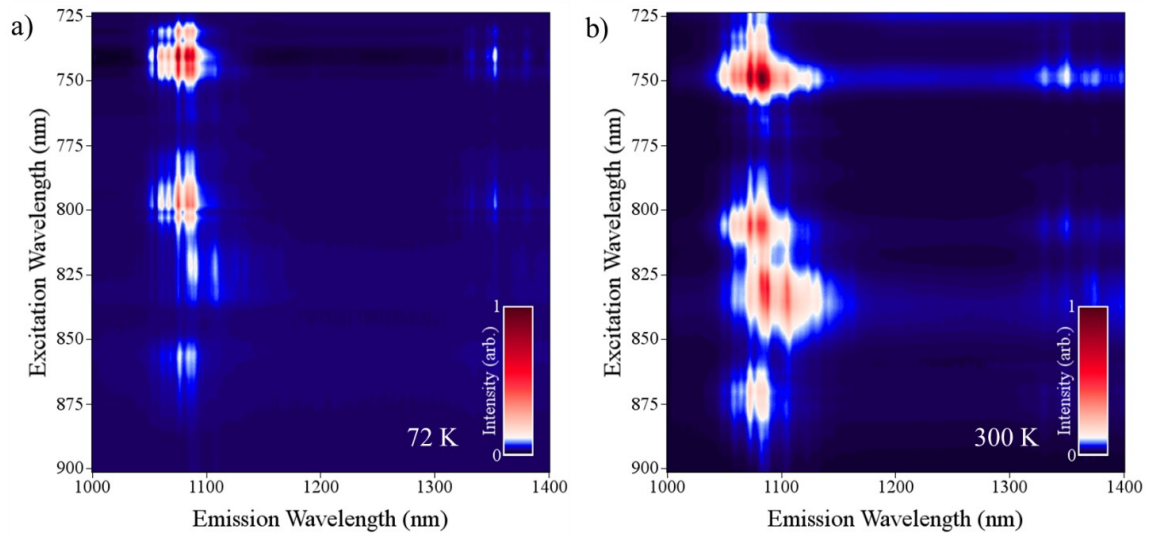


**Figure 3.6:** Luminescence vs. excitation maps for 0.5 at. % Nd:AlN (Sample 2) taken with tunable laser pulse excitation at different temperatures. The intensities are normalized by the maximum (brightest) global emission peak. (a) 300 K and (b) 72 K.

The 300 K luminescence maps show the brightest emission in four similar regions to those observed at 72 K. The greatest difference is the much broader emission bandwidth as expected from phonon broadening. Another difference is that the three lower energy excitation bands are wider and seem to be accessible at lower excitation energies (down to 875 nm). The emission at 1105 nm has increased to the point that it rivals the overall intensity of the 1077 line observed at higher energy excitation ( $\sim 750$  and  $\sim 800$  nm).

The effect of excitation wavelength on emission is more easily appreciated in the PL maps plotted in Figure 3.7. These maps are similar to those in Figure 3.6 but are normalized to the maximum intensity of each excitation wavelength instead of the global intensity. Thus, the brighter the color, the more intense the emission for a given excitation wavelength. At 72K, the 1077 line is the dominant for almost all excitation wavelengths. However, in the region of  $\sim 825$  to  $\sim 840$  nm the line at 1105 nm rivals the 1077 emission as observed previously in Figure 3.6.

The observed broadening under laser excitation may arise from Nd situated on multiple locations within the Nd:AlN microstructure. AlN has the wurtzite structure and we presume that in AlN,  $\text{Nd}^{3+}$  would dope onto the  $\text{Al}^{3+}$  sites. In this structure, the Al sites are all equivalent (Al sites are surrounded by four nitrogen atoms forming a distorted tetrahedron), thus Nd substituted on Al sites should be indistinguishable if no other defects are formed. However, if Nd dopants are associated with vacancies or interstitials distinguishable sites arise. Previous work by Metcalfe *et al.* identified one dominant Nd site and two minority sites in epitaxial Nd:AlN films<sup>6</sup>. They also observed broad emission (< 50 nm) at room temperature although their reported emission

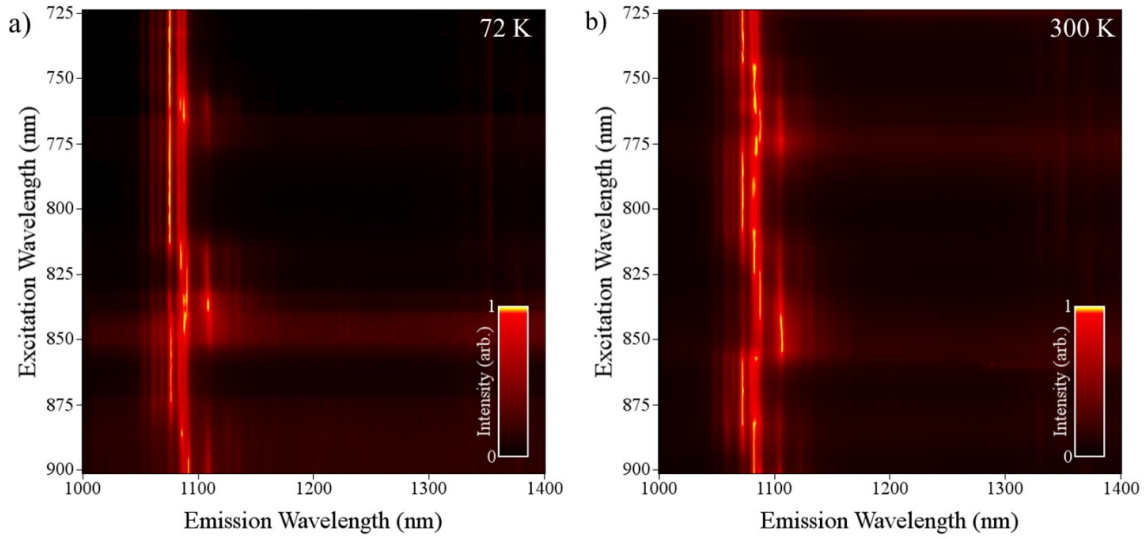


**Figure 3.7:** Luminescence vs. excitation maps for 0.5 Nd:AlN (sample 2) taken with tunable laser pulse excitation at different temperatures. The intensities are normalized by maximum intensity for each excitation wavelength. **(a)** 72 K and **(b)** 300 K. Emission at 1077 nm dominates for nearly all excitation wavelengths except in the 825–840 nm excitation range where 1105 nm emission nearly rivals 1077 nm emission observed at other excitation wavelengths. This observation suggests the possibility for tuning based on pump wavelength.

was red shifted compared to the present work. Epitaxial thin films often have emission shifts compared to bulk crystals caused by lattice strain. Multiple RE sites were also observed in previous work on AlN ceramics doped with Er<sup>7</sup>. Nd associated with grain boundary regions in polycrystalline ceramics are also likely alternative sites.

In addition to thermal broadening, we must also consider natural birefringence of the AlN lattice, which may contribute to linewidth broadening. AlN has hexagonal symmetry leading to anisotropy in both absorption and emission. In our polycrystalline samples, the luminescence is likely the spatially averaged emission of individual randomly oriented grains. Such anisotropic effects have been observed previously in other non-cubic Nd hosts<sup>8-10</sup>.

### 3.6 Conclusion

Although laser media with very broad emission leading to a high tunability range are typically transition metal based (e.g., Ti:Sapphire Ti:Al<sub>2</sub>O<sub>3</sub>), successful RE-based tunable lasers have been demonstrated. Stoneman and Esterowitz demonstrated continuous tunable lasers based on Tm:YAG and Tm:YSGG<sup>11</sup>. The emission spectra of Tm:YAG shows overlapping lines caused by considerable phonon broadening and high multiplicity the Stark levels of the 4f electron provides, resulting in laser tunability from 1870 to 2160 nm<sup>11</sup>. It is possible that the overlapping phonon broadened lines we observe (Figure 3.5) could lead to similar tunability in the 1050 to 1150 nm range. Interestingly, the excitation-emission map of Figure 3.7 reveals that one can tune the location of brightest intensity by carefully choosing the excitation wavelength, and at 300 K, the dominant line is more sensitive to excitation wavelength. It may be possible to exploit

this feature to produce a laser tunable in this relatively large range. Finally, we note the possibility that our homogeneously doped Nd:AlN could also be used to produce lasing at two wavelengths (so called bichromatic lasing) similar to that observed in some Nd doped fluoride glasses<sup>12</sup>.

In summary, we have investigated the spatial distribution of PL for samples produced using different procedures. The sample with the more uniform dopant distribution resulted in significantly more uniform PL distribution. CW diode excitation of the Nd:AlN ceramics showed significantly broader bandwidth than either Nd:YAG or Nd:Glass. We attribute the broadened lines to a combination of multiple Nd sites, polycrystallinity and thermal broadening. The results demonstrate that Nd:AlN might hold interesting potential for producing short pulses and/or tunability over a relatively broad range. Luminescence maps also suggest the exciting opportunity for emission tunability by controlling excitation wavelength.

## REFERENCES

1. Geusic, J.E., Marcos , H.M., and Van Uitert, L.G. “Laser oscillations in Nd-doped yttrium aluminum, yttrium gallium and gadolinium garnets.” *Appl. Phys. Lett.* **4**, 182–184 (1964).
2. Paschotta, R. “Neodymium-doped gain media.” *RP Photonics Encyclopedia*. [https://www.rp-photonics.com/neodymium\\_doped\\_gain\\_media.html](https://www.rp-photonics.com/neodymium_doped_gain_media.html)
3. Kodera, Y., Yamamoto, T., Toyofuku, N., Ohyanagi, M., and Munir, Z. A. “Role of disorder-order transformation in consolidation of ceramics.” *J. Mater. Sci.* **41**, 727–732 (2006).
4. Y. Kodera, C. L. Hardin, and J. E. Garay, “Transmitting, emitting and controlling light: Processing of transparent ceramics using current-activated pressure-assisted densification.” *Scr. Mater.* **69**, 149–154 (2013).
5. J. E. Garay, “Current-Activated, Pressure-Assisted Densification of Materials.” *Annu. Rev. Mater. Res.* **40**, 445–468 (2010).
6. G. D. Metcalfe, E. D. Readinger, R. Enck, H. Shen, M. Wraback, N. T. Woodward, J. Poplawsky and V. Dierolf, “Near-infrared photoluminescence properties of neodymium in in situ doped AlN grown using plasma-assisted molecular beam epitaxy.” *Opt. Mater. Express* **1**(1), 78 (2011).
7. Merkle, L. D. et al. “Fluorescence of Er<sup>3+</sup>: AlN polycrystalline ceramic.” *Opt. Mater. Express* **2**, 721-727 (2008).
8. Yaney, P.P. and DeShazer, L. G. “Spectroscopic studies and analysis of the laser states of Nd<sup>3+</sup> in YVO<sub>4</sub>.” *J. Opt. Soc. Am.* **66**, 1405 (1976).
9. Ikonnikov, D. A. et al. “Spectroscopic properties of Nd<sup>3+</sup> in orthorhombic δ-BiB<sub>3</sub>O<sub>6</sub> crystal.” *Opt. Mater.* **34**, 1839–1842 (2012).
10. Weber, M.J., Bass M., Andringa, K., Monchamp, R.R., and Comperchio, E. Czochralski, “Growth and Properties of YAlO<sub>3</sub> Laser Crystals.” *Appl. Phys. Lett.* **15**, 342 (1969);
11. R. C. Stoneman and L. Esterowitz, “Efficient, broadly tunable, laser-pumped Tm:YAG and Tm:YSGG cw lasers.” *Opt. Lett.* **15**, 486 (1990).
12. J. Azkargorta, I. Iparraguirre, R. Balda and J. Fernández, “On the origin of bichromatic laser emission in Nd<sup>3+</sup>-doped fluoride glasses.” *Opt. Express* **16**(16), 11894 (2008).

## Chapter 4

### Carrier Multiplication Using 2D Heterostructures

#### 4.1 Electronic engineering at the nanoscale

The discovery of graphene and other layered materials in the late aughts heralded a new era in condensed matter physics, promising almost boundless possibilities for construction of novel electronic systems. These materials are characterized by strong covalent bonds in plane, but only weak van der Waals bonds out of plane, making it possible to separate arbitrary numbers of layers from bulk samples and then combine them with other layered materials to create nanoscale heterostructures. The band structure of many van der Waals materials also depends strongly on layer thickness, meaning a monolayer sample will behave differently than a bilayer, trilayer, etc. This control over electronic structures at the nanoscale is truly unprecedented. Strong electronic interactions can result in novel particle-antiparticle (electron-hole) pair generation effects<sup>1</sup>, which may be exploited to enhance the photoresponse of nanoscale optoelectronic devices.

Highly efficient electron-hole (*e-h*) pair multiplication has been demonstrated in several important nanoscale systems including nanocrystal quantum dots<sup>2-6</sup>, carbon nanotubes<sup>7-9</sup>, and graphene<sup>10-13</sup>. The small Fermi velocity and nonlocal nature of the effective dielectric screening in ultra-thin layers of transition metal dichalcogenides (TMDs) indicates that electron and hole interactions are very strong<sup>14-16</sup> and, thus, high efficiency generation of *e-h* pairs from hot electrons is expected. However, such *e-h* pair multiplication has not been observed in two-dimensional (2D) TMD devices. In this

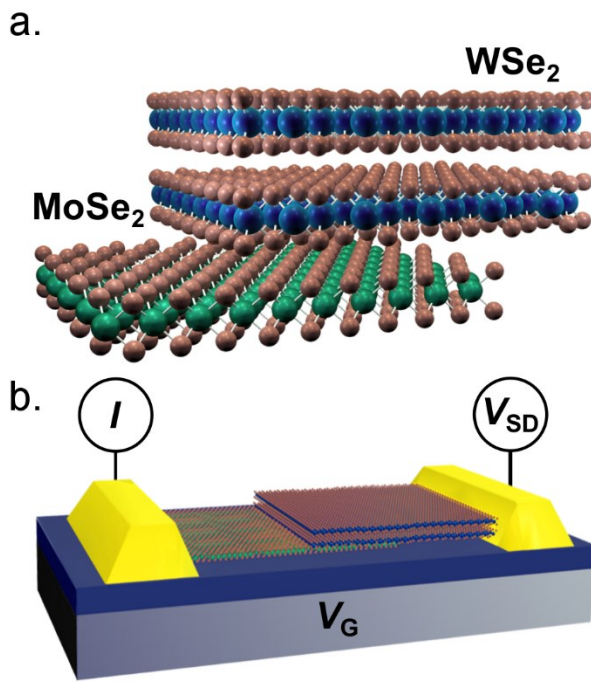


**Figure 4.1:** TMD device geometry. **a**, Schematic of the atomic layer heterostructure. **(b)** The  $n^+-n$  heterojunction device.

chapter, we discuss an experiment utilizing bandgap engineered atomic layer heterostructures to induce highly efficient multiplication of interlayer *e-h* pairs in 2D semiconductor heterostructure photocells.

#### 4.2 Basic experimental picture

We studied electron-hole pair multiplication in 2D heterostructures of monolayer molybdenum diselenide ( $\text{MoSe}_2$ ) and bilayer tungsten diselenide ( $\text{WSe}_2$ ) integrated into field-effect heterojunction devices (Figure 4.1a). A back-gate voltage  $V_G$  allows electrostatic doping of the  $\text{MoSe}_2/\text{WSe}_2$  interface, which is produced by mechanical exfoliation of bulk TMD crystals followed by van der Waals-mediated pick-up, dry transfer, and high vacuum annealing (detailed in the next section). Assembling the heterostructure results in an interfacial potential energy difference  $\Delta E_c^0$  ( $\Delta E_v^0$ ) of the two conduction (valence) bands (Fig. 4.2). An electron transferred from  $\text{WSe}_2$  into  $\text{MoSe}_2$  experiences the potential energy drop, while an electron travelling in the opposite direction must gain energy to overcome the potential energy barrier  $\Delta E_c^0$ . At the heterostructure interface, the energy difference  $\Delta E_h^0$  between the highest valence band and lowest conduction band is the minimum energy required to excite an interlayer *e-h* pair<sup>17-21</sup>.

We confirmed interlayer charge transfer between the TMDs by measuring photoluminescence from the heterostructure. Figure 4.3 shows photoluminescence spectra with a laser wavelength  $\lambda = 532$  nm fixed on the individual TMDs and on the overlapped region at  $T = 300$  K. In the monolayer  $\text{MoSe}_2$  (green line, Fig. 4.3),

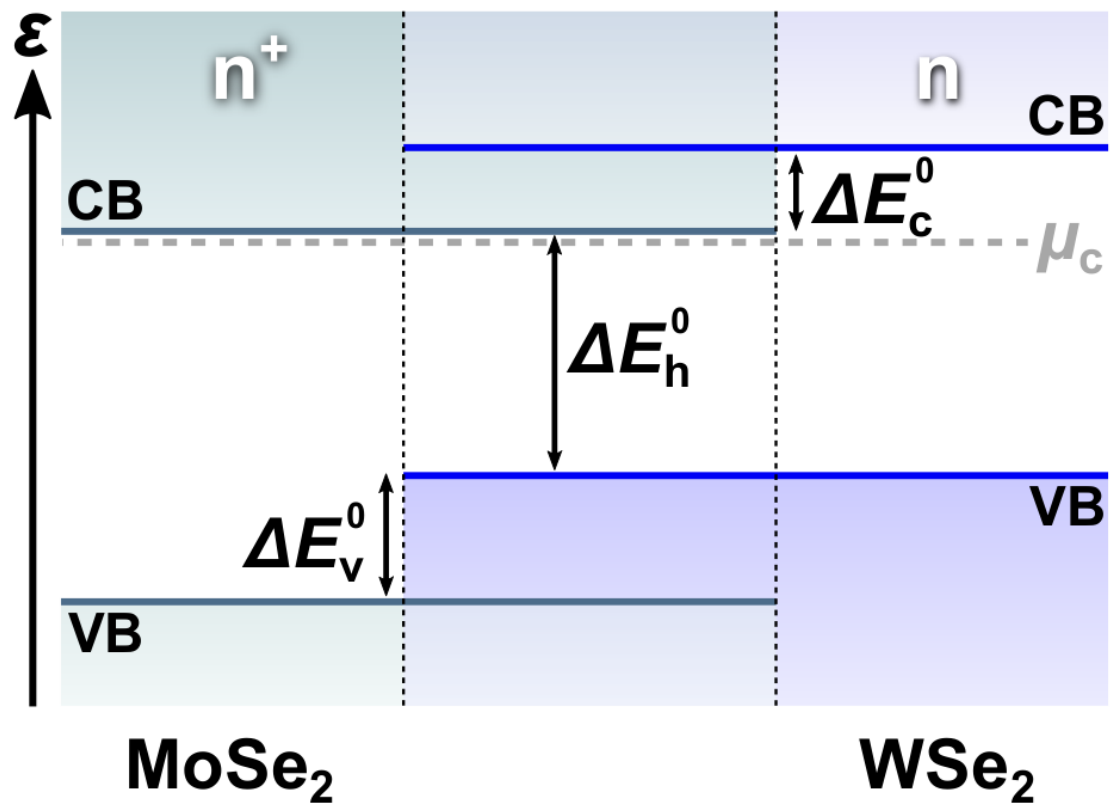


**Figure 4.2:** MoSe<sub>2</sub>-WSe<sub>2</sub> heterostructure band alignment.

photoluminescence peaks were observed at photon energy  $E_{\text{PH}} = 1.57$  eV and 1.75 eV, while in bilayer WSe<sub>2</sub> (blue line, Fig 4.3), two peaks were observed at  $E_{\text{PH}} = 1.46$  eV and 1.66 eV. When measured in the heterostructure overlap region, we observed strong suppression of the lowest energy photoluminescence peak (originating from the WSe<sub>2</sub>), and an order of magnitude decrease of the peaks at 1.55 eV and 1.64 eV. Such photoluminescence suppression, which was typical of the devices measured here (Fig. 4.5), has been studied previously<sup>17-20, 22</sup> and is attributed to charge redistribution and the formation of spatially indirect, bound *e-h* pairs at the interface.

#### 4.3 MoSe<sub>2</sub>/2L-WSe<sub>2</sub> heterostructure synthesis

Before diving too deeply into the physics of the project, we'll describe the methods used to make and measure these devices. We fabricated MoSe<sub>2</sub>/2L-WSe<sub>2</sub> heterostructures by mechanical exfoliation of WSe<sub>2</sub> and MoSe<sub>2</sub> flakes from bulk crystals (purchased from 2D Semiconductor) onto Si wafers coated with 290nm-thick SiO<sub>2</sub>. The heterostructure devices were assembled using a highly customized, temperature-controlled transfer microscope that ensures that the interface between the two layers has no intentional contact to polymer films. The dry pick-up transfer process, described below, results in a heterostructure with minimal interfacial contamination, and is followed by two annealing processes.

The van der Waals pick-up and transfer process is based on Andres Castellanos-Gomez, et al.<sup>1</sup>, and is represented schematically in Figure 4.4 to highlight key distinctions of this work. We first use a stamp to pick up the target layer, (Fig. 4.4a, top). The stamp consists of a thin layer of polypropylene carbonate (PPC) and a layer of

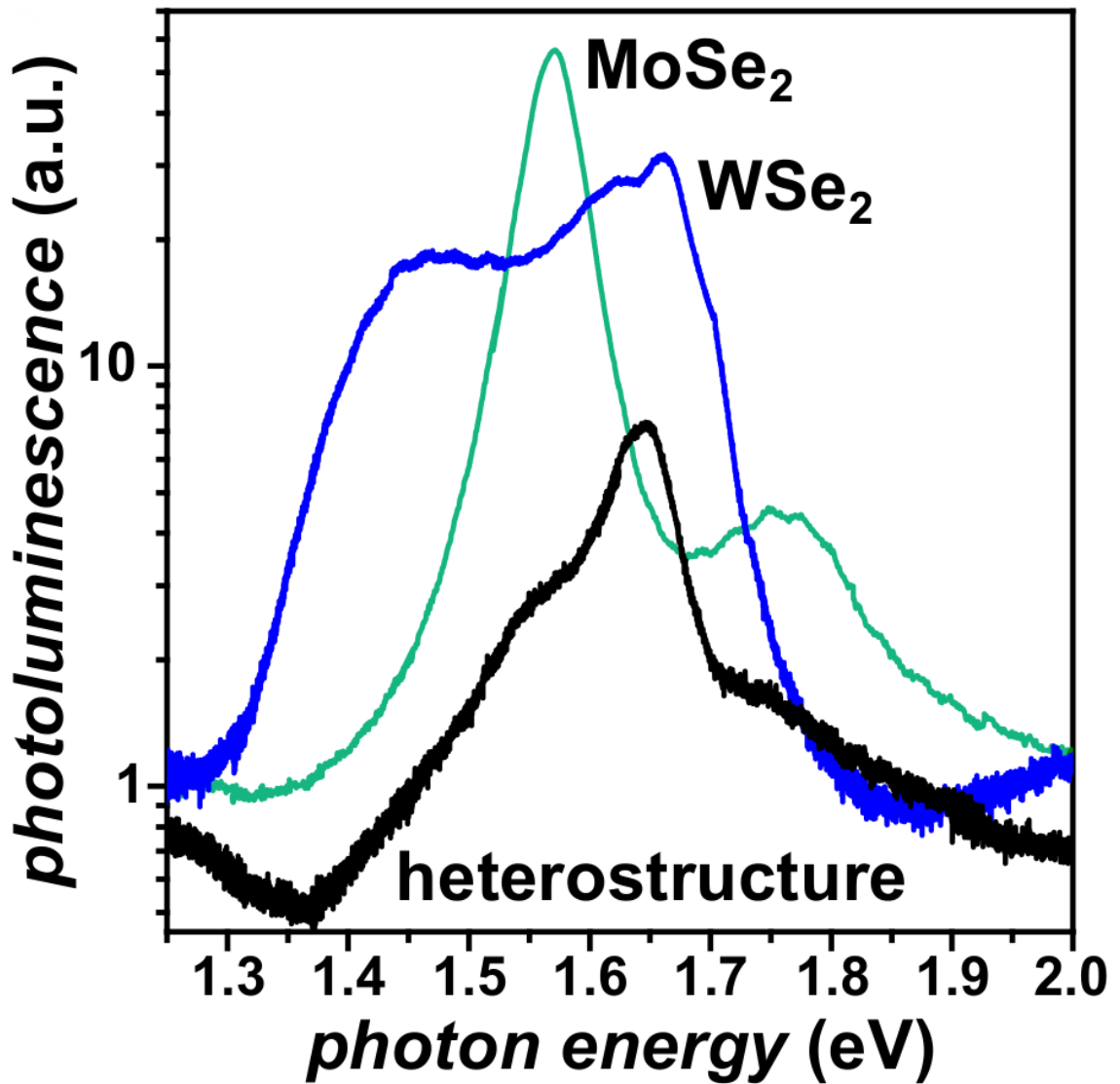


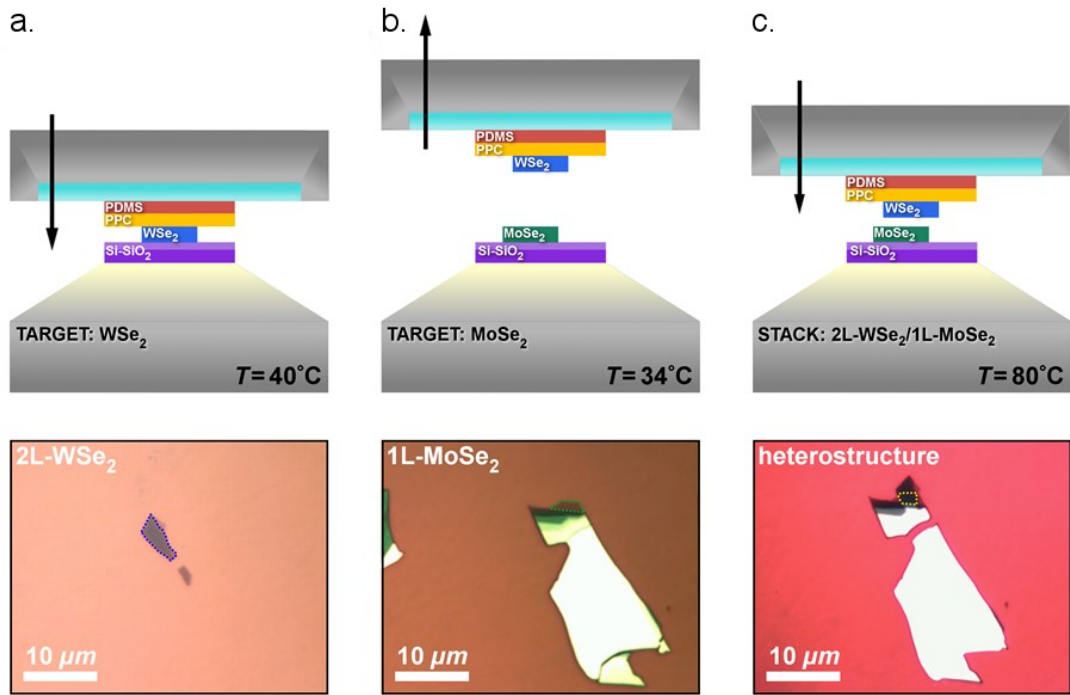
**Figure 4.3:** Photoluminescence of MoSe<sub>2</sub> (teal), WSe<sub>2</sub> (blue), and heterostructure region (black).

polydimethylsiloxane (PDMS) on top of a glass slide. The stamp is lowered until the PPC contacts the first target layer, WSe<sub>2</sub>. We then heat the stage to 40° C. We next cool the stage to 34°C and very quickly lift the stamp, as shown in Figure 4.4b (top). To assemble the heterostructure, we lower the WSe<sub>2</sub> flake and place it on to the MoSe<sub>2</sub> flake on the stage as shown in Figure 4.4c (top). The stage is then heated to 80°C to melt the PPC and the stamp is lifted very slowly, causing the PPC to separate from the PDMS. This leaves the stack of two flakes with PPC on top. We remove the residual PPC using heated acetone. Figure 4.4 (a, and b), bottom, show optical images of exfoliated flakes of WSe<sub>2</sub> and MoSe<sub>2</sub>. Dashed lines highlight the individual layers and overlapped region of the completed heterostructure.

#### 4.4 Spectroscopic characterization

In this section, we present comprehensive characterization of heterostructures composed of monolayer molybdenum diselenide (MoSe<sub>2</sub>) and bilayer tungsten diselenide (2L-WSe<sub>2</sub>). We include detailed descriptions of optical and optoelectronic spectroscopy measurements on two devices that have been thoroughly characterized using all of the techniques described. All experimental results were typical of Devices 1 and 2.

The devices, shown in Figure 4.5, were first characterized to identify layer thickness and ensure interlayer coupling, as determined through Raman and photoluminescence (PL) spectroscopy. Many heterostructures were assembled, and only those exhibiting the PL signatures indicative of electron transfer and equilibrium charge redistribution between the layers (Neil R. Wilson, et al.)<sup>2</sup> were selected for comprehensive measurements.



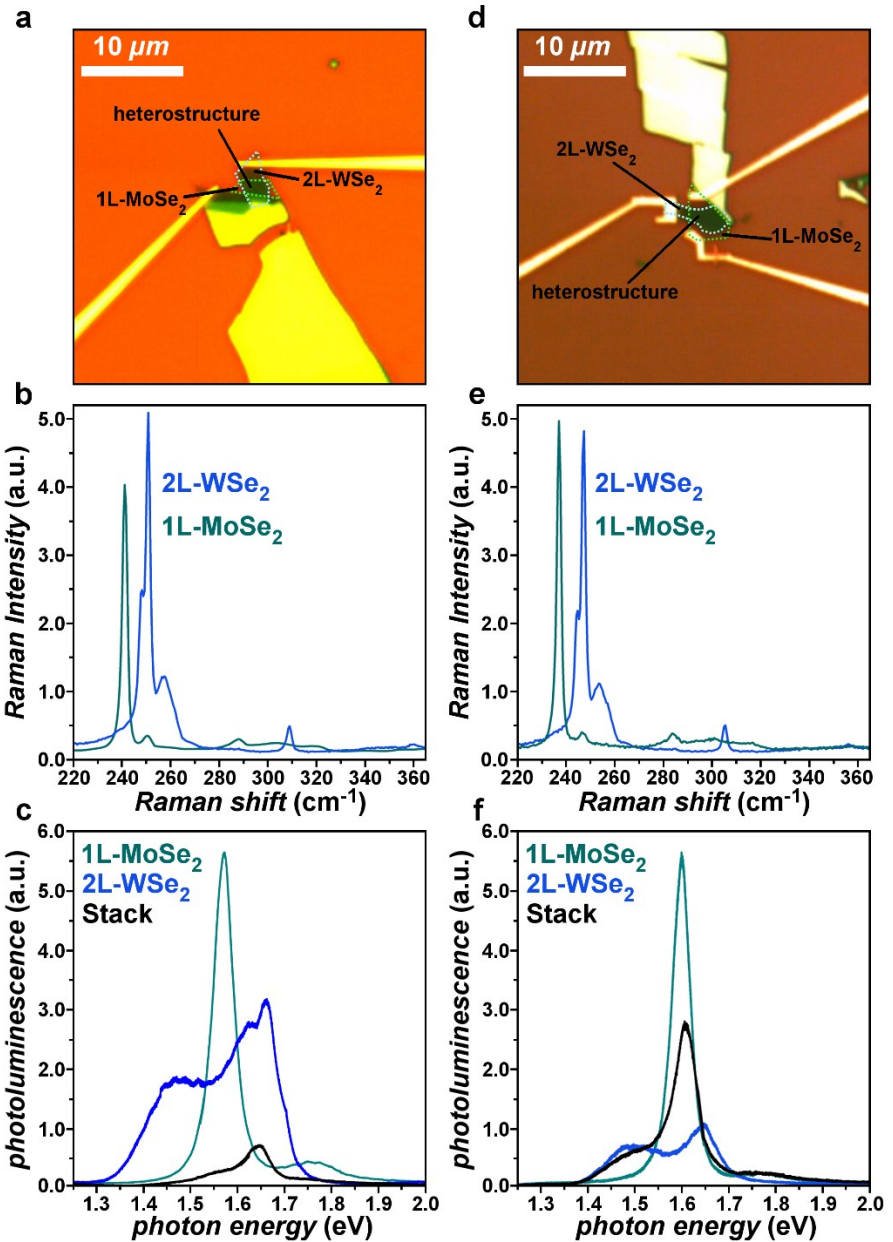
**Figure 4.4:** Schematic illustration and optical images of the dry-transfer process. **(a, b, c) top**, Schematic illustration of the transfer microscope at different temperatures for different purposes. **(a, b, c) bottom**, Optical images of exfoliated flakes of WSe<sub>2</sub>, MoSe<sub>2</sub>, and MoSe<sub>2</sub>/2L-WSe<sub>2</sub> heterostructures respectively. Dashed lines indicate the area of the individual layers and the overlapped region, which are about 14 μm<sup>2</sup>, 8 μm<sup>2</sup>, and 4.3 μm<sup>2</sup> respectively.

Figure S2 shows Raman and photoluminescence spectroscopy measurements that were carried out before and after constructing the heterostructure, as well as electronic transport measurements. No quantitative or qualitative changes were observed before/after transport measurements. Figure 4.5b shows the Raman spectrum for the MoSe<sub>2</sub> and WSe<sub>2</sub> flakes for Device 1. For MoSe<sub>2</sub>, the A<sub>1g</sub> peak at 241 cm<sup>-1</sup>, E<sub>2g</sub><sup>1</sup> peak at 288 cm<sup>-1</sup>, and lack of B<sub>2g</sub><sup>1</sup> peak between 350 and 360 cm<sup>-1</sup> are characteristic of monolayer thickness<sup>32</sup>. The Raman spectrum of the WSe<sub>2</sub> flake shows the A<sub>1g</sub> mode at 250 cm<sup>-1</sup> and B<sub>2g</sub><sup>1</sup> mode at 309 cm<sup>-1</sup>, which indicates bilayer thickness<sup>2</sup>.

The PL spectra of the heterostructure devices show several key features that indicate interlayer electron transfer and equilibrium charge redistribution between the layers in the heterostructure (Pasqual Rivera, et al.<sup>4</sup>, Frank Ceballos, et al.<sup>5</sup>). Figure 4.5c shows the photoluminescence (PL) spectra of MoSe<sub>2</sub>, 2L-WSe<sub>2</sub>, and the heterostructure. The PL emission of MoSe<sub>2</sub> has a large peak at 1.57 eV and a shoulder at 1.75 eV, while the 2L-WSe<sub>2</sub> exhibits two peaks at 1.46 eV and 1.66 eV, in agreement with previously reported data<sup>2</sup>. Figure 4.5 (d, e, and f) shows characterization data for a second 2L-WSe<sub>2</sub>/MoSe<sub>2</sub> heterostructure, Device 2. Raman spectra and PL are again in agreement with the results of Tonndorf *et al.*<sup>3</sup>.

#### 4.5 Annealing process

After devices were placed into high vacuum (10<sup>-6</sup> torr), we first annealed the samples at 420°C for 48 hours to improve device contact quality and remove surface contaminants (Marco M. Furchi, et al.<sup>6</sup>). Following this procedure, the devices were kept



**Figure 4.5:** Optical images, Raman spectroscopy, and PL spectroscopy of Devices 1 and 2. **(a, d)** Optical images of the two MoSe<sub>2</sub>/2L-WSe<sub>2</sub> heterostructures with contacts. **(b, e)** Raman spectra (excitation wavelength  $\lambda=532\text{nm}$ ) for MoSe<sub>2</sub> (green), and 2L-WSe<sub>2</sub> (blue). **(c, f)** PL spectra of MoSe<sub>2</sub> (green), 2L-WSe<sub>2</sub> (blue), and the stack (black).

under a  $10^{-6}$  torr vacuum at all times. We carried out scanning photocurrent spectroscopy measurements using the microscope described in Chapter 2. The photocurrent was measured with a diffraction-limited beam spot at various wavelengths over the Ti:sapph laser range (wavelengths 700-1000 nm) and at average powers below 1 mW. After initial photocurrent measurements to assess device contacts, the device resistance and DC current noise was significantly decreased when measured at low and high  $V_{SD}$  voltage. An order of magnitude decrease in resistance was typical after 12-24 hours of sustained scanning photocurrent measurements under vacuum, after which time the device remained stable. Each of the devices described here were measured for more than 60 days and demonstrated stable operation after annealing.

#### 4.6 Photocurrent and differential reflection

After annealing, photocurrent and differential reflection spectra were taken to confirm interlayer coupling at the interface, as determined by the strong correlation with PL spectral features. We measured photocurrent and reflection spectra with a 0.7 mW beam focused to a diffraction-limited 500 nm diameter (FWHM) spot. Figure 4.6a shows photocurrent (red),  $\Delta R/R$  (blue), and PL (gray) as a function of incident photon energy. The quantity  $\Delta R/R$  is the difference between the reflection at any point and the reflection of the silicon substrate, normalized by the background reflection from the substrate. In Figure S3b we show spatial  $\Delta R/R$  maps taken at different wavelengths. We observed a clear spatial dependence of  $\Delta R/R$ , and a wavelength-dependent transition from positive, through zero, and then to negative  $\Delta R/R$ . We took the data from the green dot in Figure S3b to plot the  $\Delta R/R$  spectrum in Figure 4.6a. The zero crossing of the  $\Delta R/R$  spectrum

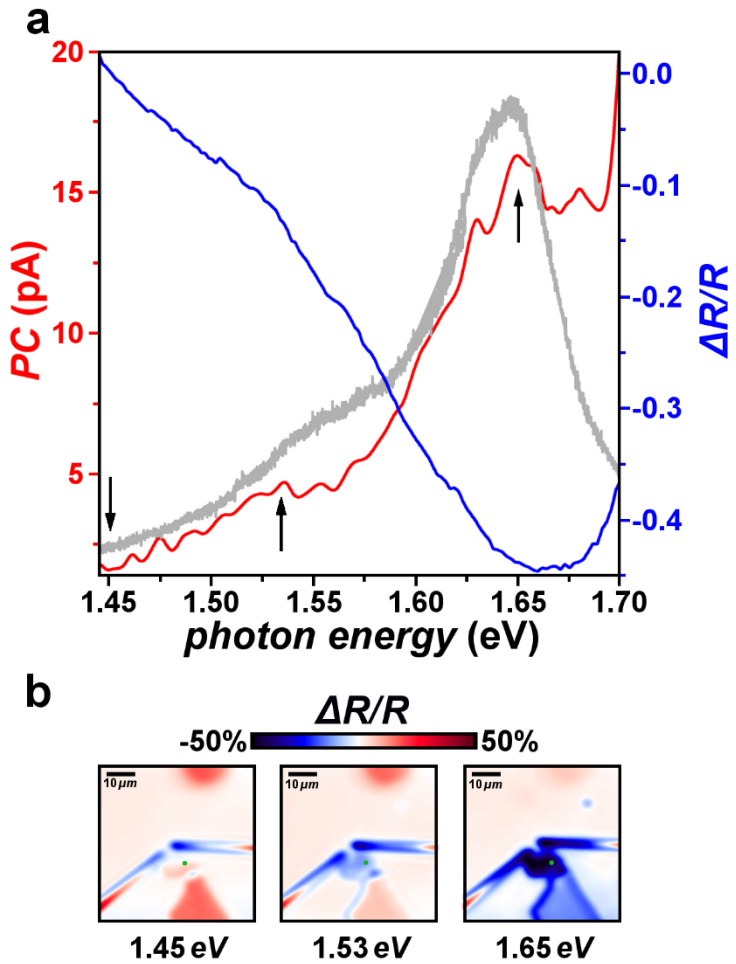


**Figure 4.6:** Differential reflection and photocurrent spectroscopy measurements of Device 1. **(a)** Photocurrent,  $\Delta R/R$ , and PL spectra from  $\text{MoSe}_2/2\text{L}-\text{WSe}_2$  heterostructure illustrated respectively by red, blue, and gray lines. **(b)** Spatial  $\Delta R/R$  maps at different excitation photon energies (labeled).

occurs near 1.45 eV, and a minimum in  $\Delta R/R$  occurs at 1.66 eV, slightly higher in energy than the peak in PL emission. The photocurrent shows a peak near 1.66 eV and continues to increase at higher photon energies.

#### 4.7 Gate and bias dependent interlayer current

We next characterized the device response as a function of applied gate and bias voltage. Figure 4.7 shows interlayer current  $I$  vs.  $V_G$  for the same device at source-drain voltage  $V_{SD} = 0.65$  V. The  $I-V_G$  characteristic demonstrates ordinary unipolar electron-type (*n*-type) semiconductor heterojunction behavior<sup>22</sup>: current that increases monotonically at low  $V_{SD}$  and a well-defined transition from insulating behavior at  $V_G = -50$  V to conducting behavior at  $V_G = 10$  V. From the  $I-V_G$  characteristic, we compute  $d\log I/dV_G$  and find the maximum, which determines the onset gate voltage  $V_{ON} = -35.5$  V. For  $V_G > V_{ON}$ , electrons are transferred through the  $n^+ - n$  heterojunction formed at the interface of the heavily electron-doped ( $n^+$ ) MoSe<sub>2</sub> and lightly electron-doped (*n*) WSe<sub>2</sub><sup>22</sup>.

As  $V_{SD}$  was increased, we observed highly unusual response. Figure 4.8a shows the current  $I$  as a function of  $V_{SD}$  and  $V_G$ . The  $I-V_{SD}$  characteristics (Fig. 4.8b inset) measured in the low-current state exhibit distinct behavior from those in the highly conducting *n*-type transport regime. As  $V_G$  increased, the forward bias  $I-V_{SD}$  characteristics ( $V_{SD} > 0$  V, Fig. 4.8b) increased monotonically as a function of  $V_{SD}$ . In contrast, the reverse bias ( $V_{SD} < 0$  V) current (Fig. 4.8) first increased sharply to a peak value near  $V_{SD} = -4.8$  V (bright feature, Fig. 4.8a) and then decreased at higher  $V_{SD}$ . The non-monotonic behavior in reverse bias emerged for  $V_G > -36$  V. As  $V_G$  increased, the current peak remained at an approximately constant  $V_{SD}$  value.

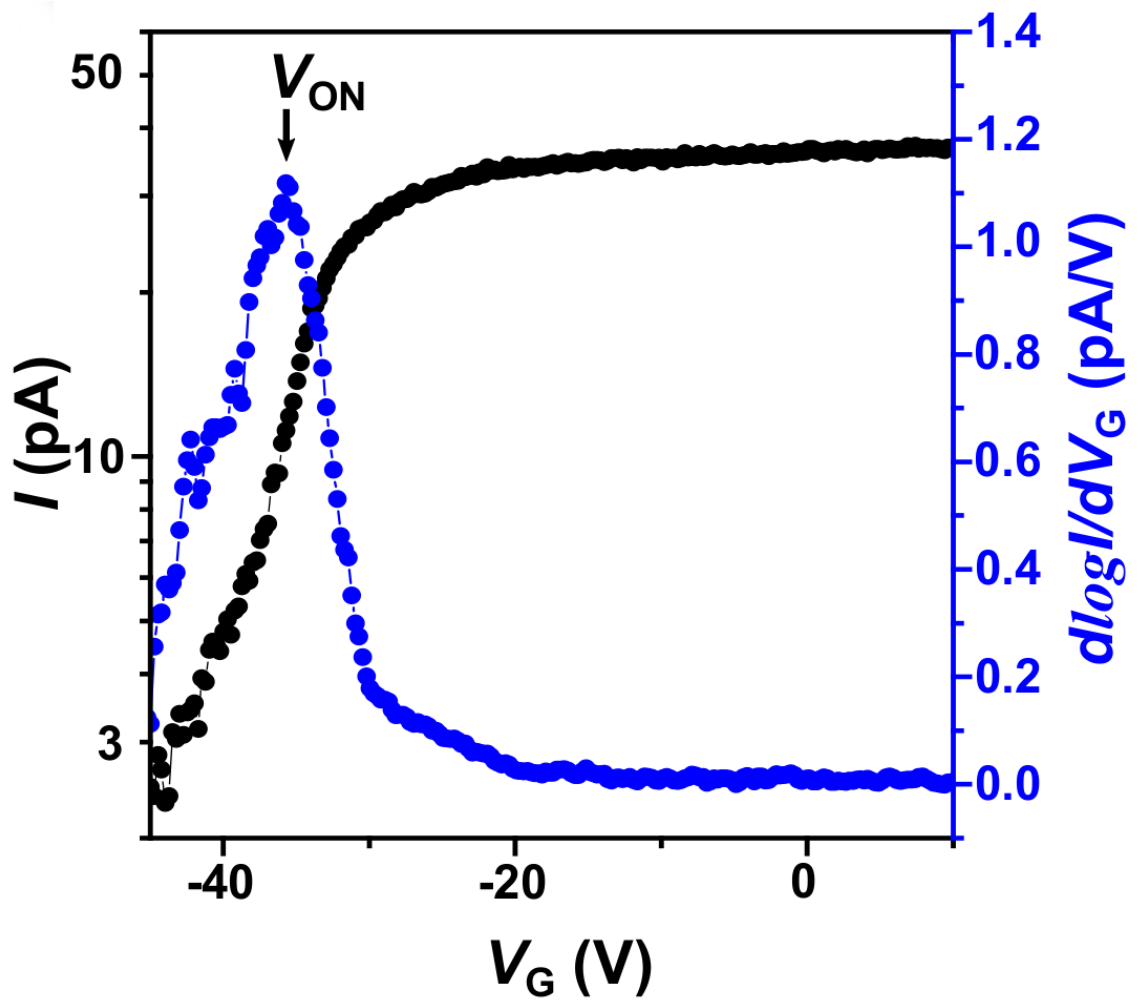


**Figure 4.7:** Gate dependence of device current (black) and  $d\log I / dV_g$  (blue).

In Figure 4.8c, the reverse bias current peak emerges over a range of gate voltages corresponding to an abrupt increase of the interlayer current  $I$ . To examine the emergence of this peak more thoroughly, Figure 4.8d shows differential conductance  $dI/dV_{SD}$  vs.  $V_{SD}$  as a function of gate voltage  $V_G$ . Near  $V_{SD} = -2.5$  V, a maximum in the differential conductance, labeled  $g_M$ , appears as  $V_G$  increases. In contrast, near  $V_{SD} = -5.4$  V, valleys in  $dI/dV_{SD}$  vs.  $V_{SD}$  evolve into prominent negative differential conductance (NDC) for increasing  $V_G$  (labeled with open circles). The onset of NDC, and thus the reverse bias current peak, directly correlates with the  $V_G$ -dependent onset to unipolar electron conduction.

The non-monotonic  $I-V_{SD}$  characteristics arise as the temperature increases and differ strongly from interlayer Zener tunneling behavior<sup>29</sup>. Figure 4.9 shows  $I-V_{SD}$  characteristics as a function of  $V_G$  at several temperatures. Below  $T = 340$  K, the  $I-V_{SD}$  characteristics exhibit no current peak in reverse bias. At and above  $T = 340$  K, however, the reverse bias current peak becomes evident as  $V_G$  is increased (Fig. 4.9a). Importantly, the reverse bias current increased much more rapidly with increasing temperature when compared to the current at  $V_{SD} > 0$  V. At  $T = 360$  K (Fig. 4.9b), the reverse bias current, particularly at low negative  $V_{SD}$ , is approximately two orders of magnitude larger than in forward bias. By rescaling the temperature-dependent reverse bias interlayer current as  $T \ln(I/T^2)$ , the data (for  $V_G > V_{ON}$ ) collapse to a temperature-independent characteristic vs.  $V_{SD}$  (Fig. 4.9c). In forward bias (Fig. 4.9d), a similar temperature-independent characteristic is observed, yet the current must be rescaled as  $T \ln(I/T)$ . In contrast to the temperature-independent current expected for interlayer tunneling across the

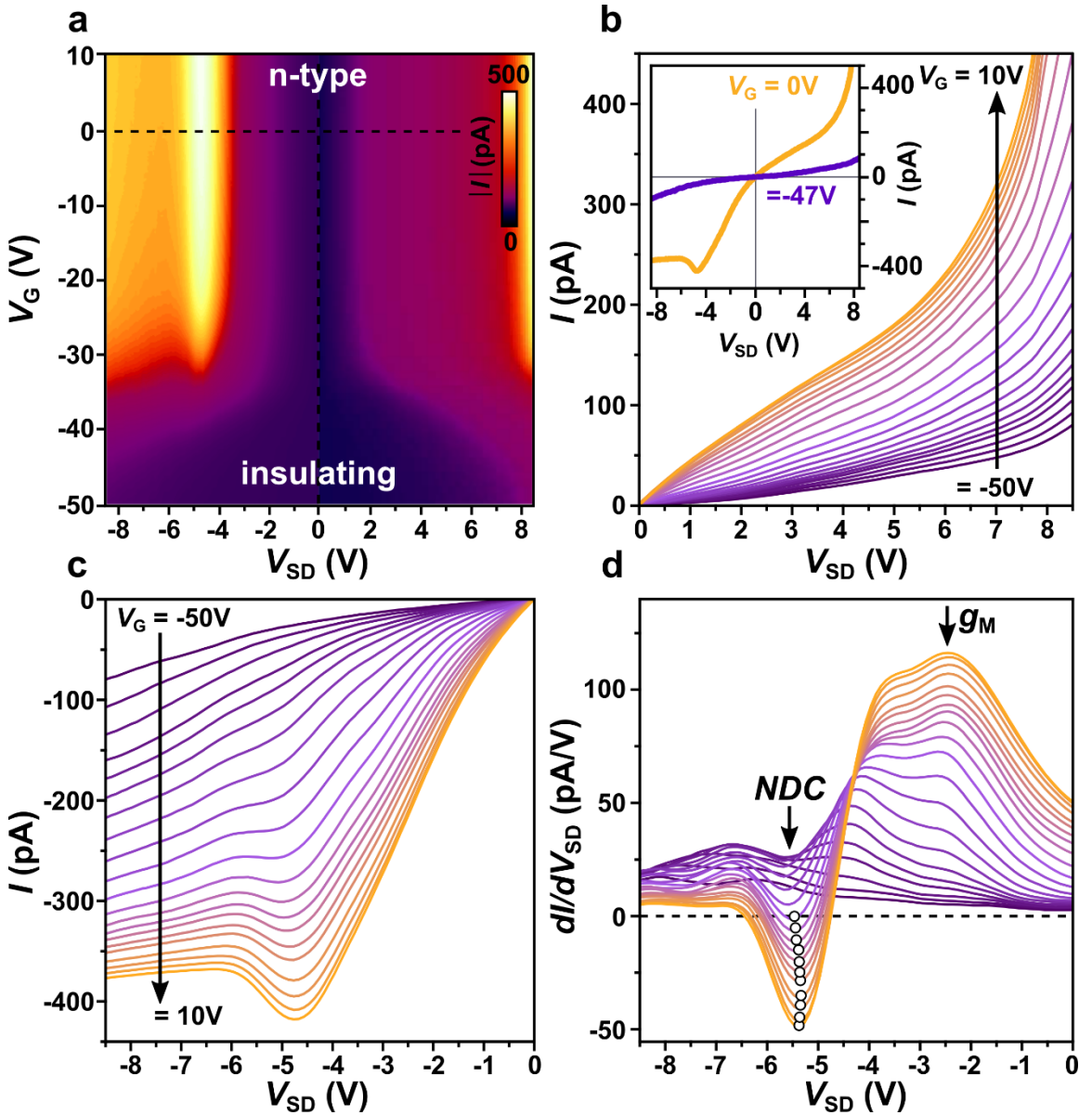


**Figure 4.8:** Gate voltage dependence of the  $I$ - $V_{SD}$  and  $dI/dV_{SD}$  characteristics in the 2D  $n^+$ - $n$  heterojunction device. **(a)** Color map of  $I$  vs.  $V_{SD}$  and  $V_G$  ( $T = 340$  K; heterostructure overlap area  $4.3 \mu\text{m}^2$ ). **(b)** Forward bias  $I$ - $V_{SD}$  characteristics as a function of  $V_G$  (increasing from dark purple to orange, labeled with vertical solid arrow). Inset,  $I$ - $V_{SD}$  characteristics at  $V_G = 0$  and  $V_G = -47$  V (labeled). **(c)** Reverse bias  $I$ - $V_{SD}$  characteristics as a function of  $V_G$ . **(d)**,  $dI/dV_{SD}$  vs.  $V_{SD}$  characteristics ( $T = 340$  K). NDC labels the negative differential conductance peak values (marked with open circles).  $g_M$  is the maximum differential conductance.

interface<sup>29</sup>, the reverse bias interlayer current  $I \propto T^2 \exp(-1/T)$  increases sharply with temperature at low reverse bias, giving rise to a current peak at increased temperatures.

#### 4.8 Interlayer carrier multiplication

We attribute the non-monotonic reverse bias current to interlayer  $e$ - $h$  multiplication by high-energy electrons. In the  $e$ - $h$  pair excitation process requiring the lowest excess energy, an electron in WSe<sub>2</sub> gains the combined energy of the interlayer potential energy  $\Delta E_c^0$  and the kinetic energy of the source-drain electric field to create a low-energy electron in MoSe<sub>2</sub> plus an interlayer  $e$ - $h$  pair (Fig. 4.9e)



The subscript  $W$  or  $Mo$  indicates the layer into which the electron ( $e$ ) or hole ( $h$ ) is transferred. The final three-body state includes an interlayer  $e$ - $h$  pair produced at the interface. The kinetic energy available to an electron  $e_W$  in WSe<sub>2</sub> is given by  $K_e = \Delta E_c$ , where  $\Delta E_c(V_{SD}) = \Delta E_c^0 - e(\alpha V_{SD})$  is the total potential energy drop for the interlayer electron transfer process  $e_W \rightarrow e_{Mo}$ . The potential energy drop can be tuned by changing  $V_{SD}$ , and the factor  $\alpha \leq 1$  is a phenomenological constant included to express the proportionality between electric potential drop and applied voltage (Supplementary S4).

We obtain the temperature and  $V_{SD}$  dependence of the interlayer current  $I$  by a straightforward calculation based on the Landauer formalism (Supriyo Datta 1995<sup>16</sup>). Following Chul-Ho Lee, et al.<sup>22</sup>, we model a 2D  $n$ -type, type II heterojunction in which most of the voltage drop in the device occurs across the vertical junction, leaving no appreciable potential barriers in the lateral transport direction within each semiconductor

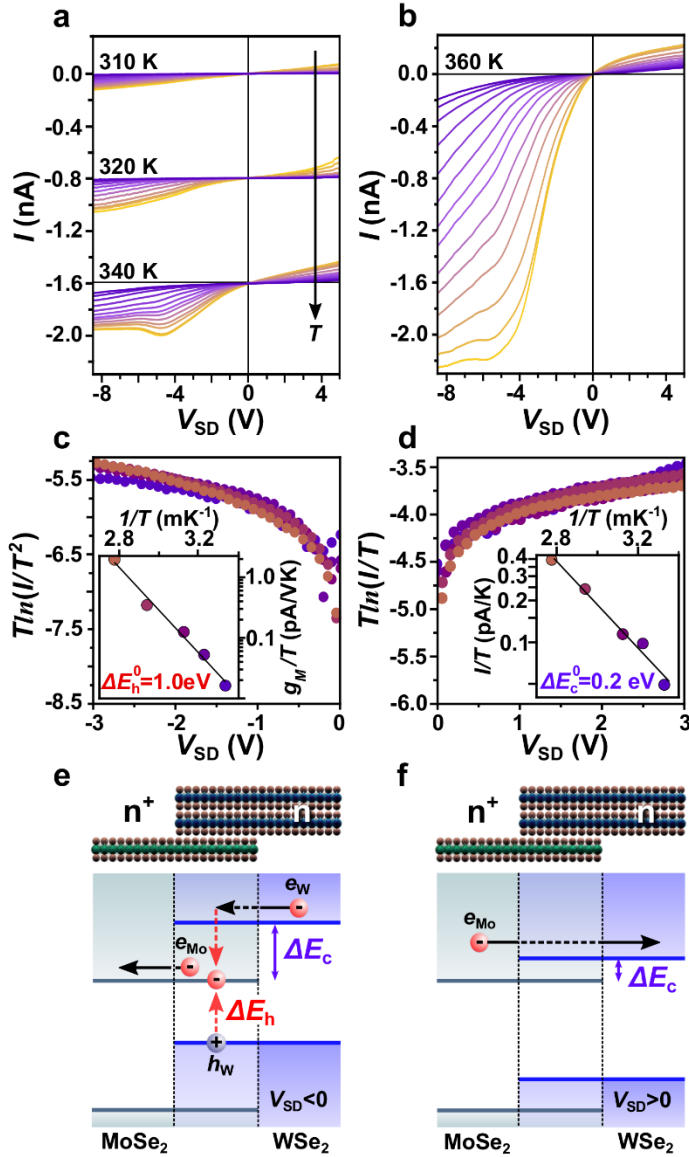


**Figure 4.9:** Temperature dependence of the interlayer  $I$ - $V_{SD}$  characteristics. **(a)**  $I$ - $V_{SD}$  characteristics at  $T = 310 \text{ K}$ ,  $320 \text{ K}$ , and  $340 \text{ K}$  (shifted vertically for clarity).  $V_G$  increases from  $-50 \text{ V}$  to  $10 \text{ V}$  (dark purple to orange). **(b)**  $I$ - $V_{SD}$  characteristics for increasing  $V_G$  at  $T = 360 \text{ K}$ . **(c)**,  $T \ln(I/T^2)$  vs.  $V_{SD}$  in reverse bias at  $T = 300 \text{ K}$ ,  $310 \text{ K}$ ,  $320 \text{ K}$ ,  $340 \text{ K}$ ,  $360 \text{ K}$  ( $V_G = 15 \text{ V}$ ). Inset  $g_M/T$  vs.  $1/T$  ( $V_{SD} = -2.5 \text{ V}$ ,  $V_G = 15 \text{ V}$ ). **(d)**,  $T \ln(I/T)$  vs.  $V_{SD}$  in forward bias at the same temperatures ( $V_G = 15 \text{ V}$ ). **(d)** (inset)  $I/T$  versus  $1/T$  at  $V_{SD} = 2.0 \text{ V}$ ,  $V_G = 15 \text{ V}$ . **(e)** Electronic potential energy diagram for the heterojunction in reverse bias with electron-hole pairs generated at the MoSe<sub>2</sub>/2L-WSe<sub>2</sub> interface. **(f)** Electronic potential energy diagram for  $V_{SD} > 0 \text{ V}$ .

layer. We then evaluate the current in forward and reverse bias by assessing the rates of electron transmission through the *n*-type heterojunction Fig. 4.10, including the rate of interlayer *e-h* pair multiplication.

The 2D heterojunction model requires that we first calculate the density of electronic states  $g(E)$  in each of the TMD atomic layer semiconductors. Our starting model for individual TMD layers is the effective tight-binding two-valley Bloch Hamiltonian (Evan Sosenko, et al.<sup>30</sup>, Di Xiao, et al.<sup>31</sup>, Xiaodong Xu, et al.<sup>32</sup>) which gives the energy spectrum (shown in Figure 4.10):

$$E_{\tau s}^n(k) = \frac{1}{2} \left( \lambda \tau s + n \sqrt{(2atk)^2 + (\Delta - \lambda \tau s)^2} \right). \quad (2)$$

Here,  $\Delta$  is the band gap energy,  $2\lambda$  is the spin splitting in the valence band, the valley index  $\tau = \pm 1$  corresponds to  $\pm K$  points, and the spin index  $s = \pm$  corresponds to the z-component of the spin.  $n = \pm 1$  indexes the conduction and valence band, respectively<sup>18</sup>. We note that the energy spectrum is hyperbolic;  $E(k)$  is approximately parabolic at low energies, but tends towards a constant linear slope at high electron energies.

The density of electronic states in the conduction band ( $n = 1$ ) can be calculated directly from Equation (2) and is given by:

$$g(E) = \frac{I}{\pi a^2 t^2} (E + E_{GAP}) = \frac{E_{GAP}}{\pi a^2 t^2} (1 + E/E_{GAP}) \quad (3)$$

Here,  $E_{GAP}$  is the energy difference between the conduction and valence band in the K and K' valleys of a monolayer TMD, such as MoSe<sub>2</sub>. From Equation (3), the density of states approaches a constant value for electrons near the bottom of the bands, but depends linearly on the electron energy at high energies. Importantly, we note that this

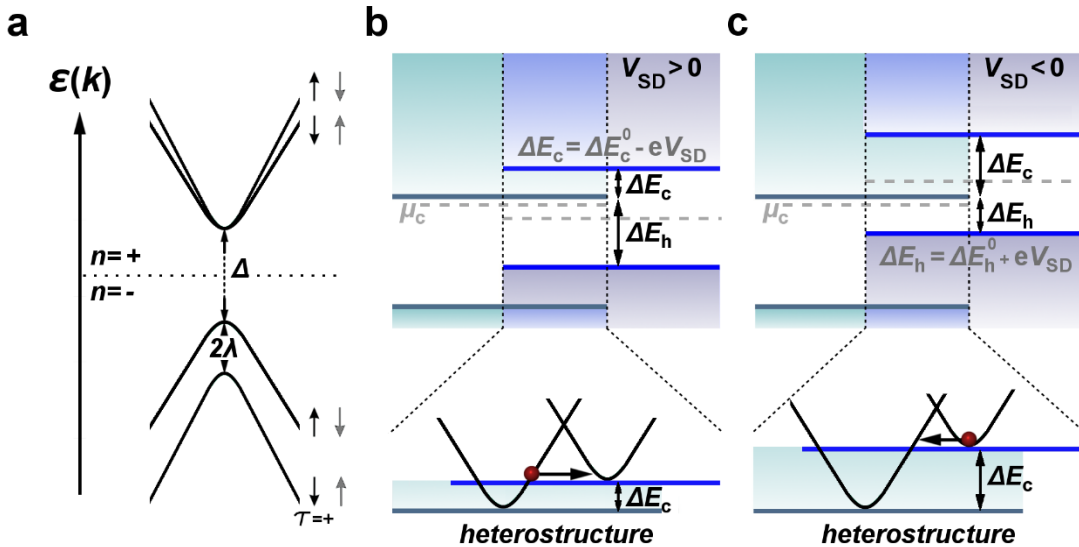


**Figure 4.10:** Schematics of TMD band structure and interlayer electronic transport. **(a)** energy band diagram of a 2D-TMD material with hyperbolic band structure, **(b, c)** electronic band structure of the MoSe<sub>2</sub>/2L-WSe<sub>2</sub> under forward and reverse bias respectively, the area inside the vertical dashed line illustrates the hetero-junction.

result is distinct from the density of states in conventional 2D electron gases, where  $g(E)$  does not depend on energy due to parabolic band structure..

**Forward bias.** Figure 4.10 shows a schematic of the potential energy landscape for electrons in the heterojunction for  $V_{SD} > 0$  V. For  $k_B T \gg \epsilon_F$ , we assume classical Boltzmann distributions to evaluate how many *right*-moving electrons (*i.e.*, electrons that are transferred from MoSe<sub>2</sub> into WSe<sub>2</sub>) transit the interface when a positive  $V_{SD}$  is applied. From the left side, we consider a charge carrier with energy that is just enough to get over the potential barrier at the interface  $\Delta E_c^0$ . From the diagram, this carrier has kinetic energy  $\epsilon - \epsilon_F = \Delta E_c^0 - eV_{SD}$  for  $V_{SD} > 0$  V.

In the forward bias interlayer transport process, conduction occurs through electron states near the bottom of the conduction bands in both materials. In this case, the density of states in both layers is approximately independent of energy. The interlayer current results from counting only right-transiting electrons and is given by:

$$I_+ = \int_{\epsilon}^{\infty} ev\eta_0 g_W(E)g_{Mo}(E)f(E)dE \quad (4)$$

where  $v = v_F$  is the electron Fermi velocity,  $\eta_0$  is the transmission coefficient,  $g_W(E)$  and  $g_{Mo}(E)$  are the density of states in WSe<sub>2</sub> and MoSe<sub>2</sub>, respectively, and  $f(E)$  is the electron distribution in MoSe<sub>2</sub>. Assuming  $eV_{SD}, \Delta E_c^0 \gg k_B T$ , the interlayer current is then

$$I_+ = \Gamma_+(k_B T) \exp(-(\Delta E_c^0 - eV_{SD})/k_B T) \quad (5a)$$

where

$$\Gamma_+ = \frac{ev\eta_0}{(\pi a^2 t^2)^2} (\Delta E_c^0 + \Delta E_h^0)(\Delta E_h^0 + \Delta E_v^0). \quad (5b)$$

Here, we model the system to have constant transmission coefficient  $\eta_0$  for carriers whose total kinetic energy is sufficient to transit the barrier between the TMD layers. As shown in Figure 4.10, the band gap energy in WSe<sub>2</sub> is approximately equal to  $(\Delta E_c^0 + \Delta E_h^0)$  and in MoSe<sub>2</sub> equal to  $(\Delta E_h^0 + \Delta E_v^0)$ .

Equation (S4) indicates that in forward bias the normalized current  $I_+ / T$  should exhibit an exponential decrease with  $1/T$ , from which the activation energy  $\Delta E_c^0$  can be extracted. Equation (5) can also be re-expressed in terms of a temperature-independent quantity that depends only on  $\Delta E_c^0$  and  $V_{SD}$ :

$$(k_B T) \ln(I_+ / \Gamma_+ k_B T) = -\Delta E_c^0 + eV_{SD}. \quad (6)$$

The forward bias  $I-V_{SD}$  characteristics, when rescaled as  $T \ln(I_+/T)$  as in Equation (6), should collapse to a single characteristic. The current  $T \ln(I_+/T)$  vs.  $V_{SD}$  exhibits temperature independent behavior with a linear increase as  $V_{SD}$  increases.

**Reverse bias.** In reverse bias, the temperature and  $V_{SD}$  dependence of the interlayer current serves as a signature of hot electron injection into MoSe<sub>2</sub>, while the thermally activated behavior arises from the energetic threshold for  $e-h$  pair multiplication. The electron-hole pair production process takes place in two steps: **(1)** a low-energy electron in WSe<sub>2</sub> is transferred into a high-energy state in MoSe<sub>2</sub>. **(2)** The high-energy (hot) electron in MoSe<sub>2</sub> decays and produces an interlayer  $e-h$  pair. As the reverse bias voltage is increased, electron-hole pairs generated by high-energy electrons are separated in the electric field and increase the device current. We first define the

energy barrier for additional electron generation due to *e-h* pair multiplication, and then evaluate the interlayer current  $I$  that results from *e-h* pair multiplication when  $V_{SD} < 0$  V.

For interlayer transport from WSe<sub>2</sub> (right) to MoSe<sub>2</sub> (left), it is important to note that electrons need not overcome a potential energy barrier, but instead may gain the potential energy  $\Delta E_c^0$ . In conventional devices, this leads to reverse bias saturation current with weak dependence on  $V_{SD}$  or temperature<sup>22</sup>. However, interlayer *e-h* pair production requires a hot electron with a minimum excess kinetic energy, and thus depends strongly on both  $V_{SD}$  and temperature. From the schematic in Figure 4.10, the minimum kinetic energy required for an electron to generate an interlayer *e-h* pair is given by:

$$K_e^* = \Delta E_h^0 - \Delta E_c^0 + 2eV_{SD}, \quad (7)$$

where  $\Delta E_h^0$  is the interlayer *e-h* pair excitation energy at  $V_{SD} = 0$  V. We note that when  $V_{SD} < 0$  V, the potential energy that can be gained by an electron is increased  $\Delta E_c = \Delta E_c^0 + e|V_{SD}|$ , while the interlayer excitation energy is simultaneously decreased  $\Delta E_h = \Delta E_h^0 - e|V_{SD}|$ , resulting in Equation (S6).

In reverse bias, the energy difference between the conduction bands of the two materials is large. Due to the electric field at the interface, low-energy electrons in WSe<sub>2</sub> - with approximately constant density of states - are transferred into hot electrons in MoSe<sub>2</sub> at high kinetic energy with density of states proportional to  $E$  (Eq. (3)). The current due to interlayer *e-h* pair multiplication  $I_M$  is then

$$I_M \approx \int_{\varepsilon}^{\infty} e v \gamma_0 \left( \frac{E_{GAP}^W}{\pi a^2 t^2} \right) \left( \frac{E}{\pi a^2 t^2} \right) \exp(-(E-E_F)/k_B T) dE; \quad (8a)$$

$$= \frac{e v \gamma_0 (\Delta E_c^0 + \Delta E_h^0)}{(\pi a^2 t^2)^2} \int_{\varepsilon}^{\infty} E \exp(-(E-E_F)/k_B T) dE, \quad (8b)$$

where we assume that the product of the transmission coefficient and impact excitation rate  $\gamma_0$  is approximately constant above the kinetic energy threshold. Computing the integral over the entire energy range and noting  $k_B T \gg \varepsilon_F$ , gives

$$I_M = \Gamma_M (k_B T)^2 \left( \exp(-K_e^*/k_B T) - 1 \right); \quad (9a)$$

$$\Gamma_M = \frac{e v \gamma_0 (\Delta E_c^0 + \Delta E_h^0)}{(\pi a^2 t^2)^2}. \quad (9b)$$

In contrast to the forward bias current, there is an additional power of  $k_B T$  in the reverse bias current, which arises from the density of available electron states in MoSe<sub>2</sub>.

Equation (9) indicates that in the  $V_{SD}$  and temperature regime in which  $e$ - $h$  pair multiplication is the dominant source of current, the reverse bias current can be re-expressed in terms of a temperature-independent quantity that depends on  $\Delta E_h^0$ . The reverse bias  $I$ - $V_{SD}$  characteristics, when rescaled as  $T \ln(I_M/T^2)$  as in Equation (9), should collapse to a single line. In this case, the voltage dependence of  $T \ln(I_M/T^2)$  exhibits universal behavior, with a linear increase with  $V_{SD}$ .

While Equation (9) gives the temperature scaling of the current due to  $e$ - $h$  pair multiplication, an additional straightforward analysis is required to obtain  $\Delta E_h^0$ . First, note that Equation (9) contains a  $V_{SD}$ -independent term and a  $V_{SD}$ -dependent term. In

order to isolate the activation energy  $\Delta E_h^0$ , we simply take the derivative  $dI_M/dV_{SD}$  of Equation (9), giving

$$\frac{|dI_M/dV_{SD}|}{(2\Gamma k_B T)} = \exp(-K_e^*/k_B T) . \quad (10)$$

Equation (10) indicates that the quantity  $(dI_M/dV_{SD})/T$  vs.  $1/T$  should exhibit an exponential decrease, from which the activation energy  $K_e^*$  can be extracted.

Ignoring recombination of interlayer  $e$ - $h$  pairs, the low bias ( $-3 \text{ V} < V_{SD} < -0.5 \text{ V}$ ) current due to  $e$ - $h$  pair multiplication  $I_M$  takes the form:

$$I_M \propto \Gamma_M (k_B T)^2 \exp(-K_e^*/k_B T), \quad (11)$$

where  $k_B$  is the Boltzmann constant, and  $\Gamma_M$  contains details about the impact excitation probability and interlayer transit rate. The minimum kinetic energy required for a hot electron to excite an interlayer  $e$ - $h$  pair in reverse bias is given by

$$K_e^* = \Delta E_h^0 - \Delta E_c^0 + 2e(\alpha V_{SD}), \quad (12)$$

where  $\Delta E_h^0 > \Delta E_c^0$ . When a negative  $V_{SD}$  is applied, the potential energy gained by the electron increases while the interlayer excitation energy decreases  $\Delta E_h = \Delta E_h^0 - e(\alpha |V_{SD}|)$  (Fig. 3e). For increasing reverse bias, the rapidly increasing current due to  $e$ - $h$  multiplication  $I_M$  is overcome by the evolution of the recombination rate with  $V_{SD}$ : recombination increases with the reduction of  $\Delta E_h$ , and also increases with  $V_G$  since there are more electrons available to combine with the holes generated through impact excitation. This competition results in NDC and a corresponding peak in the dark  $I$ - $V_{SD}$  characteristics.

This model makes a number of predictions that can be compared to experiment. First, as the reverse bias voltage is increased, hot electrons with kinetic energy that exceeds  $K_e^*$  may generate interlayer  $e$ - $h$  pairs (Fig. 4.9e), which are subsequently separated into the constituent electron and hole. Impact excitation generates additional conduction electrons at the interface. As a consequence, the onset gate voltage  $V_{ON}$  is lowered for negative  $V_{SD}$ , while it is not affected for  $V_{SD} > 0$  V.

#### 4.9 Confirmation of gate and temperature dependence

We examine the gate voltage-dependent interlayer current to test this conjecture. Figure 4.11a shows a color map of  $d\log I/dV_G$  vs.  $V_G$  and  $V_{SD}$  taken at  $T = 340$  K. At  $V_{SD} > 0$  V, we observed a vertical peak feature in the  $d\log I/dV_G$  map that occurs near  $V_G = -36$  V. We label this gate voltage, which remains constant in forward bias, as  $V_{ON}^+$  in Figure 4.11a. Such standard behavior does not include the effects of  $e$ - $h$  pair multiplication. In contrast, horizontal line traces of  $d\log I/dV_G$  in reverse bias (Fig. 4.11a bottom) show that  $V_{ON}$  decreases approximately linearly with increasing negative  $V_{SD}$ . Additional electrons generated in the MoSe<sub>2</sub> conduction band increase the electron density in the unipolar interlayer channel, thus lowering the gate voltage required for the onset to conduction.

Our model also predicts that by reducing temperature,  $e$ - $h$  multiplication is suppressed. Figure 4.11b shows the temperature-dependent  $d\log I/dV_G$  maps in reverse bias. At each temperature, we extract the maximum values of  $d\log I/dV_G$  as a function of  $V_G$  and  $V_{SD}$  (Fig. 4.11c). At  $T = 300$  K, the onset gate voltage shifts only slightly below

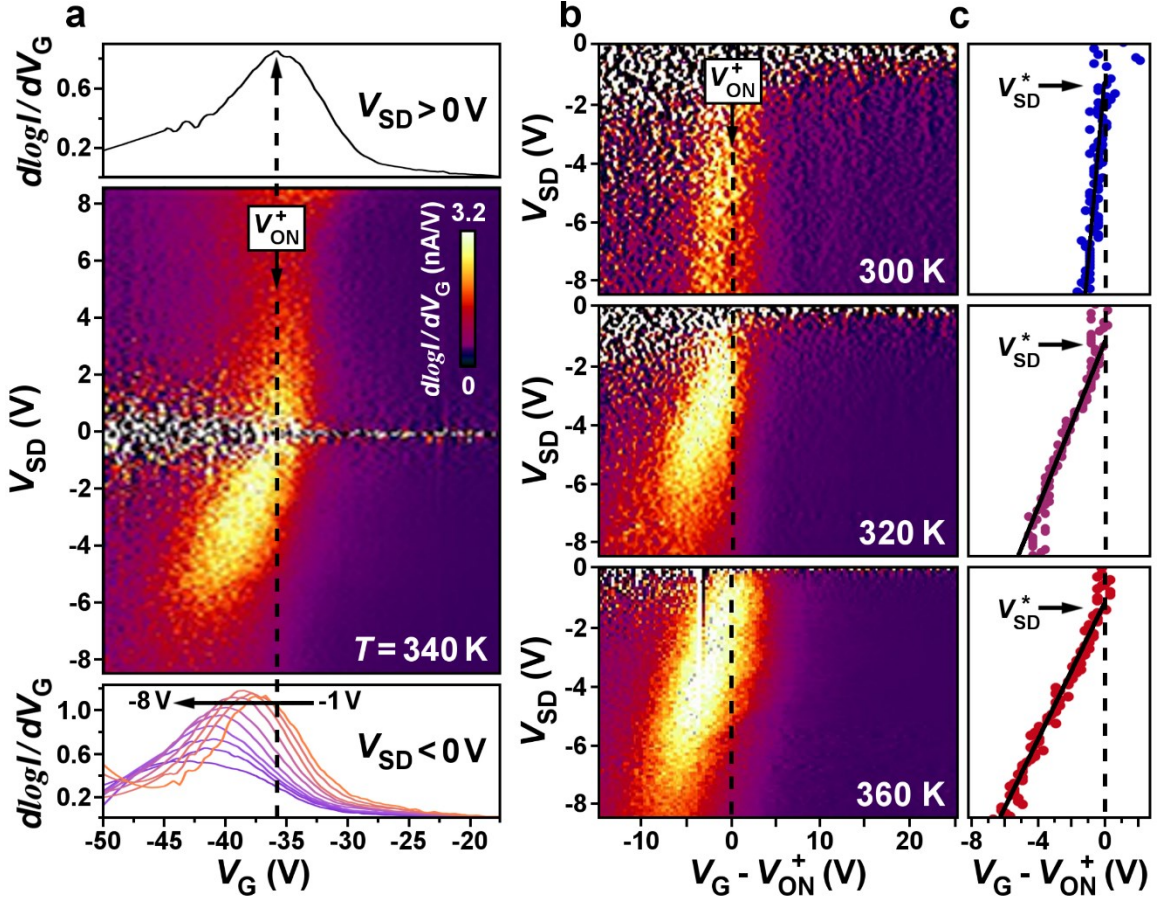


**Figure 4.11:** Gate voltage, source-drain voltage, and temperature dependence of  $d\log I/dV_G$  in the 2D semiconductor heterostructure device. **(a)** Color map of  $d\log I/dV_G$  vs.  $V_G$  and  $V_{SD}$  ( $T = 340$  K). Top,  $d\log I/dV_G$  vs.  $V_G$  characteristic at  $V_{SD} = 2.0$  V. Vertical dashed line labels the maximum value of  $d\log I/dV_G$  in forward bias, denoted  $V_{ON}^+$ . Bottom,  $d\log I/dV_G$  vs.  $V_G$  characteristics for increasing negative  $V_{SD}$  from  $V_{SD} = -1.0$  V (yellow line) to  $V_{SD} = -8.0$  V (purple line). **(b)**  $d\log I/dV_G$  vs.  $V_G$  and  $V_{SD}$  for negative  $V_{SD}$ . The gate voltage axis is shifted by  $V_{ON}^+$  (vertical dashed line) extracted at each temperature. **(c)** Maximum values of  $d\log I/dV_G$  extracted at each temperature.  $V_{SD}^*$  labels the intercept of the linear fits of the maxima and  $V_{ON}^+$ .

$V_{ON}^+$  (vertical dashed lines Fig. 4.11c) as the reverse bias  $V_{SD}$  is increased, indicating that no additional charge is generated at the interface. Above  $T = 320$  K, as the source-drain voltage increases above the threshold  $V_{SD}^* = -1.2$  V, the onset gate voltage  $V_{ON}$  decreases approximately linearly with increasing negative  $V_{SD}$ . The appearance of this feature, in which  $V_{ON}$  decreases linearly with negative  $V_{SD}$ , correlates directly with the temperature-dependent increase of the interlayer current (Fig. 4.9).

The very low threshold voltage  $V_{SD}^*$  shown in Figure 4.11b highlights an important aspect of hot carrier-enhanced  $e$ - $h$  pair generation. The interlayer transport process  $e_W \rightarrow e_{Mo}$  transfers a low-energy electron in the WSe<sub>2</sub> conduction band into a hot electron above the conduction band edge in MoSe<sub>2</sub> (Fig. 4.10). Impact excitation generates additional charge density only if the excess kinetic energy exceeds  $K_e^*$ .  $V_{ON}$  is therefore reduced below  $V_{ON}^+$  once the source-drain voltage exceeds a critical energy  $eV_{SD}^* > 1.2$  eV (labeled in Fig. 4.11c). The threshold voltage  $V_{SD}^*$  for *interlayer*  $e$ - $h$  pair generation is lower than the energy-conservation limit for excitation of *intralayer* bound  $e$ - $h$  pairs in either MoSe<sub>2</sub> ( $\Delta E_{Mo}/e = 1.57$  V) or bilayer WSe<sub>2</sub> ( $\Delta E_W/e = 1.46$  V).

#### 4.10 Photoresponse enhancement using carrier multiplication

Hot carrier-enhanced interlayer impact excitation can be utilized to significantly increase the photoresponse in TMD heterojunction photocells. Figure 4.12a shows interlayer photocurrent characteristics at low optical power (17  $\mu$ W) and  $\lambda = 900$  nm. When  $V_G < V_{ON}$ , the dark current (black line trace Fig. 4.12a) is strongly suppressed since

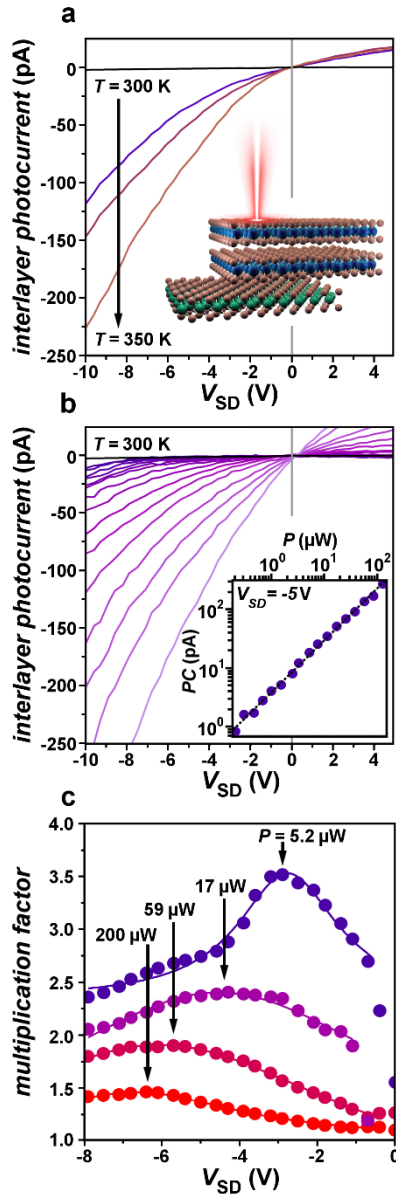


**Figure 4.12:** Interlayer photocurrent characteristics and multiplication enhancement in the 2D heterojunction photocell. **(a)** Interlayer photocurrent vs.  $V_{SD}$  at  $T = 300$ ,  $340$ , and  $350$  K with  $V_G < V_{ON}$ ; black line trace is the dark  $I-V_{SD}$  characteristic. Optical illumination is focused at the heterostructure with a laser at  $\lambda = 900$  nm,  $P = 17 \mu\text{W}$ . (see inset schematic) **(b)** Interlayer photocurrent vs.  $V_{SD}$  for increasing optical power at  $T = 300$  K. Inset, photocurrent vs. power at  $V_{SD} = -5$  V. **(c)** Multiplication factor determined from the ratio of the responsivities  $R_{350} / R_{300}$  at various optical power levels (labeled). Solid lines are Lorentzian fits used to determine the peak multiplication value.

the  $n^+ - n$  heterojunction formed at the interface is depleted of conduction electrons. Under local optical illumination of the heterostructure, the reverse bias photocurrent increases rapidly with increasing temperature. In contrast, the photocurrent at  $V_{SD} > 0$  shows negligible temperature dependence. Such reverse bias photocurrent enhancement is fully consistent with Equation (1): an optically excited  $e_W$  electron in the conduction band of WSe<sub>2</sub> undergoes efficient multiplication into an  $e_{Mo}$  electron and additional  $e-h$  pairs.

Interlayer impact excitation results in responsivity enhancement that exceeds 350%. To quantify the multiplication factor, we measured the power dependence at each temperature and examined the ratio of the responsivity  $R$  at elevated temperatures to that at  $T = 300$  K (Figure 4.12b). Since impact excitation is suppressed at low temperatures, the ratio  $R_{350} / R_{300}$  gives a lower bound of the multiplication enhancement. Figure 4.12c shows  $R_{350} / R_{300}$  as a function of  $V_{SD}$  for various optical powers. At low power (blue data), the enhancement factor exceeds 3.5 and shows a clear peak near  $V_{SD} = -2.8$  V, which corresponds very closely to the peak conductance  $g_M$  due to  $e-h$  multiplication in the absence of light (Fig. 4.8d). At high optical power (red data) the enhancement is reduced, likely resulting from increased electron-hole pair annihilation or thermal effects.

For the assessment of the multiplication factor, we were very careful to photoexcite only within the WSe<sub>2</sub> absorption edge while avoiding optical absorption in the (overlapping) low energy tail of the MoSe<sub>2</sub> absorption peak. Absorption in MoSe<sub>2</sub> may result in complicated interlayer transfer processes and additional state filling that may skew the determination of the multiplication factor. From Figures 4.5 and 4.6, we show that the heterostructure exhibits somewhat weak, but easily measured

photoluminescence and photocurrent response at photon energy 1.38 eV (corresponding to  $\lambda = 900$  nm). While this energy is slightly below, but still within the absorption peak of the  $\text{ew}$  transition, we chose this wavelength to avoid as much as possible any absorption in the low energy tail of the MoSe<sub>2</sub> absorption edge, which begins to become non-negligible as the photon energy increases above 1.4 eV (Figure 4.6).

Figure 4.13 shows photocurrent I-VSD characteristics taken at increasing photon energies and  $T = 300\text{K}$  (in the regime of inefficient impact excitation) with the laser power fixed at  $P = 17 \mu\text{W}$ . While the overall photoresponse at 1.38 eV is comparatively weak, the photocurrent results primarily from absorption in WSe<sub>2</sub> rather than combined absorption within the absorption bands of WSe<sub>2</sub> and MoSe<sub>2</sub>. As the absorption of MoSe<sub>2</sub> becomes important at higher energies, the overall photoresponse increases proportionally. At higher photon energies, a careful assessment of the multiplication factor is less dependable, as it must include the additional effects of current flow and interlayer transfer caused by absorption in both layers. Future work will examine the detailed photon energy dependence of impact excitation process by probing the intricate dependence of photocurrent on photon energy, voltage, and temperature.

#### 4.11 Conclusion

Since the basic process limiting the performance of optoelectronic and photovoltaic devices is the generation of phonons by hot charge carriers, hot-carrier enhanced multiplication could theoretically improve device efficiency beyond standard thermodynamic limits<sup>33</sup>. Normally, optical phonon emission is very efficient at relaxing

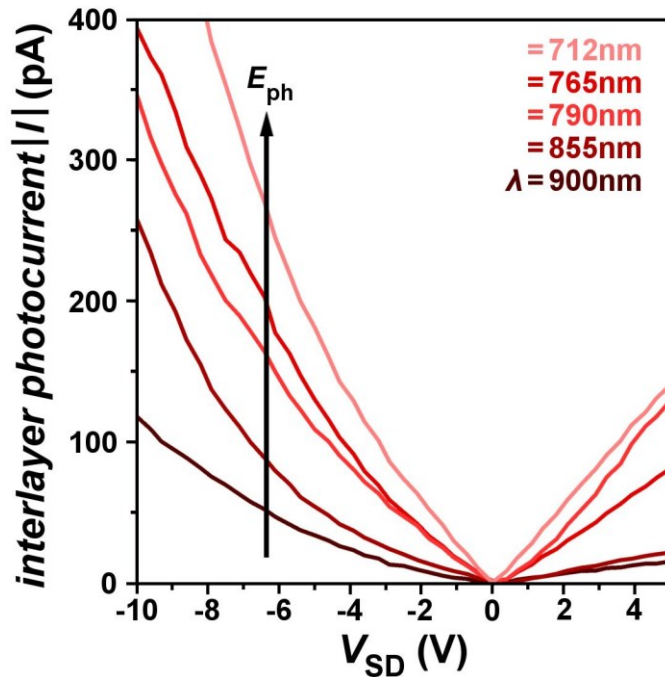


**Figure 4.13:** Wavelength dependence of the interlayer photocurrent-voltage characteristics at  $T = 300$  K. Photocurrent (absolute value) vs.  $V_{SD}$  measured as a function of decreasing wavelength (increasing photon energy) at fixed power = 17  $\mu\text{W}$ . Photon energies are  $E_{ph} = 1.38$  eV, 1.45 eV, 1.57 eV, 1.62 eV, and 1.74 eV from bottom to top. For comparison, the black line trace is the same data shown in main text Figure 5a ( $T = 300$  K,  $E_{\text{photon}} = 1.38$  eV).

hot electrons, including those in individual monolayer TMDs<sup>34</sup>. In contrast, the  $e_W \rightarrow e_{Mo}$  process produces hot electrons that convert excess kinetic energy  $\Delta E_h^0$  into additional *e-h* pairs. From Equation (2),  $I_M$  depends sensitively on  $\Delta E_h^0$  and contains a temperature-dependent pre-factor of  $(k_B T)^2$ . This factor arises from the increased density of states available to hot  $e_{Mo}$  electrons during impact excitation (Fig. 4.10) and does not arise in forward bias (see Supplementary S4). The differential conductance in reverse bias is then given by  $g = dI_M/dV_{SD} \propto 2eI_M / k_B T$  (Supplementary equation S9), suggesting a linear relationship between  $\ln(g/T)$  and  $1/T$  with a slope of  $-K_e^*$ . Figure 3c inset shows the data  $\ln(g_M/T)$  vs.  $1/T$  over a range of temperatures. From the slope of the linear fit ( $-K_e^*$ ) and Eq. (3), we obtain the interlayer *e-h* pair excitation energy  $\Delta E_h^0 = K_e^* + \Delta E_c^0 = 1.0$  eV, which agrees well with  $\Delta E_h^0(\text{theory}) = 0.94$  eV (Fig. S4).

Hot electron impact excitation results in a highly efficient energy relaxation process that differs strongly from conventional impact ionization. In the MoSe<sub>2</sub>/WSe<sub>2</sub> heterostructure photocells, no avalanche breakdown behavior is observed, giving additional insight into the origin of the NDC in Figure 2. While NDC is often attributed to tunneling behavior, here the NDC is due to the competition between multiplication and *e-h* pair recombination. Recent measurements of 2D heterostructures have suggested that Shockley-Read-Hall (SRH) and Langevin processes dominate the recombination of interlayer *e-h* pairs<sup>18,19,22</sup>, which may be strongly bound at low voltage and temperature. In the devices demonstrated here, the multiplication-recombination competition results in a peak in the dark  $I-V_{SD}$  characteristics (Fig. 4.8c) and a corresponding reduction of the

multiplication enhancement factor at high negative  $V_{SD}$  (Fig. 4.8b). While in standard semiconductors, competing energy relaxation mechanisms restrict carrier multiplication to extremely large biases<sup>24</sup>, interlayer impact excitation dominates at very low applied  $V_{SD}$  bias. Such remarkable behavior could lead to novel photodetectors<sup>22,27</sup>, electroluminescent emitters<sup>35</sup>, and excitonic integrated circuits<sup>36</sup>, which exploit the quantum degrees of freedom<sup>19,37</sup> and layer-indirect nature of  $e-h$  pairs in 2D heterostructures.

## REFERENCES

1. Dirac, P. A. M. *The Principles of Quantum Mechanics*. (Oxford University Press, Amen House, London, 1930).
2. Schaller, R. D. & Klimov, V. I. “High efficiency carrier multiplication in PbSe nanocrystals: implications for solar energy conversion.” *Phys. Rev. Lett.* **92**, 1866011-1866014 (2004).
3. Ellingson, R. J. et al. “Highly efficient multiple exciton generation in colloidal PbSe and PbS quantum dots.” *Nano Lett.* **5**, 865-871 (2005).
4. Semonin, O. E. et al. “Peak external photocurrent quantum efficiency exceeding 100% via MEG in a quantum dot solar cell.” *Science* **334**, 1530-1533 (2011).
5. Gachet, D., Avidan, A., Pinkas, I. & Oron, D. “An upper bound to carrier multiplication efficiency in type II colloidal quantum dots.” *Nano Lett.* **10**, 164-170 (2010).
6. Cirloganu, M. C. et al. “Enhanced carrier multiplication in engineered quasi-type-II quantum dots.” *Nat. Commun.* **5**, 1-8 (2014).
7. Ueda, A., Matsuda, K., Tayagaki, T. & Kanemitsu, Y. “Carrier multiplication in carbon nanotubes studied by femtosecond pump-probe spectroscopy.” *Appl. Phys. Lett.* **92**, 2331051-2331053 (2008).
8. Gabor, N. M., Bosnick, Z. K., Park, J. & McEuen, P. L. “Extremely efficient multiple electron-hole pair generation in carbon nanotube photodiodes.” *Science* **325**, 1367-1371 (2009).
9. Wang, S., Khafizov, M., Tu, X., Zheng, M. & Krauss, T. D. “Multiple exciton generation in single-walled carbon nanotubes.” *Nano Lett.* **10**, 2381-2386 (2010).
10. Plotzing, T. et al. “Experimental verification of carrier multiplication in graphene.” *Nano Lett.* **14**, 5371-5375 (2014).
11. Brida, D. et al. “Ultrafast collinear scattering and carrier multiplication in graphene.” *Nat. Commun.* **4**, 1-9 (2013).
12. Wendler, F., Knorr, A. & Malic, E. “Carrier multiplication in graphene under Landau quantization.” *Nat. Commun.* **5**, 1-6 (2013).

13. Wu, S. et al. “Multiple hot-carrier collection in photo-excited graphene Moire superlattices.” *Sci. Adv.* **2**, 1-6 (2016).
14. Wu, F., Qu, F. & MacDonald, A. H. “Exciton band structure of monolayer MoS<sub>2</sub>.” *Phys. Rev. B* **91**, 0753101-0753108 (2015).
15. Chernikov, A. et al. “Exciton Binding Energy and Nonhydrogenic Rydberg Series in Monolayer WS<sub>2</sub>.” *Phys. Rev. Lett.* **113**, 0768021-0768025 (2014).
16. Keldysh, L. V. “Coulomb interaction in thin semiconductor and semimetal films.” *JETP Lett.* **29**, 658-660 (1979).
17. Hong, X. et al. “Ultrafast charge transfer in atomically thin MoS<sub>2</sub>/WS<sub>2</sub> heterostructures.” *Nat. Nanotechnol.* **9**, 682-686 (2014).
18. Rivera, P. et al. “Valley-polarized exciton dynamics in a 2D semiconductor heterostructure.” *Nat. Commun.* **6**, 1-6 (2015).
19. Rivera, P. et al. “Observation of long-lived interlayer excitons in monolayer MoSe<sub>2</sub>-WSe<sub>2</sub> heterostructures.” *Science* **351**, 688-691 (2016).
20. Rigosi, A. F., Hill, H. M., Li, Y., Chernikov, A. & Heinz, T. F. “Probing Interlayer Interactions in Transition Metal Dichalcogenide Heterostructures by Optical Spectroscopy: MoS<sub>2</sub>/WS<sub>2</sub> and MoSe<sub>2</sub>/WSe<sub>2</sub>.” *Nano Lett.* **15**, 5033-5038 (2015).
21. Calman, E. V. et al. “Control of excitons in multi-layer van der Waals heterostructures.” *Appl. Phys. Lett.* **108**, 1019011-1019014 (2016).
22. Lee, C. L. et al. “Atomically thin p-n junctions with van der Waals heterointerfaces.” *Nat. Nanotechnol.* **9**, 676-681 (2014).
23. Castellanos-Gomez, A. et al. “Deterministic transfer of two-dimensional materials by all-dry viscoelastic stamping.” *2D Mater. Lett.* **1**, 1-8 (2014).
24. Wilson, N. R. et al. “Band parameters and hybridization in 2D semiconductor heterostructures from photoemission spectroscopy.” *arXiv* **1** 1601.05865 (2016).
25. Tonndorf, P. et al. “Photoluminescence emission and Raman response of monolayer MoS<sub>2</sub>, MoSe<sub>2</sub>, and WSe<sub>2</sub>.” *Opt. Express* **21**, 4908-4916 (2013).

26. Rivera, P. et al. “Valley-polarized exciton dynamics in a 2D semiconductor heterostructure.” *Nat. Commun.* **6**, 1-6 (2015).
27. Ceballos, F., Bellus, M. Z., Chiu, H. & Zhao, H. “Ultrafast charge separation and indirect exciton formation in a MoS<sub>2</sub>–MoSe<sub>2</sub> van der Waals heterostructure.” *ACS Nano* **8**, 12717-12724 (2014).
28. Furchi, M. M., Pospischil, A. A., Libisch, F., Burgdörfer, J. & Mueller, T. “Photovoltaic Effect in an Electrically Tunable van der Waals Heterojunction.” *Nano Lett.* **14**, 4785-4791 (2014).
29. Nourbakhsh, A., Zubair, A., Dresselhaus, M., & Palacios, T. “Transport properties of a MoS<sub>2</sub>/WSe<sub>2</sub> hterojunction transistor and its potential for application.” *Nano Letters* **16**, 1359-1366 (2016).
30. Sosenko, E., Zhang, J., Aji, V. “Superconductivity in transition metal dichalcogenides.” *arXiv* **2**, 1512.01261 (2016).
31. Xiao, D., Liu, G., Feng, W., Xu, X. & Yao, W. “Coupled spin and valley physics in monolayers of MoS<sub>2</sub> and other group-VI dichalcogenides.” *Phys. Rev. Lett.* **108**, 1968021-1968025 (2012).
32. Xu, X., Yao, W., Xiao, D. & Heinz, T. F. “Spin and pseudospins in layered transition metal dichalcogenides.” *Nat. Phys.* **10**, 343-350 (2014).
33. Sze, M. & NG, K. K. *Physics of Semiconductor Devices*. (Wiley-Interscience publications, United States, 1963).
34. Movva, H. C. P. et al. “High-mobility holes in dual-gated WSe<sub>2</sub> field-effect transistors.” *ACS Nano* **9**, 10402-10410 (2015).
35. Withers, F. et al. “Light-emitting diodes by band-structure engineering in van der Waals heterostructures.” *Nat. Mater.* **14**, 301-306 (2015).
36. High, A. A., Novitskaya, E. E., Butov, L. V., Hanson, M., Gossard, A. C. “Control of exciton fluxes in an excitonic integrated circuit.” *Science* **321**, 229-231 (2008).
37. Jones, A. M. et al. “Spin–layer locking effects in optical orientation of exciton spin in bilayer WSe<sub>2</sub>.” *Nat. Phys.* **10**, 130-134 (2014).

## Chapter 5

### Thermospintronic Imaging of Electrostatic Flux

#### 5.1 Introduction

A single moving electron will generate a current in nearby electrodes, even if it never strikes an electrode itself. This is because the electric field of the electron propagates with it and induces current in electrodes. First formalized in the Shockley-Ramo theorem<sup>1-3</sup>, this result states that the current induced by the moving electron will be  $I = e\vec{E} \cdot \vec{v}$ , where  $e$  is the electron charge,  $v$  is the electron velocity, and  $E$  is the electric field that would exist at the electron's location if the electron were removed and one electrode was placed at some potential while all others were grounded. This result has been extended to optoelectronic systems<sup>4,5</sup>, in which the current measured between contacts will be

$$I = A \int \mathbf{j}_{ph}(\mathbf{r}) \cdot \nabla \psi(\mathbf{r}) d^2r$$

where  $\mathbf{j}_{ph}(\mathbf{r})$  is a local photocurrent,  $\psi$  is a weighting field obtained by solving the Laplace equation  $-\sigma \nabla^2 \psi = 0$  for the device geometry, and  $A$  is a device-dependent scaling factor. The consequence of this relation is that in an optoelectronic device, maximum measured current will occur when  $\mathbf{j}$  and  $\nabla \psi$  are aligned.

One method for generating a highly directional photocurrent is the spin Seebeck effect (SSE)<sup>6</sup>, in which a temperature gradient applied to a magnetized material generates a voltage perpendicular to both, or  $V = L \nabla T \times \mathbf{M}$ , where  $L$  is the material-specific spin Seebeck coefficient (Fig 5.1). By measuring the current generated in a SSE device as we

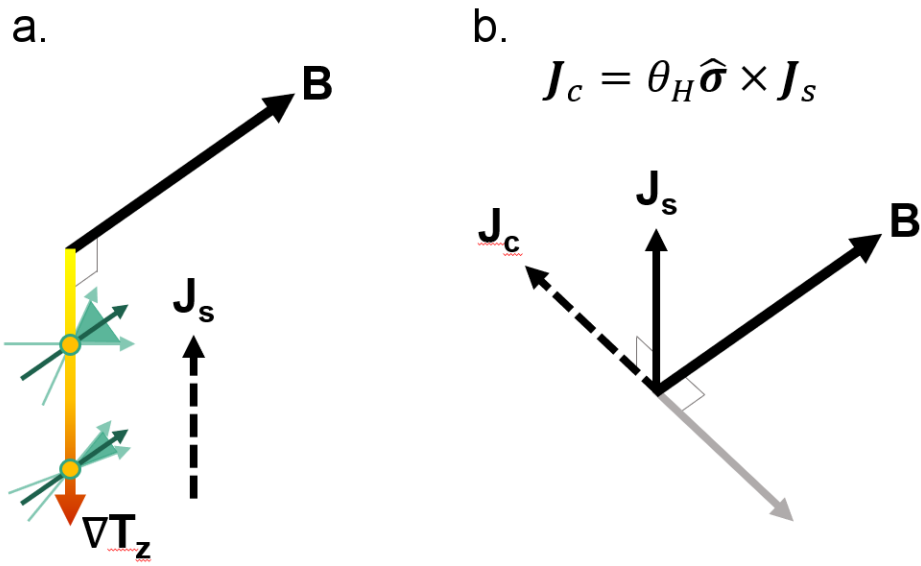


**Figure 5.1:** Thermospintronic generation mechanisms. **(a)** Spin-Seebeck effect: A temperature gradient in a magnetized material creates a spin current as hotter spins oscillate more than cold spins. **(b)** Inverse Spin-Hall effect: In the presence of a spin-orbit interaction, electrons are scattered proportional to  $\hat{\sigma} \times J_s$ , converting spin current to real charge current  $J_c$ .<sup>6</sup>

scan a laser beam and vary magnetic field direction, we can identify field angles that generate maximum photocurrent and directly map the electrostatic flux lines.

## 5.2 Spin-Seebeck effect in a Pt-YIG device

To test this hypothesis, we fabricated a 5 nm-thick platinum Hall bar on top of an unpatterned 80 nm YIG layer, all on top of a GGG (110) substrate (Fig 5.2.a). We contacted the Hall bar pads with 25  $\mu\text{m}$ -diameter aluminum wire bonds connected to a PCB and measured the differential voltage between wire bonds using standard lock-in technique at 4 Hz. To generate a photovoltage in the device, we scan a laser beam across the surface while applying a 0.52T magnetic field (Fig 5.2.b). Absorption in the platinum generates a temperature gradient centered on the laser spot, which, combined with the magnetic field, gives rise to a spin-Seebeck voltage. The beam had a wavelength of 830 nm, with a pulselwidth of 180 fs, a spot size FWHM of 23  $\mu\text{m}$  and power of 30mW at the sample surface. The spot size was determined using knife-edge technique and we characterized the pulselwidth by measuring the autocorrelation.

Figure 5.3a shows the reflection image of the sample with dark color representing the platinum Hall bar and light color representing YIG. The beam spot is several times smaller than the width of the Hall bar and of comparable width to the narrow channels connecting to the contact pads. Photovoltage maps over the exact same field of view are shown in Figs. 5.3.b and 5.3c with the magnetic field direction flipped between measurements. We observe photovoltage everywhere in the main body of the Hall bar with the largest signal occurring in the channels nearest to the measurement leads. There is a left-to-right asymmetry in the photovoltage which flips with the magnetic field, as

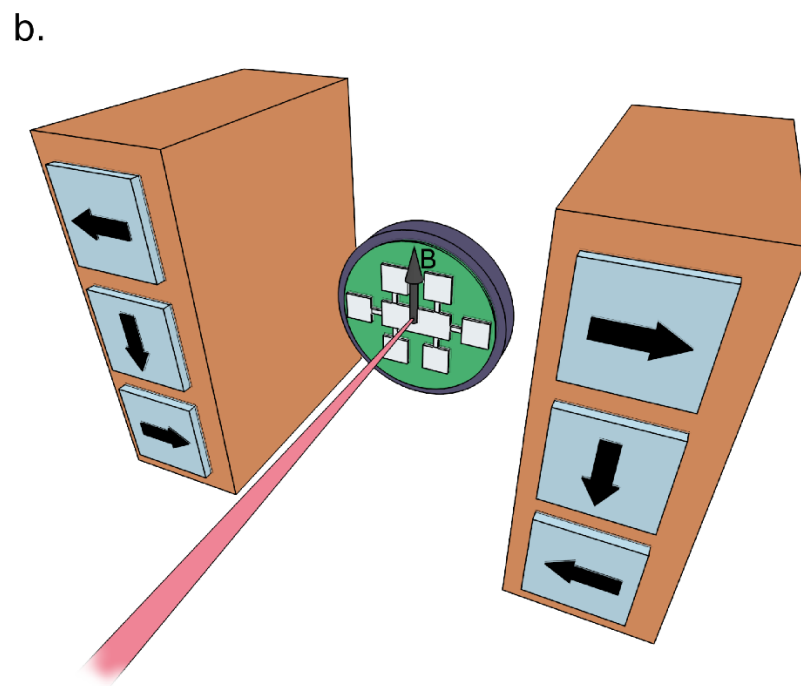
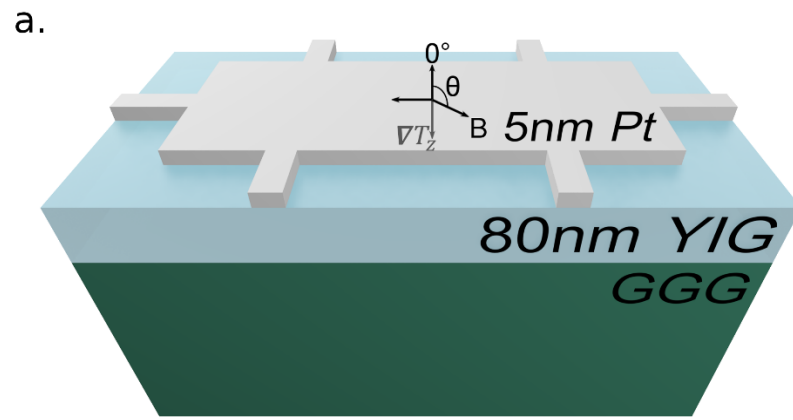


**Figure 5.2:** Experimental spin-Seebeck setup. **(a)** Pt-YIG device diagram. B-field angle is defined with respect to line perpendicular to long dimension of Hall bar. **(b)** Magneto-optic measurement architecture including Halbach array.

does the photovoltage signal. This asymmetry is largely due to the conventional Seebeck effect (see section 5.5), which is subtracted from the raw data to leave only the spin-Seebeck contribution. The magnitude of the signal seen here is comparable to that reported by other groups<sup>7-9</sup> under similar conditions.

### 5.3 Angular dependence of spin-Seebeck photovoltage

Removing the conventional, magnetic field-independent Seebeck effect reveals the angle-dependent spin Seebeck photovoltage shown in Figure 5.4a. We see that when the magnetic field is pointed perpendicular to the contacts, the photovoltage is large and uniform in the body of the Hall bar, in agreement with Goennenwein<sup>7</sup>. When the field is parallel to the contacts, the photovoltage in the center of the device drops to zero as expected, but nodes of signal remain in the corners and perpendicular channels. To better understand the nature of these data, we fit the photovoltage as a function of field angle with the sine function

$$V_{LSSE} = V_0 + A \sin\left(2\pi \frac{\varphi - \varphi_c}{\omega}\right)$$

at every point in space (Fig 5.4c), where  $A$  is the amplitude,  $\varphi_c$  is phase shift,  $V_0$  is an offset voltage, and  $\omega$  is angular frequency. This again confirms the conventional behavior of the SSE in the center of the device but also illustrates the phase shift and decreased amplitude found when the laser beam heats near the corners and perpendicular channels of the device.

We next spatially map the fitting parameters amplitude and phase. The amplitude (Fig 5.4d) shows that the peak value of the SSE remains constant throughout the body of the Hall bar. The phase map (Fig 5.4e) is far more intriguing, showing that the phase

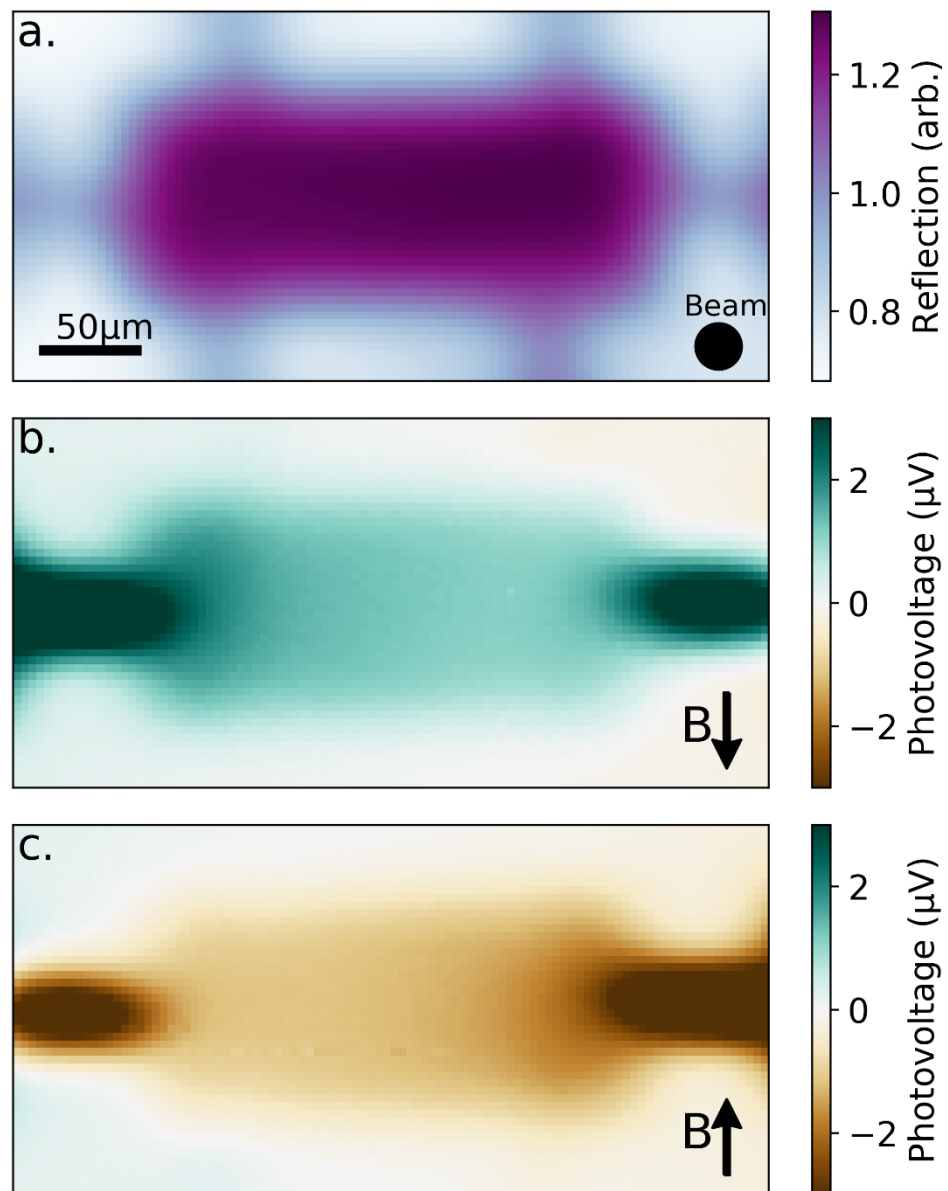


**Figure 5.3:** Measurements of a Pt-YIG Hall bar device. **(a)** Scanning reflection image of device, purple regions are platinum. **(b)** Photovoltage measurement of device with  $B$ -field pointing down. **(c)** Photovoltage measurement of device with  $B$ -field pointing up. Note asymmetry in photovoltage scans near active contacts on left and right sides of Hall bar.

varies by  $\pm 45^\circ$  in the corners of the Hall and by almost  $\pm 90^\circ$  in the perpendicular channels. This quantity can be understood as the angle at which a particular point in space experiences its maximum for the SSE. For the perpendicular channels, this means the maximum signal is achieved when the magnetic field is parallel to the measurement points, in stark contrast with the predictions of basic SSE theory.

#### 5.4 Mapping electrostatic flux lines

We solve for  $\nabla\psi$  in our Hall bar using FiPy<sup>10</sup> and display the results in Fig 5.5a. We next render our experimental SSE phase map as a field of vectors showing the magnetic field resulting in maximum current at every point in Fig 5.5b, then add a second set of vectors pointing *perpendicular* to the magnetic field to show the direction of the generated photocurrent. The plots of current and  $\nabla\psi$  match exactly, showing that our measurement of the SSE provides a precise method for directly imaging the electrostatic lines of flux in any sample geometry.

To confirm the generalizability of our method, we fabricate a terraced Hall cross device and repeat the same SSE measurements. The results are shown in Fig 5.6 and again match theory exactly. In addition to the alignment of  $\nabla\psi$  and  $j_{SSE}$ , we see that the length of the  $\nabla\psi$  vectors accurately predicts the amplitude of photocurrent generated at any point in space. Thus far, these we have assumed the conductivity in our samples is completely uniform, but this is certainly not the case. Future measurements may be able to utilize this method to precisely map out spatial variations in conductivity.

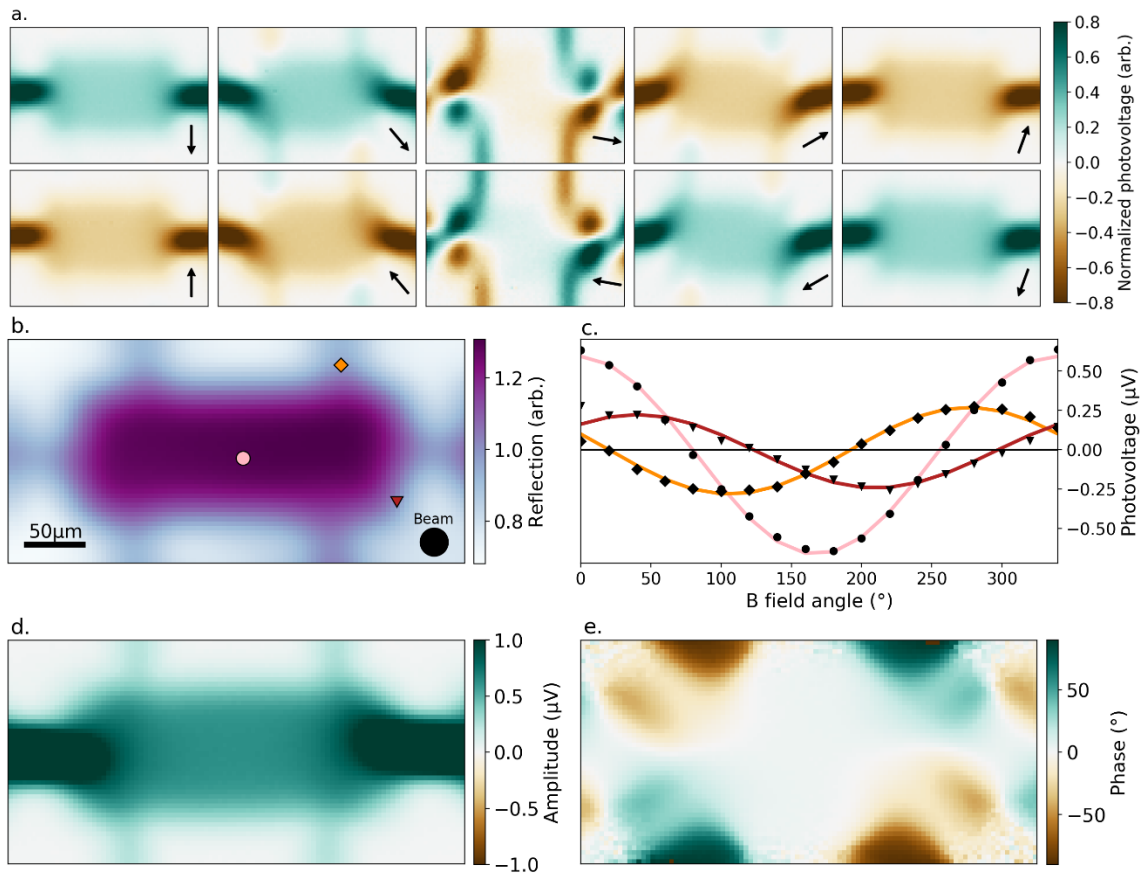


**Figure 5.4:** Spin-Seebeck measurements. **(a)** Spin-Seebeck signal as function of magnetic field direction as shown by arrow. **(b)** Reflection image of Hall bar. **(c)** Photovoltage as a function of field angle at the three points marked in (b). Symbols represent data points while solid lines are sine fits. **(d)** Sine fit amplitude  $A$  mapped in space. **(e)** Sine fit phase map.

## 5.5 Removing the Seebeck effect

The conventional Seebeck effect was discovered by Alessandro Volta in 1794<sup>11</sup> when he heated one end of a metal rod, then placed the ends of the metal rod into two baths of water connected by a bisected frog. The frog legs began to twitch as current moved from the hot bath to the cold. The process driving this macabre experiment stems from the fact that hot electrons have a higher average velocity than cold electrons, causing a net current flow away from a hot region. If this heat flow occurs in a metal junction, a voltage will build up at opposite ends of the junction because the chemical potential in each metal has a different temperature dependence. Measuring the voltage between the ends of the junction in such a setup is proportional to the change in temperature,  $V=S\Delta T$ .

In our experiment, the sample is a platinum bar while the contacts are aluminum so laser-induced heating induces a Seebeck voltage that must be accounted for. To do this, we leveraged the magnetic field-independence of the Seebeck effect. Measuring photovoltage twice, with magnetic field direction switched in between, means that averaging the measurements removes any magnetic field dependent signals. This result is shown in Fig 5.7a, while a simple explanation is shown in panel b. When the beam spot is at the midpoint between two contacts, the temperature difference is zero, resulting in zero voltage between the two. Moving away from the midpoint increases  $T$  and thus voltage difference, all proportional to  $1/r^2$ . Subtracting the Seebeck voltage from the total signal leaves only the magnetic-field dependent spin-Seebeck voltage.

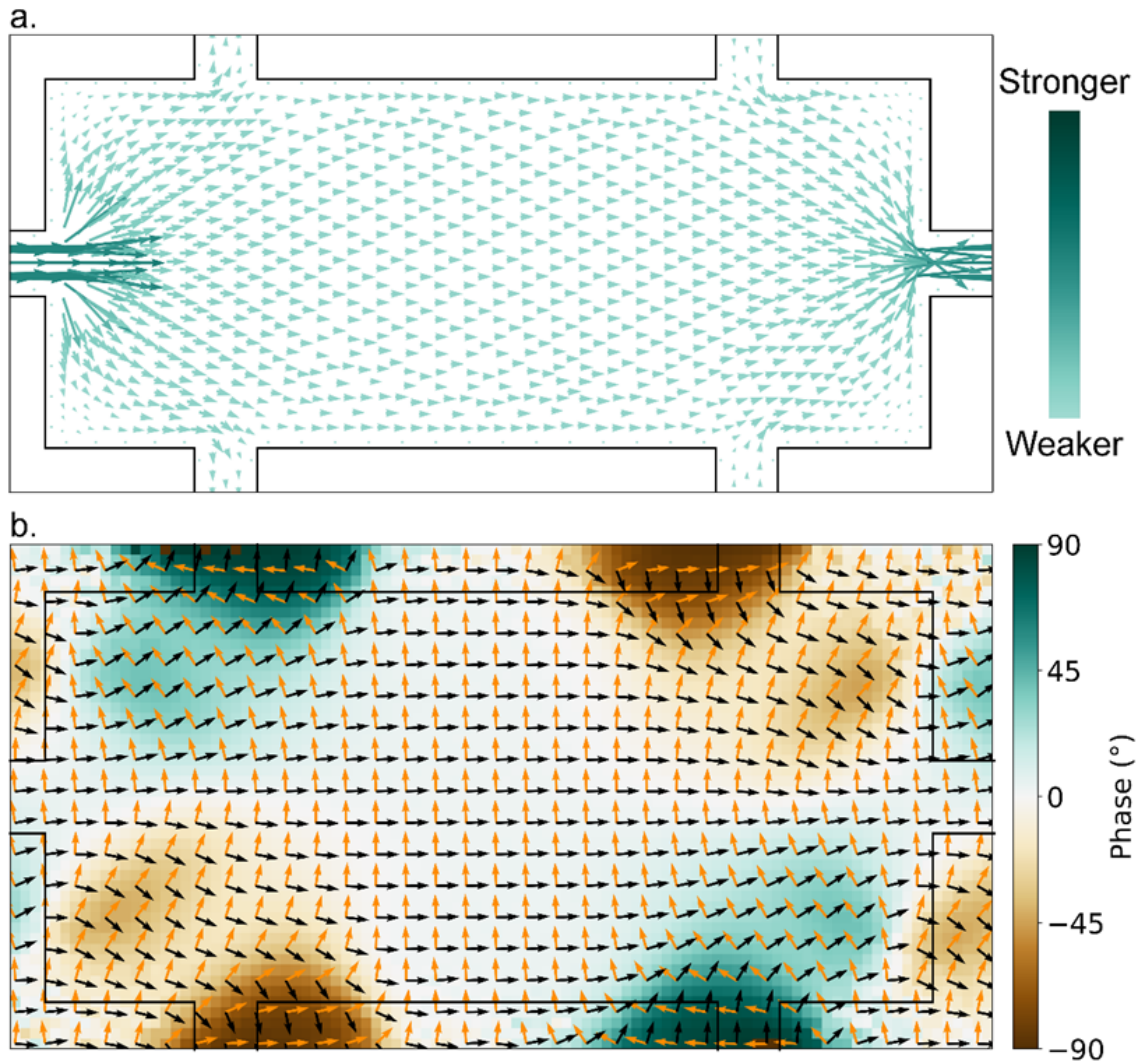


**Figure 5.5:** Shockley-Ramo analysis of a Hall bar. **(a)** Shockley-Ramo field line directions generated using FiPy<sup>10</sup> and prescription of Refs (x,y). Vector length and color correspond to expected amplitude at given location. Hall bar geometry outlined in black. **(b)** Phase map overlaid by magnetic field directions (orange arrows) and resulting local photocurrent (black arrows).

## 5.6 Excluding the Hall effect (and others)

Any measurement driving currents in a magnetic field must of course consider the original Hall effect. Discovered by Edwin Hall in 1879<sup>12</sup>, the effect consists of a deflected current when a wire is placed in a magnetic field. It arises from the Lorentz force on a moving charge,  $\mathbf{F} = q\mathbf{v} \times \mathbf{B}$ . As this effect depends only on the presence of a current and magnetic field (not a magnetization), we repeat our previous measurements on a Pt-GGG device. When probed by a laser, this device will still experience currents associated with the Seebeck effect, but the absence of the magnetic YIG layer means there will be no spin Seebeck effect. The result of this measurement is shown in Fig 5.8 and makes clear that any Hall effect present in the system would make up <1% of the total signal in a spin Seebeck measurement. This measurement also disqualifies the Nernst effect, in which  $\mathbf{V} = \mathbf{B} \times \mathbf{T}$ .

‘Anomalous’ versions of the Hall and Nernst effects depend on magnetization,  $\mathbf{M}$ , instead of  $\mathbf{B}$ , and must also be accounted for. Our measurement apparatus does not provide a convenient way to test for these anomalous effects, but the literature has tried and failed to find significant contributions in Pt-YIG or analogous systems. It has been shown<sup>13</sup> that for a 5nm Pt film in a 0.5T field, the anomalous Hall effect should be of comparable magnitude to the ordinary Hall effect. Since we previously showed the Hall effect is negligible, we can trust that the anomalous Hall effect is also not present. Other groups have been unable to find the anomalous Nernst effect<sup>14</sup> ( $\mathbf{V} = \mathbf{T} \times \mathbf{M}$ ) or the proximity Nernst effect<sup>15</sup>, in which the magnetic layer magnetizes a narrow region of a nearby conductor that then exhibits a Nernst signal.

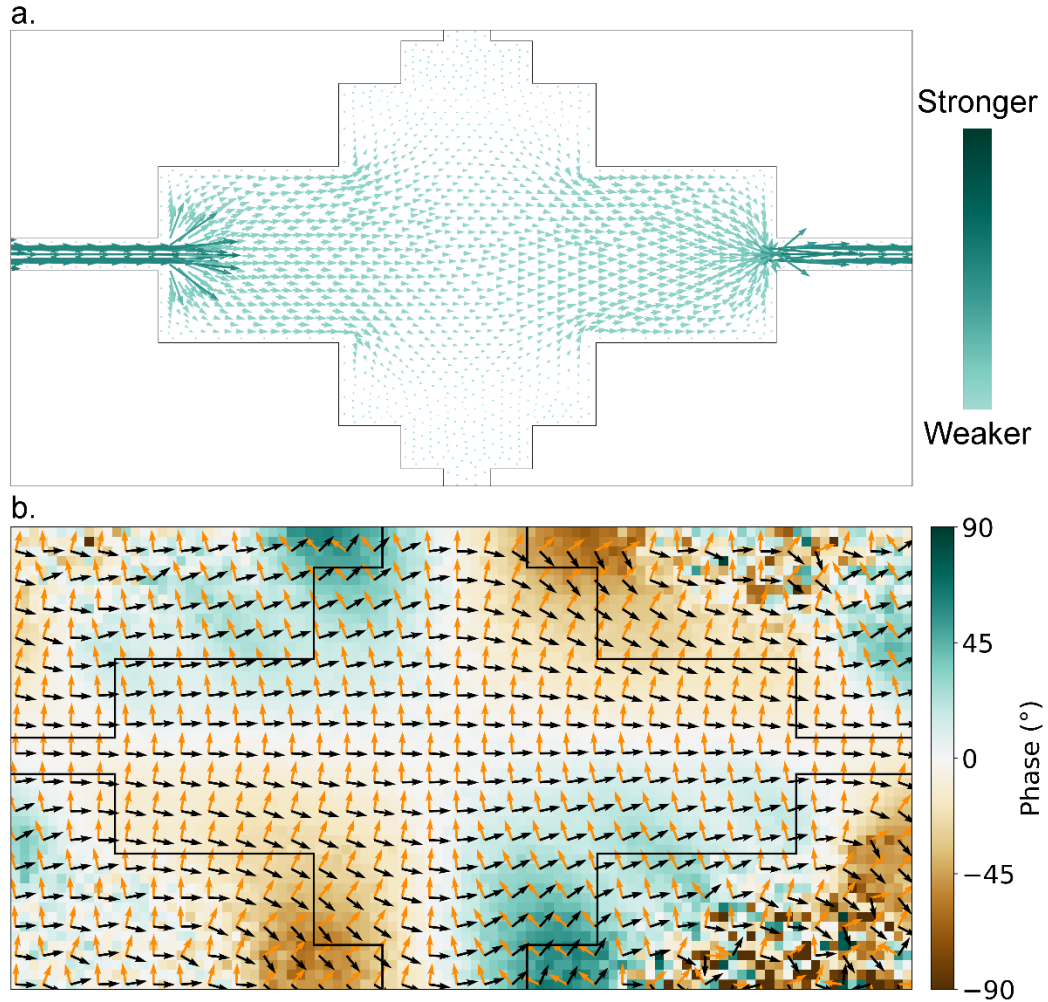


**Figure 5.6:** Shockley-Ramo analysis of terraced Hall cross. **(a)** Shockley-Ramo field line directions generated using FiPy<sup>10</sup> and prescription of Refs (x,y). Vector length and color correspond to expected amplitude at given location. Device geometry outlined in black. **(b)** Phase map overlaid by magnetic field directions (orange arrows) and resulting local photocurrent (black arrows).

## 5.7 Future directions

Earlier, we placed a great deal of emphasis on our measurement's ability to measure at any arbitrary angle, both in- and out-of-plane. No doubt, at this point, hordes of entranced readers are demanding to see what all that was about. Rest assured that these measurements have been taken but relegated to this section as they are intriguing but presently defy explanation. Fig 5.9 shows a plot of the sine fit amplitude in the center of the sample as a function of out-of-plane angle. From our earlier discussion of the theory behind the spin Seebeck effect, we naïvely would expect this dependence to vary as

$V = \mathbf{T} \times \mathbf{M} = TM\sin\theta$ , but this is clearly not the case. This could be due to additional interactions that occur as spins are canted out-of-plane and merits further investigation.

Other avenues to pursue lie in understanding different magnetic systems (such as antiferromagnets) or the interaction between YIG and other materials with high spin-orbit coupling. Tungsten diselenide ( $\text{WSe}_2$ ) and disulfide ( $\text{WS}_2$ ) are two van der Waals materials that exhibit strong spin-orbit coupling. Their very low dimensionality and strong layer dependent properties could also serve as an exciting playground for examining the interplay between heat, electricity, and spin at the nanoscale.

## 5.8 Conclusion

In this chapter, we have shown that multi-dimensional spin Seebeck effect measurements used in conjunction with the Shockley-Ramo theorem can be used to precisely map electrostatic flux lines in arbitrary device geometries. These measurements are free of influence from other magnetic effects and will serve as a steppingstone for

even more data-intensive experiments that will probe subtle thermoelectromagnetic phenomena in a number of different material systems.

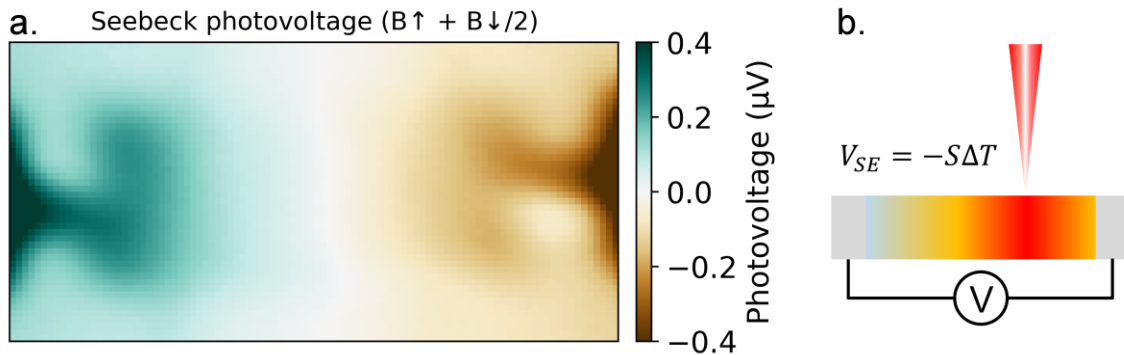


**Figure 5.7:** Seebeck effect analysis **(a)** B-field symmetrized data reveals Seebeck contribution. **(b)** Diagram of the Seebeck effect using a laser as a point heat source.

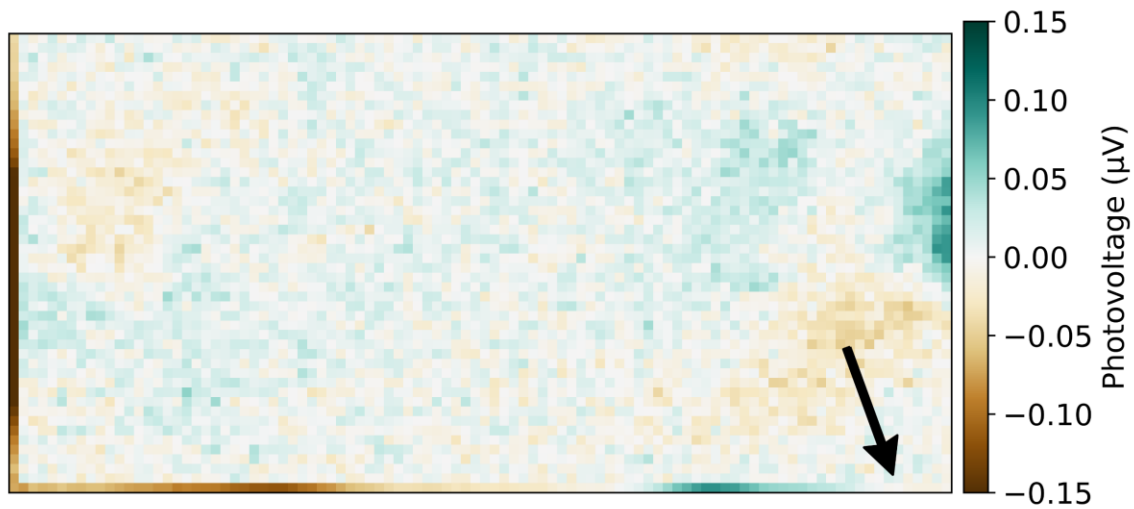


**Figure 5.8:** Lack of spin-Seebeck signal in a Pt-GGG sample.

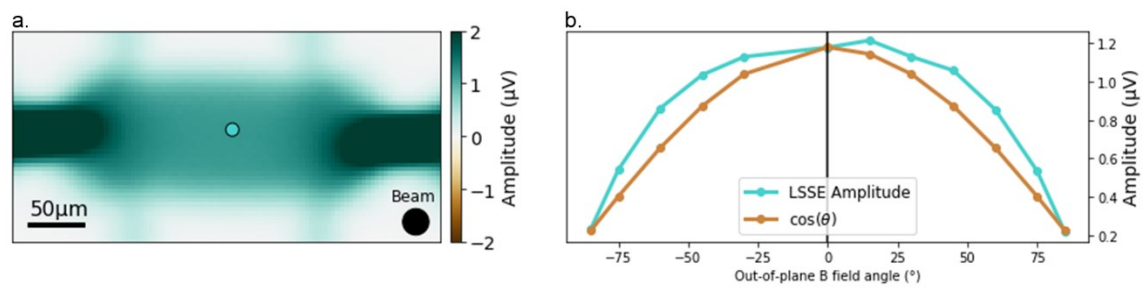


**Figure 5.9:** Spin-Seebeck amplitude in center of Hall bar vs out-of-plane B-field angle.  $\cos(\theta_B)$  included for reference.

## REFERENCES

1. Shockley, W. "Currents to conductors induced by a moving point charge." *J. Appl. Phys.* **9**, 635 (1938).
2. Ramo, S. "Currents induced by electron motion." *Proceedings of the I.R.E.*, June 1941, p. 345.
3. He, Z. "Review of the Shockley-Ramo theorem and its application in semiconductor gamma-ray detectors." *Nucl. Instrum. and Meth. A* **463**, 250-267 (2001).
4. Song, J.C.W., and Levitov, L.S. "Shockley-Ramo theorem and long-range photocurrent response in gapless materials." *Phys. Rev. B* **90**, 075415 (2014).
5. Ma, Q. et al. "Giant intrinsic photoresponse in pristine graphene." *Nat. Nanotech* **14**, 145-150 (2019).
6. Uchida, K. et al. "Observation of the spin Seebeck effect." *Nature* **455**, 778-781 (2008).
7. Weiler, M. et al. "Local charge and spin currents in magnetothermal landscapes." *Phys. Rev. Lett.* **108**, 106602 (2012).
8. Giles, B.L., Yang, Z., Jamison, J.S., and Myers, R.C. "Long-range pure magnon spin diffusion observed in a nonlocal spin-Seebeck geometry." *Phys. Rev. B* **92**, 224415, (2015).
9. Uchida, K. et al. "Local spin-Seebeck effect enabling two-dimensional position sensing." *Jpn. J. Appl. Phys.* **50**, 120211 (2011).
10. Guyer, J.E., Wheeler, D. & Warren J.A., "FiPy: Partial Differential Equations with Python," *Computing in Science & Engineering* **11** (3), 6-15 (2009).
11. Volta, A. "Nuova memoria sull'elettricità animale del Sig. Don Alessandro Volta ... in alcune lettere al Sig. Ab. Anton Maria Vassalli." *Annali di chimica e storia naturale* **5**, 132-144 (1794).
12. Hall, E. H. "On a New Action of the Magnet on Electric Currents." *Amer. J. Math* **2** (3), 287 (1879).
13. Meyer, S. et al. "Anomalous Hall effect in YIG|Pt bilayers." *Appl. Phys. Lett.* **106**, 132402 (2015).

14. Miao, B.F., Huang, S.Y., Qu, D., and Chien, C.L. “Absence of anomalous Nernst effect in spin Seebeck effect of Pt/YIG.” *AIP Advances* **6**, 015018 (2016).
15. Kikkawa, T. et al. “Longitudinal spin Seebeck effect free from the proximity Nernst effect.” *Phys. Rev. Lett.* **110**, 067207 (2013).

## **Chapter 6**

### **Conclusion**

#### 6.1 Complexity begets complexity

As materials and devices continue to shrink towards the ultimate atomic limit, the sensitivity of such systems will surge, necessitating an increase in experimental and analytical complexity. The first chapter of this dissertation traced the history of optoelectronic measurements from the time of Hooke to the present day, emphasizing the new areas of understanding illuminated by new technological developments. The second chapter discussed our implementation of a modern, highly modular optoelectronic microscope capable of being rapidly reconfigured to measure a multitude of different sample properties. This microscope was first used to confirm the effectiveness of a new method for developing candidate lasing materials by spatially mapping photoluminescence spectra as a function excitation wavelength (Chapter 3). We then used our microscope to generate and characterize carrier multiplication in an atomically thin transition metal dichalcogenide heterostructure (Chapter 4). Finally, we developed a data-dense methodology to directly map electric field lines in arbitrary devices using the spin-Seebeck effect in a normal metal-magnetic insulator device. These measurements, discussed in Chapter 5, also revealed an unexpected out-of-plane behavior that would have remained invisible with a less comprehensive measurement. Our experiments serve to highlight the versatility of our instrument and provide blueprints for future projects as the world of nanoscience becomes ever tinier and more intricate.

## Appendix A

### Visualizing Nanoscience

#### A.1 Introduction

This appendix serves to describe our efforts in publicizing the work done by our lab. We focus specifically on reasons to make research more accessible to the public, provide a framework for understanding how to translate results in an impactful manner, and finally demonstrate that creating high-quality media for public consumption using free software is easier than one might think.

#### A.1 Popularizing science:

In 1959, Rod Serling was interviewed on 60 Minutes about the limits of television, his chosen medium, to produce programs with a wider social impact. His answer to a question about sacrifices he would have to make to maintain his integrity is an important one for scientists to consider even today<sup>1</sup>:

**Interviewer:** [Herb Brodkin] said, "Rod is either going to stay commercial or become a discerning artist, but not both." Now, has it ever occurred to you that you're selling yourself short by taking on a series which, by your own admission, is going to be a series primarily designed to entertain?

**Rod Serling:** I remember the quote... I didn't understand it at the time. I failed to achieve any degree of understanding in the ensuing years which are three in number. I presume Herb means that inherently you cannot be commercial and artistic. You cannot be commercial and quality. You cannot be commercial

concurrent with and have a preoccupation with the level of storytelling that you want to achieve. And this I have to reject. I think you can be, I don't think calling something commercial tags it with a kind of an odious suggestion that it stinks, that it's something raunchy to be ashamed of. I don't think if you say commercial means to be publicly acceptable, what's wrong with that? The essence of my argument, Mike, is that as long as you are not ashamed of anything you write if you're a writer, as long as you're not ashamed of anything you perform if you're an actor, and I'm not ashamed of doing a television series... But I think innate in what Herb says is the suggestion made by many people that you can't have public acceptance and still be artistic. And, as I said, I have to reject that.

Though Serling was talking about the entertainment industry, the sentiment perfectly applies to the choices made by scientists. Every scientist, at some point in their career, must ask the questions “Who should know about my work? How should I package it for maximum effectiveness? How much effort should I expend towards advocating my work?” Ultimately, many choose to eschew packaging their work for the wider public because of the effort required, the perceived lack of reward, and because of reasons like those disputed by Serling above: that making something publicly acceptable can feel like ‘dumbing down’ research to an unacceptable level. Like Serling, I have to reject these notions. No one will ever understand an experiment better than the people who carried it out, and especially not a harried science writer looking for an interesting publication to spin into an 800-word article. By creating the materials for a project’s publicity

themselves a scientist can also take control of the narrative that might arise around their work, reducing the risk of a possible misinterpretation by a source outside of the lab.

### A.3 Translating science for the public

Very few people will possess the knowledge to completely understand every nuance of any single scientific article. However, this does not mean they cannot get anything useful out of a scientific research project. Rather, this means that it is the job of the scientist to identify the most important conclusion of their work and focus on explaining that as clearly and concisely as possible, while emphasizing possible connections to real-world examples that the public can use to mentally anchor the research.

The art of title design is an unexpected but valuable resource in approaching how to condense complex scientific results into small packages that non-specialists can digest. By title design, we mean the creation of opening and closing titles for film and television. Title designer face the difficult task of condensing all the complexities and atmosphere of an hours-long production down into a short sequence that can last anywhere from five minutes to fifteen seconds. This is also frequently done without any sort of additional narration or expository text – the visuals alone set the mood and engage the interest of the viewer.

As an example, we focus on the [title design of the 2014 television series \*Halt and Catch Fire\*](#)<sup>2</sup>, which is about a company struggling to break through during the personal computer revolution of the 1980s. The title sequence uses the imagery of electrons traveling through a computer chip as an analogy for the intense pressure faced by the

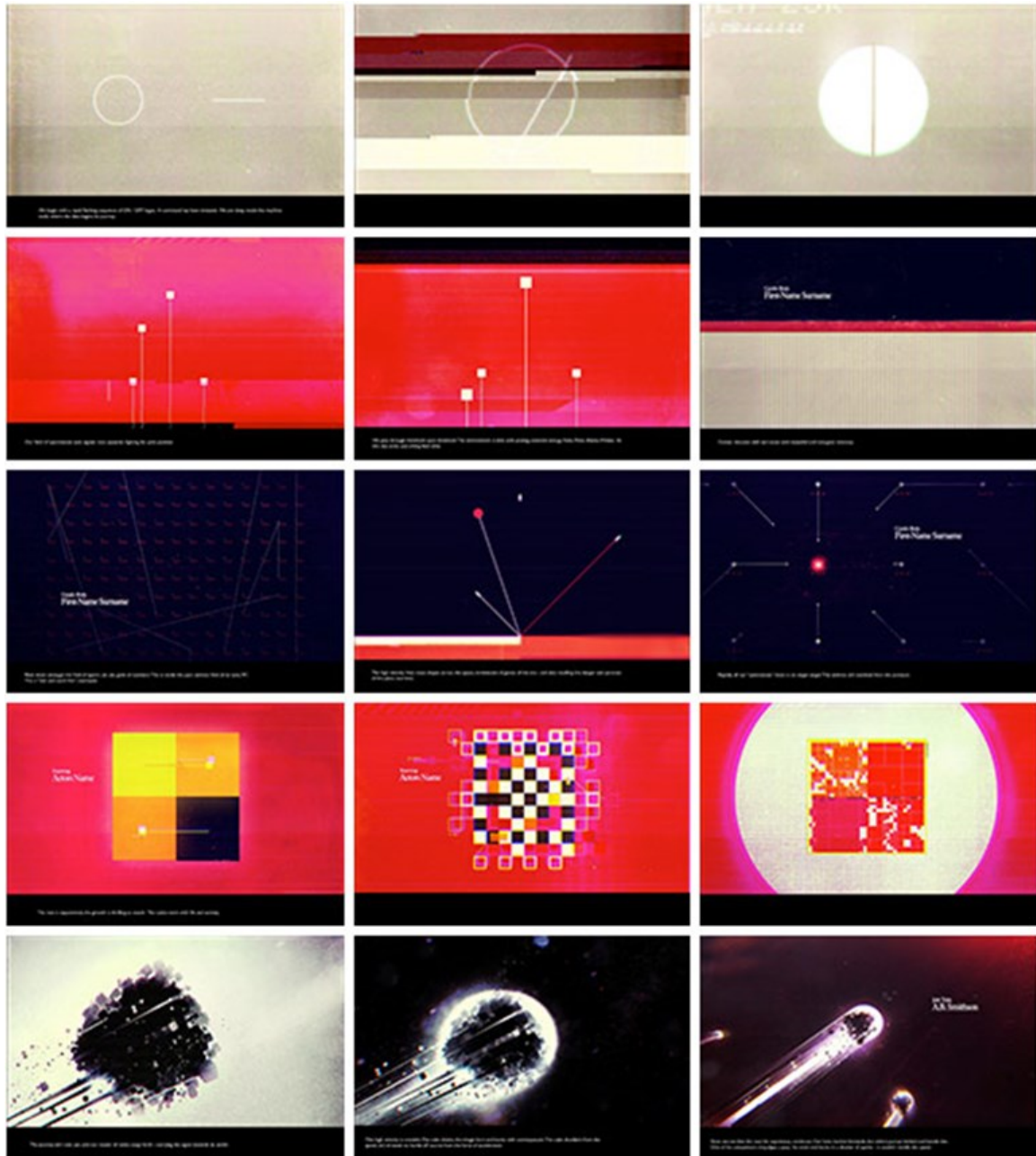


**Figure A.1:** Concept stills from the title sequence of *Halt and Catch Fire*<sup>2</sup>.

people working to make those chips a reality. Representative frames are shown in figure A.1.

There are three core concepts to focus on in this title sequence that are relevant to the interested scientist: speed, growth, and energy. The title sequence uses several artistic techniques to emphasize these properties, even in still frames.

Speed is illustrated in Fig A.2. The image on the left is from concept art that did not make it into the final title, while the right made is taken directly from the title itself. Though both images clearly reflect the same basic idea, the image on the right *feels* faster because, as any physicist knows, speed is only defined between *two* objects. By contrasting the electron and its trail with the burst in the wall, we can tell that the electron not only came through the wall but also outpaced the shockwave from doing so, so it must be moving quickly.

Growth is shown in Fig A.3. Here, a black square (representing an idea), rapidly gestates and develops into something much more complex. This is a difficult idea to show in still frames, but an important thing to notice is that as the square ‘develops’, it gains more complexity in 2D, and finally, in Fig A.3. (d), develops significant non-uniformity and depth, showing that it has broken free of two dimensions and is now growing in the 3<sup>rd</sup> dimension as well.

Finally, energy is highlighted in Fig A.4. For macroscopic objects, high energy processes result in shaking, blurring, distortion, and fragmentation – think gunshots or rocket launches. Using these techniques to illustrate nanoscience is a fantastic way to make visuals more interesting as well as approachable for a lay audience. Why say

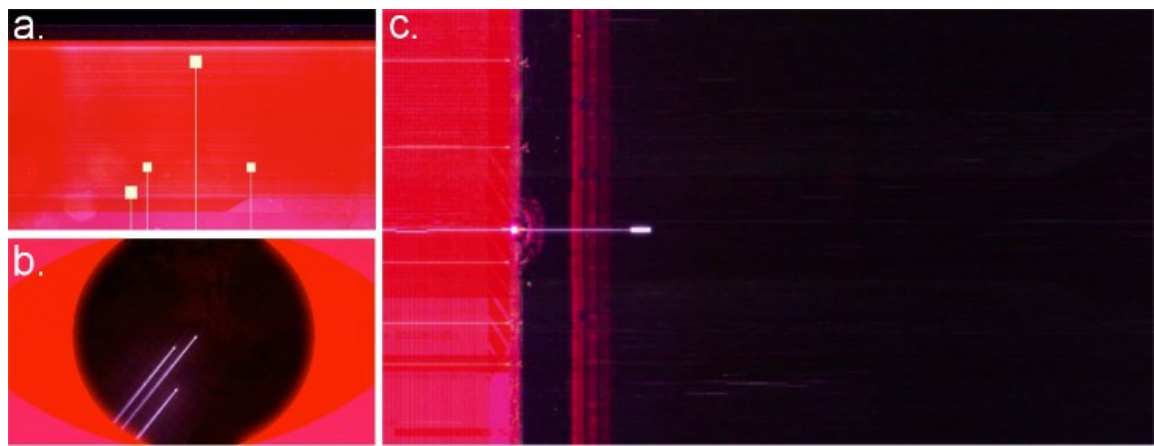


**Figure A.2:** (a,b) Stills<sup>2</sup> that imply motion but not speed. (c) A still that implies speed.

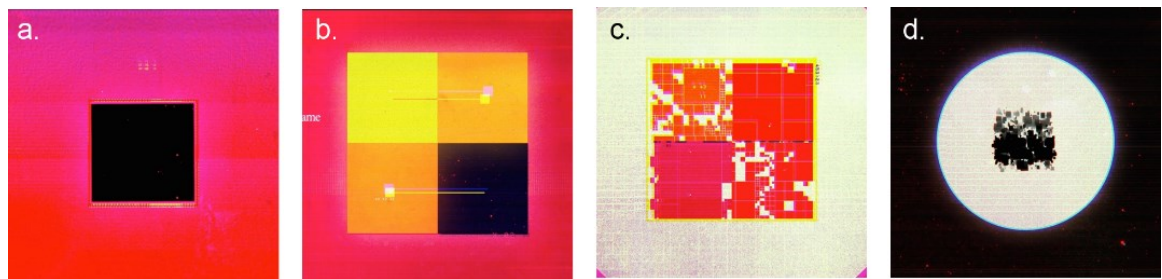


**Figure A.3:** Stills<sup>2</sup> showing a growth process.

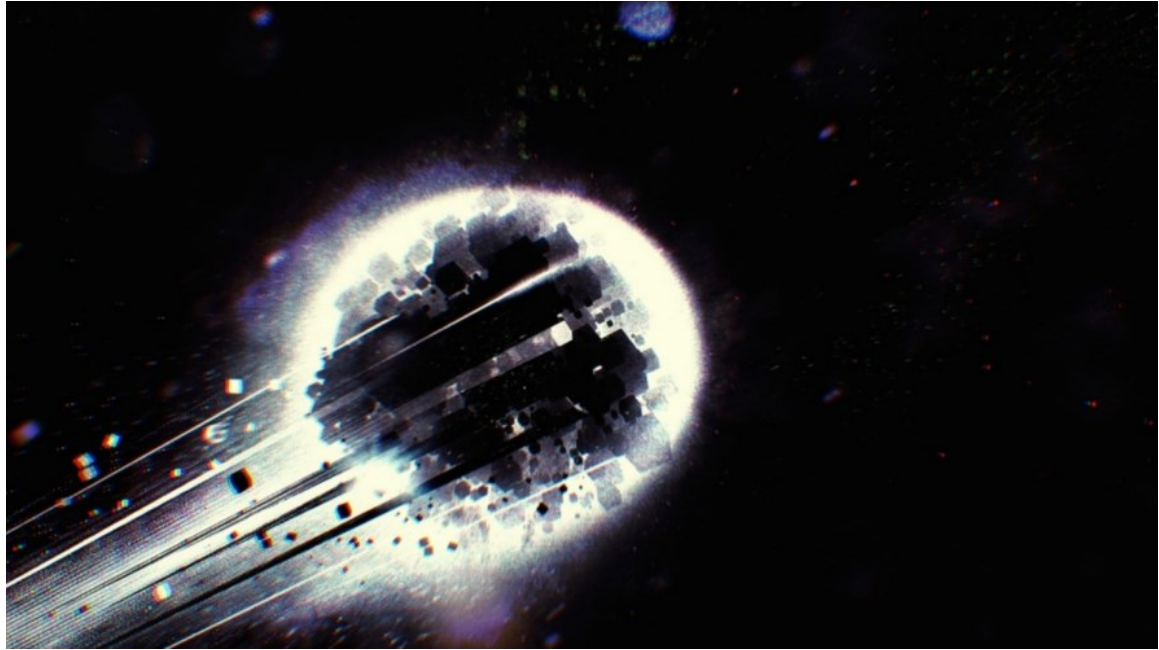


**Figure A.4:** Still<sup>2</sup> showing a high-energy particle distorting and breaking.

something is ‘high-energy’, leaving them to question what that means in a given context, when you can just encode that information in your visual at an instinctual level?

#### A.4 Creating high-quality visuals using free, open-source software

Another major reason scientists avoid outreach is that it seems hard. Most scientists are not artists, so it can seem like too much to ask that one spend a large amount of time learning how to artistically represent their work. This is not the case! At this point, 2D drawing and 3D modeling/animation software have become incredibly powerful, and there are versatile Free and Open-Source Softwares (FOSS) available. In this work, we have used the Gnu Image Manipulation Program (GIMP) for 2D artwork and the free educational version of 3ds Max for 3D, but we highly recommend any interested party to instead use Blender for 3D animation as it has much of the same functionality as 3ds Max, is FOSS, and has a significantly better tutorial community.

The strength of the tutorials is such that I was able to make my first high-quality, 30-second animation after about three weeks of effort learning the software and then applying it to the project we were working on at the time (the carrier multiplication project discussed in Chapter 4). Figure A.5 shows the progression from initial drafts to final version over the course of three weeks. These are both still frames from animations, the final version is viewable [here](#). When we published this work, the university news department was ecstatic that we already had visuals that we had developed – ultimately, it saved time as there was no back-and-forth between our lab and the university graphics team about how to portray our research.<sup>3</sup>

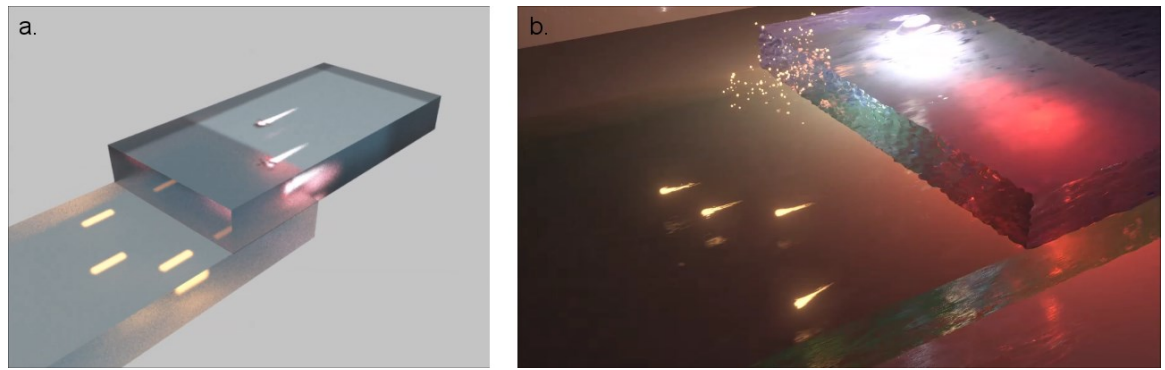


**Figure A.5:** (a) Early draft of carrier multiplication animation. (b) The same scene improved after tutorials.

We show how to build such a scene step-by-step in Figure A.6. We begin by setting the stage with simple geometry and lighting. Most 3D animation software comes with a built-in material library and physical lighting, so it is easy to make a block and set it to interact with light like a piece of metal, tile, glass, or anything else. Next, we add our focus pieces, in this case, the moving ‘particles’ we used to represent electrons, elongated to highlight their motion. Particle ‘explosions’ are an optional touch to highlight the energy transfer of the process we were talking about – in the animation, we also add a bit of camera-shake to enhance the impact of the impact and make the video feel more professional. Once this is taken care of, we introduce distortions to break up the unnatural-feeling straight lines in our geometry. A bumpy layer feels more real, especially if it is supposed to represent something microscopic. The beauty of the software we use is that there is no hand-sculpting of the ridges in the image; everything is accomplished through adjusting noise and bump modifiers. The final touch is to add some lighting effects to increase the feelings of heat and energy for the viewer.

More complicated imagery can be represented by using scripting. Collective phenomena are common in condensed matter physics and provide an excellent opportunity for outreach. We tackled representing a skyrmion for DOE-sponsored newsletter<sup>4</sup> using scripts to animate rotation and color based off position, the result is shown in Fig A.7.

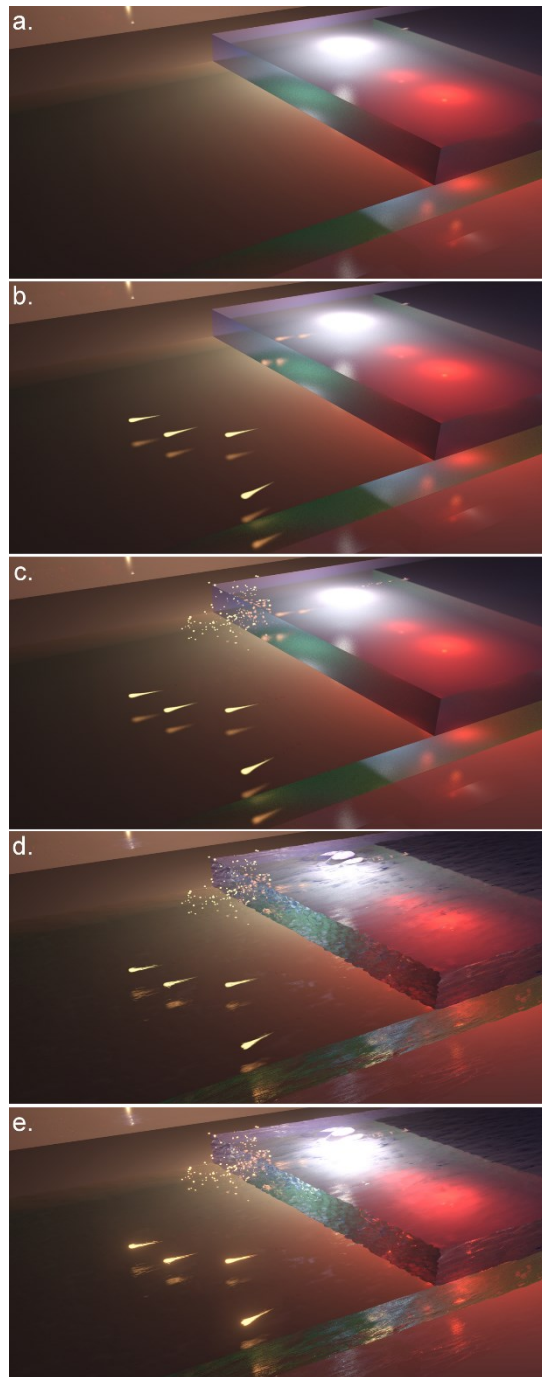


**Figure A.6:** Stills showing development of image from basic components to final version.

Finally, for more complicated phenomena, hand-animation and scripting may be inadequate. Modern software also includes particle systems that can be influenced by tunable forces such as gravity, collision, wind, shear, and others. We used particle systems to animate a result seen in our lab, the formation of an electron-hole liquid, with the result shown in Fig A.8. This animation proved to be our most successful so far: within two weeks of publication, the video (viewable [here](#)) had received over 5000 views, with most views coming from non-academic sources.<sup>5</sup> For a science video about high-level, cutting-edge research, this is a tremendous amount of exposure to an audience that would otherwise have never known what was going on in our lab. This result especially demonstrates that with a moderate effort, it is possible to communicate the main points of academic-level research to a wider audience and maintain integrity along the way.

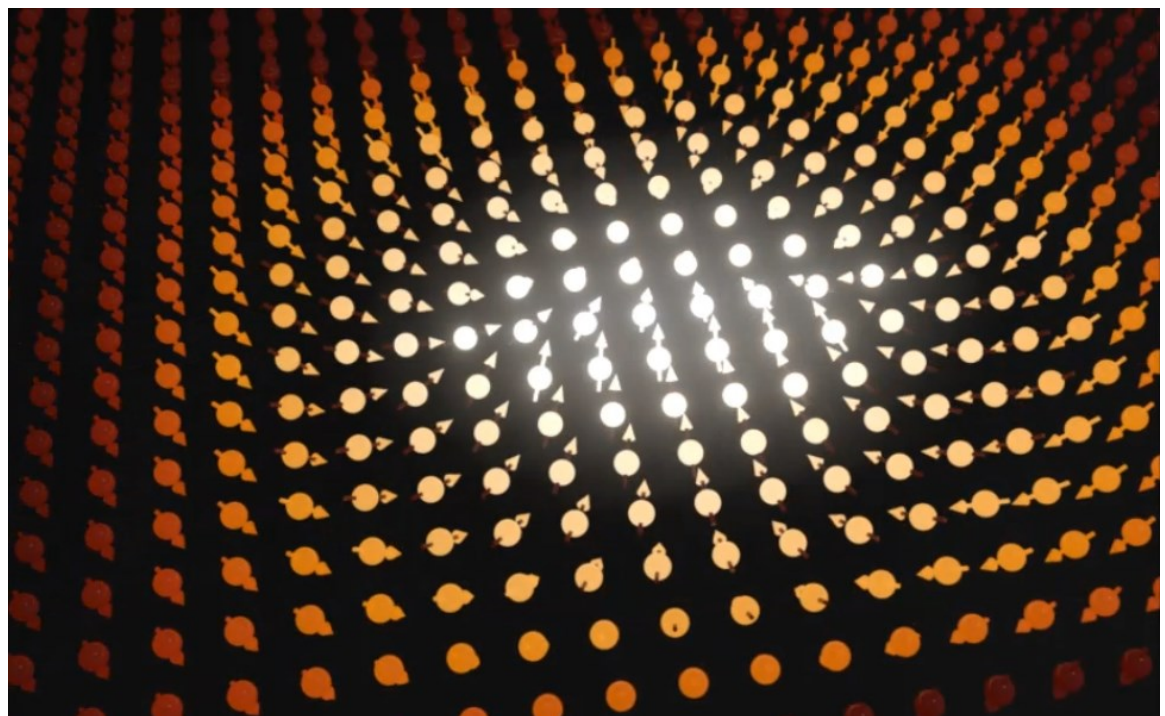


**Figure A.7:** A skyrmion animation.

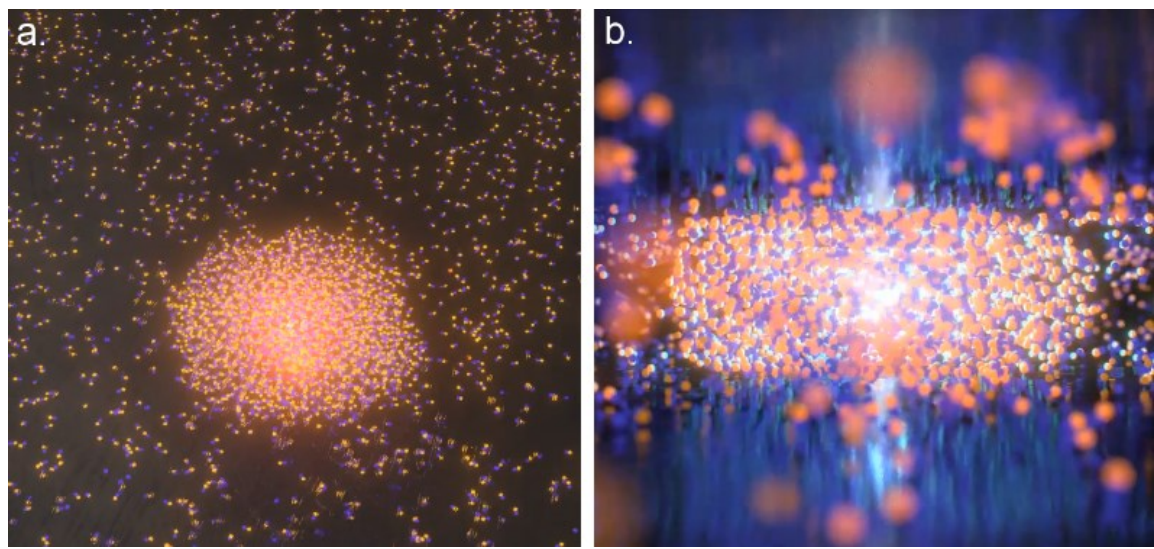


**Figure A.8:** **(a)** Birds-eye explanatory view of electron-hole liquid. **(b)** Artistic rendering of interior of electron-hole liquid.

## REFERENCES

1. Serling, Rod. Interview by Mike Wallace. *The Mike Wallace Interview*, 1959.
2. Clair, Patrick and Marks, Raoul. Interview by Art of the Title. *Art of the Title*, 2014. <https://www.artofthetitle.com/title/halt-and-catch-fire/>
3. Pittalwala, I. “Prototype shows how tiny photodetectors can double their efficiency.” *UCR Today*, 9 Oct 2017, <https://ucrtoday.ucr.edu/49282>.
4. Grossnickle, M. “Harnessing quantum vortices.” *Frontiers in Energy Research*, Summer 2017, <https://www.energyfrontier.us/content/harnessing-quantum-vortices>.
5. Meredith, D. “UC Riverside physicists create exotic electron liquid.” *UC Riverside News*, 4 Feb 2019, <https://news.ucr.edu/articles/2019/02/04/uc-riverside-physicists-create-exotic-electron-liquid>.